ASPECTS OF THE PROPAGATION OF AN INTERNAL SOLITARY WAVE OF DEPRESSION OVER FLAT AND GENTLY VARYING BATHYMETRY

A Dissertation

Presented to the Faculty of the Graduate School

of Cornell University

in Partial Fulfillment of the Requirements for the Degree of

Doctor of Philosophy

by

Gustavo Rivera-Rosario

December 2018

ASPECTS OF THE PROPAGATION OF AN INTERNAL SOLITARY WAVE OF DEPRESSION OVER FLAT AND GENTLY VARYING BATHYMETRY

Gustavo Rivera-Rosario, Ph.D.

Cornell University 2018

The propagation of an Internal Solitary Wave (ISW) of depression is explored through highly-accurate numerical simulations, over a flat surface and gently varying bathymetry. The interaction between the ISW and the bottom bed may produce sediment resuspension capable of influencing bed morphology, facilitate nutrient access for organisms living in the water column, and possibly impact the integrity of bottom-lodged structures. As the wave shoals over gently varying bathymetry, an instability may develop, inducing convective breaking and causing the formation of a trapped, or recirculating core. The turbulent flow inside the core dissipates kinetic energy, mixes the fluid, and transports suspended material material, in the water column, across large distances.

To understand the impact of the propagating ISW over the bottom bed, the pore-pressure field is examined using high-accuracy numerical simulations. The velocity and density fields are obtained by solving the Dubreil-Jacotin-Long (DJL) Equation, for a two-layer, continuously stratified water column. The total wave-induced pressure across the surface of the bed is computed by vertically integrating for the hydrostatic and nonhydrostatic contributions. The bed is assumed to be a continuum composed of either sand or silt, with a small amount of trapped gas. Results indicate variations in pore-water pressure penetrating deeper into more conductive materials and remaining for a prolonged period after the wave has passed. In order to quantify the potential for failure, the

vertical pore-pressure gradient is compared against the buoyant weight of the bed. The pressure gradient exceeds this weight for weakly conductive materials. Failure is further enhanced by a decrease in bed saturation, consistent with studies in surface-wave induced failure. In deeper water, the ISW-induced pressure is stronger, causing failure only for weakly conductive materials. The pressure associated with the free-surface displacement that accompanies ISWs is significant, when the water depth is less than 100m, but has little influence when it is greater than 100m, where the hydrostatic pressure due to the pycnocline displacement is much larger. Since the pore-pressure gradient reduces the specific weight of the bed, results show that particles are easier for the flow to suspend, suggesting that pressure contributes to the powerful resuspension events observed in the field.

When an ISW propagates over gently varying bathymetry, a trapped, or recirculating, subsurface core may develop as a consequence of a preceding convective instability. Its formation is explored through fully nonlinear and non-hydrostatic two-dimensional simulations. The computational approach is based on a high resolution/accuracy deformed spectral multidomain penalty method (SMPM) flow solver, which incorporates observed background current and stratification profile [103], along with recorded bathymetry, from the South China Sea. Given these field conditions, the SMPM flow solver is initialized using the solution of the fully-nonlinear Dubreil-Jacotin-Long (DJL) Equation. During shoaling, convective breaking precedes core formation, as the ISW-rear steepens and the trough decelerates; heavier fluid plunges forward and becomes trapped. This breaking mechanism is attributed to the stretching of the near-surface vorticity layer of the baroclinic background current. Since the sign of the vorticity is opposite to that of the propagating wave, only subsurface

recirculating cores can be obtained. Once the core is established, the ISW propagates preserving its symmetric waveform. The onset of convective breaking is visualized, along with quantifying the sensitivity of the core properties to changes in the initial wave, near-surface background velocity, and maximum slope of the measured bathymetry. Various methods of defining the subsurface core boundary are explored and compared with field observations. The simulations capture the development of the recirculating subsurface core, but not the observed wave properties.

The Richardson number and lateral vorticity are used to investigate the presence of shear instabilities of Kelvin-Helmholtz (KH) type, possibly preceding the convective instability. Results in indicate that these may occur as a consequence of the convective instability, but not as an individual event. A three-dimensional simulation is initialized prior to convective breaking and the ISW is then allowed to propagate until convective breaking occurs. As the wave shoals, three-dimensional breaking ensues, but no turbulent flow is simulated. Lateral convective instabilities develop due to the primary convective overturn. The evolution of the Kinetic Energy (KE) and Available Potential Energy (APE) suggests that KE is extracted from the background current and converted to APE through the buoyancy flux. Overall, the results constitute a baseline for future three-dimensional simulations aimed at exploring the turbulent flow inside the core.

BIOGRAPHICAL SKETCH

The author was born in San Juan, Puerto Rico. He graduated from Rensselaer Polytechnic Institute, with a Bachelor of Science in Aeronautical Engineering and a Master of Science in Mechanical Engineering. After working for two years in the field, he moved to Ithaca, NY, to pursue doctoral studies at Cornell University, in the School of Civil and Environmental Engineering, under the guidance of Peter J. Diamessis.

To my beloved family.

ACKNOWLEDGEMENTS

This dissertation could not have been possible without the mentorship and rapport of my graduate advisor, and committee chair, Prof. Peter Diamessis. Thank you for your patience and dedication towards my development, since my first day at Cornell; a truly one-of-a-kind advisor. I am forever grateful for helping me grow as a professional and as a human being. I will miss very much our one-on-one discussion on work and life.

I would also like to thank my other committee member, Prof. James Jenkins, who became interested in my graduate formation during my early years as a PhD student. I was fortunate enough to take a course with you, before retirement, and attend a conference in Germany; I met some truly amazing researchers there. I would like to acknowledge my other committee member, Prof. Olivier Desjardins, who also taught me computational methods. Over the last three years we had very productive exchanges of ideas on how to model my wave propagation problem. I will miss your passionate lectures on numerical methods and your thoughtful and constructive insight on my work.

I would also like to acknowledge the various visiting researchers and professors, that provided valuable feedback on my work, particularly Ren-Chieh Lien, Kevin Lamb, and Marek Stastna; thank you all for your time and dedication. Thank you also to Greg Thomsen, for dedicating endless hours to the development of the numerical tools used by our research group and for teaching me about HPC and helping develop my programming skills.

My life as an EFMH'er was complemented by my dearest colleagues; thank you Allie, Amir, Anil, Blair, Brianna, Che-Wei, Chao, Dan, Diego, Erika, Ignacio, Jiajun, Joe, John, Jose, Katie, Kris, Mahmoud, Nimish, Pato, Peter, Qi, Seth, Sumedh, Veronica, Theo, and Xiao. I enjoyed learning from all of you during

these past few years and I hope we remain in touch. I would also like to acknowledge the support of Prof. Todd Cowen, who allowed me to TA CEE3310 for two semesters; thank you for letting me be part of your team. I would also like to acknowledge Prof. Philip L.-F. Liu and Prof. John Albertson; thank you for teaching me about waves, porous media flows, and atmospheric boundary layers. Finally, I want to thank the amazing CEE staff: Nadine, Tania, Charissa, Jeanette, Meghan, Tim, Paul, Jeff, Joe, Cameron, and Carl.

I want to also acknowledge the various funding agencies and entities that have sponsored me, particularly the Alfred P. Sloan Foundation, Diversity Programs in Engineering, the Joseph DeFrees Fellowship, the National Science Foundation, and the Office of Inclusion and Student Engagement. Thank you Jami Joyner and Sara Xayarath Hernandez for supporting me from day-one. Your dedication and hard-work makes a true difference in the lives of Cornell students and I was fortunate to have met you.

Lastly, I want to thank my former advisor, Prof. Luciano Castillo, my friends, family, and my beloved Christina. I could not have started and finished this chapter in my life without your love and support; it's the culmination of almost six years of sacrifices and arduous work and you all were there, behind the scenes, pushing me forward. Thank you for believing in me. I love you all.

TABLE OF CONTENTS

LIST OF TABLES

LIST OF FIGURES

CHAPTER 1

NONLINEAR INTERNAL WAVES IN THE OCEAN

1.1 What are Nonlinear Internal Waves?

Nonlinear Internal Waves (NLIWs) are ubiquitous in stratified environments, in the oceans, lakes, and atmosphere. In this study, they are regarded as large amplitude, long-wavelength, vertical displacements of an interface that separates two regions with a relatively constant density value, within a water column. This interface is known as the pycnocline and corresponds to a sharp transition from one fluid density to the next. The density can be related to the temperature and salinity via the Equation of State [175]; if the stratification is based on temperature, then the transition region is known as the thermocline, and halocline, if the stratification is based on salinity.

The waves have a polarity that corresponds to the direction of the pycnocline displacement [60]; NLIWs can be either elevation-type or depression-type. The direction is determined by the location of the interface, with respect to the half-depth of the water column. If the pycnocline is located above mid-depth, then waves of depression form; the opposite occurs for a pycnocline below mid-depth. An upward displacement is known as a *crest*, while a *trough* refers to a downward displacement.

Once the pycnocline has been displaced, nonlinear steepening, balanced by the nonhydrostatic dispersion, produce large amplitude oscillations, of long wavelength, that are capable of traveling without change in form for hundreds of kilometers. These interface oscillations propagate as packets, ordered

from the largest to the smallest amplitude. Without dispersion, the waves will steepen and break, whereas without nonlinearity waves will scatter onto higher wavenumbers, or disperse. In the ocean, the mechanisms that can generate such large displacements are regarded as [78]: formation of lee waves across a ridge or sill during ebb and flood tides [66, 113], internal bores from to the receding internal tides off the continental shelf [74, 167], the breaking of the internal tide associated with nonlinear processes and rotation [70], localized internal tidal energy beams [132], resonant forcing from the bathymetry [35], and gravity currents exerted by river plumes, as shown in Figure 1.1 [129, 86].

When the interface is displaced in a single direction (i.e. upward or downward), a mode-1, hump-like, wave forms. If the displacement is in both directions, simultaneously, then a mode-2 wave exists, that may be either concave [166, 173, 155, 23, 27, 38] or convex [116], where concave denotes isopycnals displaced away from the pycnocline (i.e. bulge-like or varicose [160]) and convex refers to isopycnal displacements into the pycnocline (i.e. pinch-like form). Other higher energetic mode may exist, but the vast majority of the NLIW energy is contained within a mode-1, and to a lesser extent, mode-2 waves.

A single, large amplitude nonlinear internal wave may be represented as a solitary wave [149], internally, also known as an Internal Solitary Wave (ISW) [85, 37, 136]. Waves are, by definition, a propagation of energy, although changes in waveform may result in the transport of mass and momentum as well. Locations at which ISWs have been observed include the Andaman Sea [136], Massachusetts Bay [66, 25, 174], Monterey Bay Shelf [31, 186], the New Jersey Shelf [126, 161], the Northern Oregon Coast [167], the northwest Portuguese Shelf [142], the Sulu Sea [11], and the South China Sea (SCS)

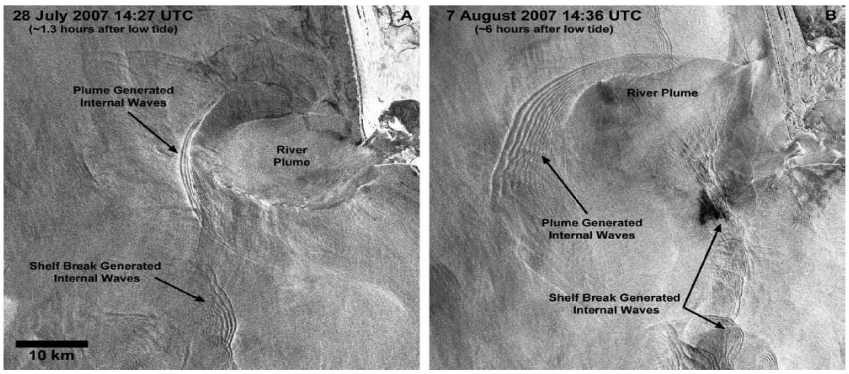

Figure 1.1: Packets of Nonlinear Internal Waves generated from the interaction between a River Plume and the Pacific Ocean, near the river mouth of the Columbia River, in Oregon, USA. The images were obtained via SAR [78].

[77, 51, 192, 143, 104], among many others.

Internal Solitary Waves have also been observed in the atmosphere. They can be visualized as distinct roll clouds, like the Morning Glory near the Gulf of Carpenteria in Northern Australia, and may cover either a few kilometers above the surface of the earth or the entire troposphere. Generation mechanisms include gravity currents associated with katabatic (downslope) winds, blowing over mountain ranges, and large-scale penetrative convection trapped in the troposphere [147]. Note that the upper part of the troposphere may be defined as a neutrally stratified or a strongly stratified upper layer that inhibits internal reflections.

1.2 Properties of Internal Solitary Waves in the Ocean

Internal Solitary Waves are characterized by their large length scales. Their maximum isopycnal displacement is known as the *amplitude*, regardless of displacement direction; that is, how much has the pycnocline been displaced from its reference water depth. In addition, their *half-width* is defined as the integral of the maximum isopycnal displacement along the direction of propagation [90], divided by the amplitude; twice the half-width is equivalent to the ISW wavelength.

The waves posses a velocity scale associated with the speed of the maximum isopycnal displacement; it is defined as the wave *propagation speed* and may be used to describe how fast the wave is moving across the water column. ISWs are also known for their distinct horizontal-induced and vertical-induced velocity field. Mode-1 ISWs induce only horizontal motion above and below the crest or trough, and only vertical motion ahead and behind. The direction of the velocity is dictated by the direction of propagation. For an ISW of depression, positive and negative horizontal velocity is induced above and below the trough, respectively; negative and positive vertical velocity is induced ahead and behind the wave, respectively. An ISW of elevation induces negative and positive horizontal velocity above and below the crest, respectively, and positive and negative vertical velocity ahead and behind the wave, respectively.

In addition to their velocity and length scales, ISWs are characterized by their free-surface signature [139, 125, 32], also shown in Figure 1.1. A depression-type mode-1 ISW, induces only horizontal velocity above the trough, as previously noted. This velocity region extends up to the free-surface; here,

the horizontal motion pushes the fluid forward, creating a modulation of the air-water interface. This displacement is a fraction of the ISW wavelength, nevertheless large enough that can be detected via Synthetic Aperture Radar (SAR) [11].

Lastly, Internal Solitary Waves also induce pressure in the water column. Their pressure is a combination of a non-hydrostatic component, associated with the wave-induced velocity, and a hydrostatic component, associated with the free-surface and isopycnal displacement [127]. The hydrostatic pressure, due to the wave-driven perturbation, is defined as that exerted by the displaced pycnocline; it is subtracted from the background reference state, without any wave-driven disturbance of the pycnocline. The pressure related to the free-surface modulation is obtained by integrating the horizontal acceleration, induced at the top of the water column, in the along-wave direction. The nonhydrostatic pressure is obtained by integrating the vertical acceleration throughout the water column, in the depthwise direction. The hydrostatic pressure is the dominant component. As such, it determines the sign of the total pressure induced by the wave.

Figure 1.2 shows the previously defined wave properties, based on a mode-1 ISW of depression propagating in the Monterey Bay Shelf. The data was obtained from Acoustic Current Doppler Profilers (ADCPs) and pressure sensors located at the bed. The Figure is courtesy of Dr. Ren-Chieh Lien from APL-UW. In Figure 1.2(a), the black-solid lines correspond to the isopycnals; the mode-1 wave-driven perturbation displaces the isopycnals from their reference position. The ISW propagates from right-to-left, as indicated by the purple arrow above. In addition to the isopycnals, contours of the horizontal velocity, U, are

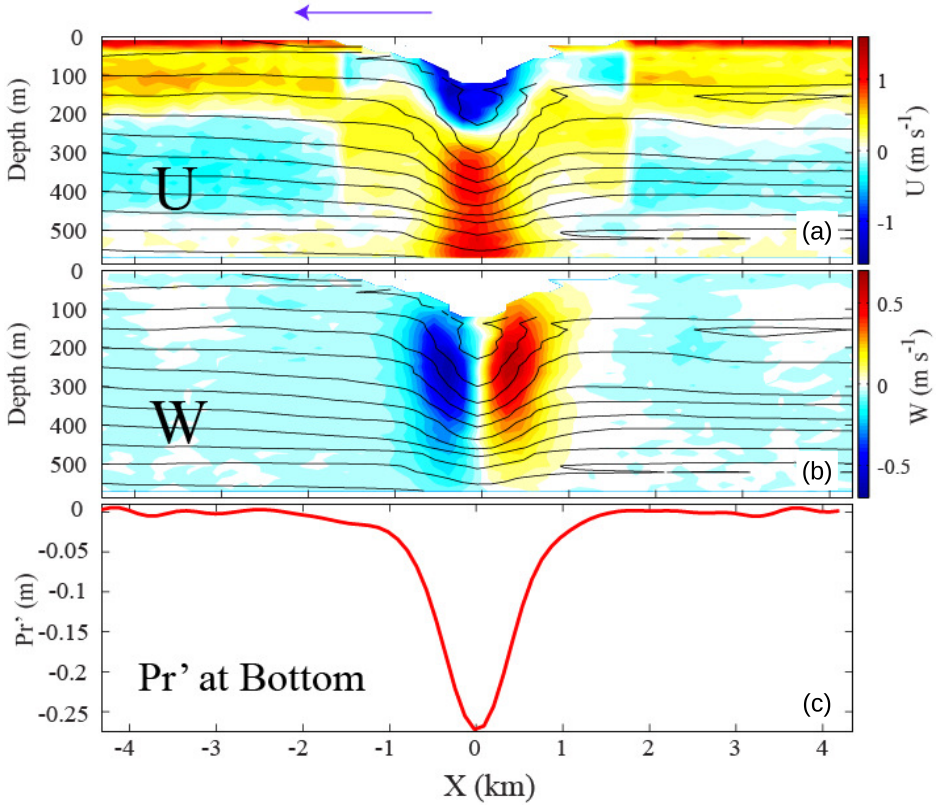

Figure 1.2: Field measurements of the velocity and pressure induced by a mode-1 NLIW of depression. In (a) and (b), the black solid lines correspond to the isopycnals. The horizontal velocity is shown in (a) while the vertical velocity in (b). The total pressure is included in (c), in units of length. Above the horizontal velocity in (a), the purple arrow indicates the direction of propagation. The figure is courtesy of Dr. Ren-Chieh Lien from the University of Washington-Applied Physics Lab.

also shown. Above the wave trough, the horizontal velocity is in the direction of propagation and below the trough, U is positive. In 1.2(b), the ISW-induced vertical velocity is shown; negative vertical velocity is induced ahead of the trough, and positive vertical velocity behind. Figure 1.2(c) shows the total ISW-induced pressure at the bed. Since the ISW is a mode-1 depression-type, the total pressure is negative.

1.3 Importance of mode-1 Internal Solitary Waves in the Stratified Ocean

The earliest observations of mode-1 ISWs in the ocean can be traced back to the 1950's and 1960's. At the time, their presence was mainly relevant to the impact on undersea structures [137]. Recently, they have been found to cause significant change in water column properties, providing a crucial link to large scale oceanic processes. For instance, ISWS have been observed to induce mixing and transport nutrients across the water column [156, 31, 121], resuspend sediment [25, 142, 144, 3, 50], and impact the stability of bottom-lodged structures [137, 136].

Figure 1.3 shows a time series of echosounder measurements displaying a ISW of depression propagating over variable bathymetry, in the South China Sea. Below the ISW, field observations indicate the presence of dunes of $O(10m)$ in amplitude by $O(100m)$ in wavelength [144]. In addition, a layer of resuspended sediment and other particulates from the bottom bed is also shown; this layer is known as a Nepheloid Layer [115]. ISWs may contribute to the persistence of this layer because their propagation is characterized by an adverse pressure gradient at the lee of the wave, that separates the bottom boundary layer [20, 43, 28, 169]. Furthermore, ISWs of depression induce a negative pressure at the bed, capable of seeping material from the pores and into the water column [134].

As the ISW propagates over variable bathymetry, it tries to conserve its energy by adjusting to the changing water depth; this adjustment process is known as shoaling. Shoaling may, in fact, result in wave breaking [83, 185, 71,

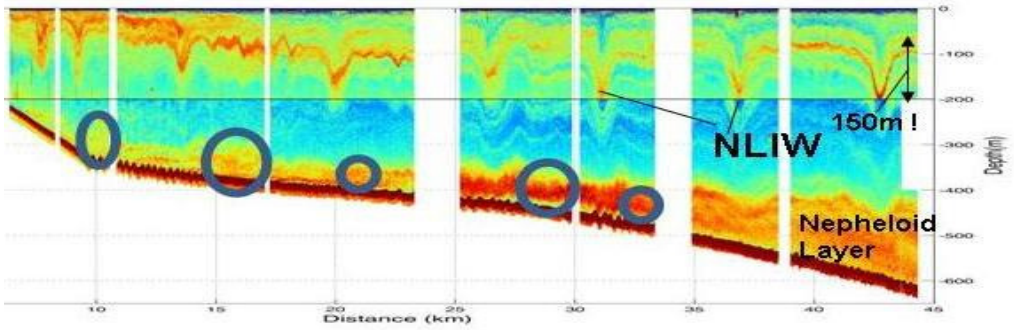

Figure 1.3: Time series of an echsounder image of a Nonlinear Internal Wave of depression propagating over variable bathymetry in the Northern South China Sea. The NLIW has an approximate amplitude of 150m. Above the bottom bed, five gray circles denote the location of dunes. The image is courtesy of Dr. Ben Reeder from the Naval Post Graduate School.

69] that induces transport of mass and momentum, dissipation of kinetic energy, and mixing of the fluid in the water column. The dominant breaking mechanism may be either a convective instability [75, 64] or a shear instability [125].

A convective instability occurs when the maximum horizontal ISW-induced velocity exceeds the wave propagation speed. Heavy fluid enters, from the rear of the wave, into the region above the maximum isopycnal displacement, where lighter fluid resides [148, 135, 152, 117, 183]. A shear instability may occur as the wave grows in amplitude, pinching the pycnocline and increasing the shear at the trough. The most observed shear instabilities are of Kelvin-Helmholtz type [83, 18, 55, 125, 63, 56, 14, 97]. Both instabilities may be present during shoaling [28].

1.4 Modeling the Propagation of Internal Solitary Waves of depression: A Spectral Multidomain Penalty Method-based Approach

The propagation of an Internal Solitary Wave is a fully nonlinear and nonhydrostatic process that encompasses a broad range of length scales. Furthermore, the covered distance, as well as the wavelength and amplitude, may be of $O(km)$, but when the wave shoals, the lengths scales that characterize the dynamically evolving flow may be much smaller (i.e. $< O(m)$). Consequently, modeling the wave propagation demands a highly accurate numerical tool that can capture the physical aspects, with minimal artificial dissipation and dispersion. The discretization of the governing equations using a low-order scheme can accomplish this objective [93, 54, 99], but in the context of static grids, the associated computational cost may be prohibitively expensive, given the required resolution to model the flow scales.

To this end, a high-order spectral technique for solving the governing equations provides the most accurate approximation of the solution, while being bounded by an error that decays exponentially with the order of the polynomial basis [73]. By incorporating an element-based technique, the computational domain can be partitioned into subdomains; these could be concentrated in regions of the flow where higher resolution is desired. In highly turbulent flows (i.e $Re > 10^5$), flexibility in the subdomain positioning allows for the treatment of strongly localized and energetic regions without over resolving less active parts of the flow [41]. A low-order scheme may incorporate a mesh-refinement technique that can provide further resolution in regions of interest [157, 79], but

the high-order spectral technique, with concentrated subdomains, still yields unsurpassed accuracy [40, 73]. Thus, a spectral multidomain method may provide an accurate representation of the propagation of an ISW, for a fraction of the computational overhead needed for low-order schemes with minimal dispersive errors.

The spectral multidomain penalty method, used by the Diamessis Research Group, was originally developed for the study of turbulent wakes in stratified flows [41]. It has been successfully implemented over a wide range of high Reynolds number and environmental fluid mechanic problems including: bottom boundary layer instabilities beneath surface and internal solitary waves [43, 151, 150], internal gravity wave beams interacting with the pycnocline [193] and stratified turbulent wakes [44, 45, 194, 195]. The method spectrally solves the incompressible Navier-Stokes Equations under the Boussinesq Approximation [92] by penalizing the discretized operators [58, 59, 73] and applying a spectral filter, considered to be a stand-alone subgrid-scale model [42]. As such, it may be applied to study environmental flows associated with the propagation of ISWs.

1.5 Examining the Propagation of an Internal Solitary Wave of depression

In this dissertation, three numerical studies are presented, focusing on the interaction of the ISW with the bottom bed and the water column, separately, in constant or progressively shallower water depth. Each one addresses a particular problem that is both unique and beneficial for the oceanographic commu-

nity. One has been published in a scientific journal [145], while the other two are being prepared for submission to refereed journals as well.

In the first study, the impact of the ISW-induced pressure on the bed is examined. While the ISW-induced shear may be enough to cause sediment resuspension [3], in the case of both depression and elevation-type waves [88, 159, 31, 142], there is no study that address the impact of the pressure in the context of a highly nonlinear propagating ISW of depression, where the response of the bed varies with time. Of particular interest is the case where the bed fails as a consequence of a high vertical pore-pressure gradient. For instance, surface waves induce bed failure by generating large pressure gradients, capable of causing either piping or liquefaction. It may occur from a single wave propagation event, from the prolonged exposure of the bed to progressive waves, or storm wave events. These examples of failure are caused by the increase in the vertical pore-pressure gradient, that may be larger than the buoyant weight of the bed. Piping refers to the process by which fluid is extracted from the bed. On the other hand, liquefaction is the process by which the soil looses its rigidity and behaves like a fluid. ISWs of depression, with much larger length and time scales, induce a negative pressure at the bottom, that is strong enough to draw fluid from the porous bed; the larger the wave the stronger the induced pressure gradient. Their large induced pressure may be sufficient to cause liquefaction as well. Once failed, the loose material is more susceptible to resuspension and transport.

The second study examines the adiabatic shoaling of large amplitude ISWs of depression. Field observations [102, 103] indicate that over gentle slopes (< 0.03), the waves do not lose their energy to wave fission, or dispersion,

but rather experience convective breaking, dissipate their kinetic energy, mix the fluid in the water column, and transport mass while retaining their shape. These waves are known to propagate with a trapped, or recirculating core, that transports material into the shallower continental shelf waters. Field observations have only been able to show the properties of the fluid engulfed within the trapped core, at a fixed location in the South China Sea, and prove the presence of a convective instability. However, little is known as to how the cores form and whether it is a localized event, tied to a particular oceanographic region, or perhaps a more common phenomena that is seldom observed. Only a partial description of time-evolution associated with wave propagation is known. It is very challenging, and costly, to probe the wave over large distances, that are on the $O(100km)$. As such, a high fidelity simulation can complement the field observations and perhaps generate a new vision on the role of convective instabilities in shoaling of ISWs of depression over gentle slopes.

The third and final study focuses on the formation of the convective instability in a three-dimensional framework. The subsurface recirculating core is inherently three-dimensional; it dissipates turbulent kinetic energy and mixes the fluid in the water column. However, little is known as to how the convective overturn, that leads to a subsurface core formation, can occur in the presence of any lateral instability. In addition, the role of the background current in the wave energetics is explored; the current corresponds to an active source of kinetic energy during shoaling. Overall, this study study will complement the two-dimensional work introduced in the second study, and lay the foundation for future simulations that will examine the turbulent flow within the subsurface recirculating core and the mass transport capability of the wave.

1.6 Outline of the Dissertation

This dissertation focuses on three problems related to the propagation of the ISW: one over a flat bed and two over gently varying water depth. Each study has its own Chapter, that includes an Introduction to the the problem along with driving questions, a Methodology section describing the modeling approach and initial conditions, a Results section describing the outcome of the simulations, and a Discussion section addressing any outstanding outcome. The last Chapter of the dissertation contains an overview of the results of each study, and future work. The Appendix includes the equations used to generate the initial conditions of each study.

In Chapter 2, the interaction between the ISW induced pressure and the bed is explored. The governing equations for pore-pressure are presented, along with the high-accuracy computational method, an a discussion on the possibility of ISWs causing bed failure. As part of the study, the properties of the water column and bed are varied to examine which conditions are ideal. The results of this study were published in the Journal of Geophysical Research: Oceans[1].

Chapter 3 examines the formation of convective instabilities in ISWs of depression in the South China Sea (SCS), in a two-dimensional context. The study aims to complement the field observations of Dr. Ren-Chieh Lien, and his team. In two separate deployments in the SCS, the team was able to observe subsurface recirculating cores. No other location in the world is known to exhibit ISWs with this particular features. Their large scales makes field observations very challenging thus motivating a computational-based approach to explore

[1]Rivera-Rosario, G.A., P.J. Diamessis, and J.T. Jenkins (2017), Bed Failure induced by internal solitary waves, J. Geophys. Res. Oceans, 122, 5468-6485, doi:10.1002/2017JC012935.

the shoaling process in this region. The chapter begins with a brief discussion on ISWs with recirculating cores, followed by the underlying problem and questions to try and address Dr. Lien's observations. A discussion on the field conditions, governing equations, and computational approach ensues. Results are presented, along with variations of the initial conditions that address the wide parameter space of the problem.

Chapter 4 builds from the two-dimensional study of Chapter 3 and focuses on the formation of the convective instability in a shoaling ISWs of depression, but with a three-dimensional framework. A brief introduction of the problem is presented, along with the governing equations in three-dimensions. The computational domain is also shown including the choice of boundary conditions for the lateral domain. Results include characterizing the lateral instability during convective breaking, examining the role of the background current in the ISW energetics, and describing the spanwise evolution of the velocity and density field, due to the preceding convective instability, in a shoaling ISW of depression over gentle slope. As mentioned earlier, under such low slope values, the ISW does not breakdown, but rather retain its symmetric shape as it propagates into the shallower waters of the continental shelf.

Lastly, Chapter 5 includes the concluding remarks of this dissertation. Remarks on possible future work are also discussed. Supplemental material is included in Appendix A.

CHAPTER 2

THE PRESSURE INDUCED AT THE BED BY A PROPAGATING INTERNAL SOLITARY WAVE OF DEPRESSION

2.1 Introduction

Nonlinear internal waves are capable of inducing significant pressure in the water column and upon the seafloor during their passage. They are ubiquitous phenomena in the stratified ocean, that produce isopycnal displacements which are a significant fraction of their wavelength. NLIWs are frequent in the stratified ocean, having been observed across the globe [77, 192, 143, 104, 25, 174, 31, 186, 126, 161, 142]. The depths across all locations vary substantially and, consequently, so does the wave-bed interaction. Understanding this connection is of interest in terms of sediment resuspension which may influence the bed morphology [144, 50], nutrient access for organisms living far away from the bed [3, 142] and the integrity of bottom-lodged structures [17, 130, 61, 170].

As mentioned in Chapter 1, a particular and frequently occurring form of NLIWs are Internal Solitary Waves (ISWs) [68]. ISWs are either depression-type or elevation-type, depending on the direction of the displacement of the pycnocline and its location with respect to the mid-depth of the water column. The total induced pressure at the bed, a combination of both hydrostatic and nonhydrostatic contributions [127], follows the displacement of the pycnocline; waves of elevation induce a positive total pressure at the bed, while waves of depression induce a negative total pressure. The first studies of the changes in pore-pressure induced by interfacial waves only considered a spatio-temporal periodic train of waves, with amplitudes much smaller than the wavelength

[34, 187]. Under such context, the internal-wave induced pressure, at the bottom of the water column, may be obtained from the solution of an eigenvalue problem in the vertical direction. However, the assumption of small interfacial oscillations, compared to the wavelength, is not an accurate representation of highly nonlinear internal solitary waves. Given the large amplitude, the ISW-induced pressure at the bottom of the water column will be significantly different from that obtained for the linearly approximated interfacial waves.

In environments where ISWs are found, the bed can be considered as a continuum with varying properties. In situ sampling of the bed material indicates the presence of fine sands to silts and clay at water depths between 60m to 80m at the Stellwagen Basin [25], fine sands, gravel and silts with their respective concentration varying with water column depth in the Nazaré Canyon [142], and medium to fine sands in the Northern South China Sea [144]. Thus, the bed composition varies substantially and the pore-pressure response will not be the same across these different marine environments, because, by Darcy's Law, seepage is a function of the bed properties.

Important features of the bed composition are its conductivity, stiffness and saturation. For a fine material of weak conductivity, the stiffness of the bed and its saturation dictate how pressure changes associated with the passing of a wave are transmitted through the medium [190]. Stiffer beds, in the absence of saturation, transmit pore-pressure changes quickly. Furthermore, bed saturation, a measure of the amount of trapped air or gas, plays a critical role, because its compressibility contributes to the attenuation of pore-pressure near the top causing bed failure, or momentary liquefaction [15]. The bed failure is the result of a vertical pore-pressure gradient larger than the buoyant specific weight

of the porous medium. The exact source of the trapped gas is not known, but some authors attribute it to the decomposition of organic material [176]. Others argue that, if the bed is exposed to air during a low tide event, trapped air within the bed is possible, once it becomes again fully submerged [118]. Thus, wave-induced pore-pressure changes can result in failure, as a consequence of pore-pressure build up, for the appropriate combination of both the bed constituent and saturation.

Observations in coastal environments, as well as laboratory experiments and numerical simulations, have identified the occurrence of wave-induced bed failure, but only for surface waves. These surface wave studies include those on trains of waves of the same amplitude [158] and the passage of the trough of the leading progressive surface wave [153]. Simulations include solitary surface waves [105], in which the presence of trapped gas in the bed is considered important. Furthermore, analysis of soft-sediment deformations in the Guadalquivir Basin and the Betic Cordillera has supported the possibility of bed failure due to surface wave action [120, 7]. Conclusions about potential bed failure were based on theoretical work that stated that only strong horizontal pore-pressure gradients can cause failure [15, 110]. However, the vertical pressure gradient may induce failure over a nearly saturated bed, if the wave trough is deep enough [171]. In such circumstances, fluid seeps vertically from the bed, potentially displacing bed particles. Only wave events with a strongly-induced negative pressure are capable of causing such failure.

ISWs of depression have the capacity to induce a strong negative pressure and, consequently, their passage could result in bed failure. For instance, below sluggish ISWs of depression, vertical seepage is greatly enhanced, resulting in

fluid being drawn from the bed and, possibly, contributing to the resuspension of particles [134] . If the assumption of very slow motion is disregarded, then time-dependence is introduced. Under such circumstances, the compressibility of the soil skeleton and the fluid need to be accounted for [111]. As noted earlier, such time dependence has only been explored with surface wave-bed interaction and small amplitude and, periodic internal waves, but not with strongly nonlinear internal solitary waves of depression.

The above discussion motivates further consideration of bed response under the presence of an internal solitary wave. This chapter seeks to characterize the ISW-induced pressure field and its capacity to fail the bed for a depression wave. The pressure evolution inside the bed is modeled using a high-order numerical scheme. The primary objective is to identify thresholds of stratification, key wave properties and the soil constituents that result in bed failure. Ultimately, the motivation is to highlight the role of the ISW-induced vertical pressure gradient during bed failure, with the aim of driving future field measurements to test the results of this study.

The presentation of this Chapter is as follows: Section 2.2 discusses the methodology employed to solve the governing equations in porous media flow. The problem geometry, with the relevant underlying assumptions, precedes the discussion of the numerical method, including the choice of boundary conditions. Particular emphasis is placed on the role of soil and fluid compressibility and how the bed and water column are modeled. Section 2.3 contains the results of the simulations, detailing both the induced pore-pressure and vertical pore-pressure gradient. The latter is expressed in the context of the ratio of the dimensional vertical pore-pressure gradient to the buoyant specific weight

of the porous medium. Section 2.4 contains a discussion of field observations of the changes in pore-pressure due to surface waves, including possible bed failure, a discussion of the pressure induced by ISWs of elevation, the connection between shallow and deep water environments, including the role of the ISW-induced free surface displacement in the total pressure, and the possible enhancement of particle resuspension due to the vertical pore-pressure gradient.

2.2 Methodology

2.2.1 Problem Geometry: Water Column and Wave-Forcing

Figure 2.1 illustrates both the water column, ISW and the porous medium in the model computational domain used for the present problem. On the water side, a two-layer continuous density stratification is assumed. The pycnocline displacement is driven by a depression wave with an amplitude A, half-wavelength L_W, and a propagation speed c. The half-wavelength is defined as the integral of the pycnocline displacement in the streamwise divided by the amplitude [90]. The top layer, of thickness h_1, has a density ρ_1, lighter than that of the bottom layer with thickness h_2 and density ρ_2. The bed is treated as a uniform continuous layer of either either sand or silt with thickness L_η.

The wave velocity and density fields are obtained from fully nonlinear theory based on the Dubriel-Jacotin-Long (DJL) Equation, [106, 179] using a nonlinear eigenvalue solver [52]; it generates an exact solution to the incompressible Euler equations under the Boussinesq approximation in a reference frame, $x-z$,

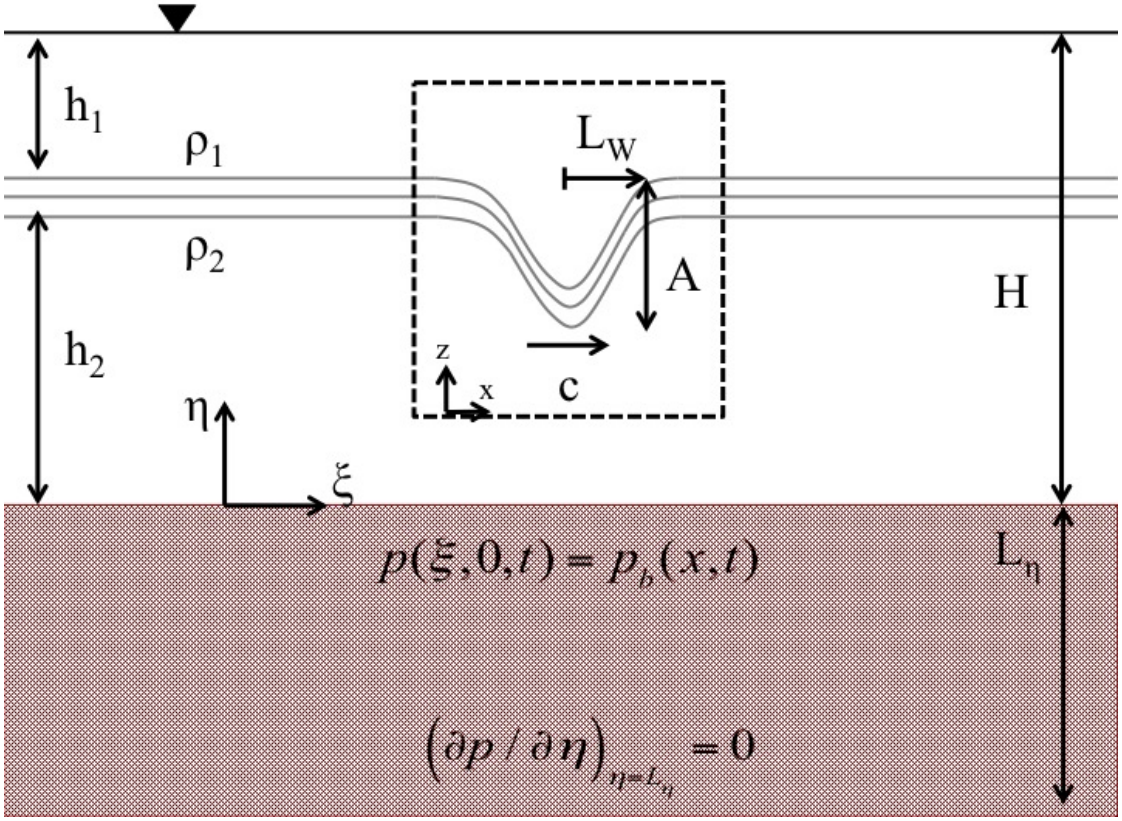

Figure 2.1: Problem Geometry for an ISW of depression propagating over a uniform bed of thickness L_η. The wavefield velocity and density perturbation are computed in a reference frame, $x - z$, moving with the wave. The bed lies in a fixed reference frame, $\xi - \eta$. The boundary conditions of the porous medium are also shown. In addition, periodicity is assumed in the streawise direction.

traveling with the wave. The DJL Equation is presented in Appendix A. The bed is in a fixed reference frame $\xi - \eta$; both the moving and fixed reference frame can be related via a Galilean transformation. Correspondingly, the wave imposes a translating boundary condition on the fixed frame. In the present study, for a given water depth, H, pycnocline location, thickness and reference density, the available potential energy (APE) [96] of the downward wave-displaced pycnocline is specified initially, generating an ISW with the minimum kinetic energy. The APE is defined as the minimum energy required to adiabatically bring a parcel of fluid from its displaced location back to its reference location.

Subsequently, the available potential energy is progressively increased until the largest wave-induced depression is attained, for the particular stratification profile. Lastly, the wave amplitude is the maximum isopycnal displacement given the specified APE.

Only two components of the wave-induced pressure are considered for this part of the study: the hydrostatic pressure due to the wave driven density perturbation (p_{wh}) and the non-hydrostatic pressure (p_{nh}), which is a function of the vertical accelerations within the wave [127]. The ISW-induced free-surface displacement, and its corresponding pressure, is not accounted for. Its influence is addressed separately in the discussion section. The first two pressure components are given by

$$p_{wh} = \int_z^H \rho_w g dz', \tag{2.1}$$

and

$$p_{nh} = \int_z^H \rho_o \frac{Dw_w}{Dt} dz', \tag{2.2}$$

where D/Dt, the material derivative, for a wave traveling without change in form, is expressed as

$$\frac{D}{Dt} = (u_w - c)\frac{\partial}{\partial x} + w_w \frac{\partial}{\partial z}. \tag{2.3}$$

In Equations (2.1) and (2.2), ρ_w is the wave-driven density perturbation, u_w and w_w are the wave-induced horizontal velocity and vertical velocity, respectively,

ρ_o is the reference density, g is the gravitational acceleration, and c is the wave propagation speed. The reference density is chosen as the value of the density in the middle of the pycnocline. The total wave-induced pressure is the summation of p_{wh} and p_{nh}, and its value at $z = 0$ is set as the boundary condition at the top of the bed.

2.2.2 Problem Geometry: Bed

A porous bed, subjected to a constant vertical load, can be considered laterally confined if the horizontal dimension is much larger than the vertical [182]. Under such circumstances, any horizontal deformation may be neglected, and the bed will compress in the direction in which the load is being applied. Thus, the change in pore-water pressure, p, derived from conservation of mass [15] inside the porous bed, can be expressed by

$$\frac{k}{\rho_o g} \nabla^2 p = (\alpha(z) + n\beta') \frac{\partial p}{\partial t}. \tag{2.4}$$

In Equation (2.4), the bed compressibility, α, is taken to vary in the vertical direction. This parameter relates the changes in void ratio to the changes in effective stress, and shall be addressed in the subsequent section. The bed, with a porosity of $n = 0.30$, is considered to be isotropic, meaning that the conductivity, k, is independent of orientation in space. Its value can be obtained from experimental data, field observations or through analytical expressions using the soil relative density and the particle diameter [101]. Table 2.2.2 presents the bed classification, considered in this study, based on the particle diameter and the corresponding conductivity.

Table 2.1: Properties of the porous bed used in this study

Material	Diameter (μm) [25, 144]	Conductivity (ms^{-1}) [101]
Medium Sand	200	8.0×10^{-5}
Fine Sand	100	2.0×10^{-5}
Coarse Silt	40	3.2×10^{-6}
Medium Silt	20	8.0×10^{-7}

Finally, the fluid compressibility inside the bed is considered through the parameter β', which accounts for a small amount of trapped gas. The response of the bed under a fully saturated porous medium is not explored, as it was originally thoroughly addressed for surface waves and is not necessarily representative of wave-induced bed response [122, 111].

Bed Compressibility

The deformation of the bed is modeled using Lamé's parameters, which describe the elastic behavior of the continuous medium [24]. The response, is assumed to be a function of space, described by effective Lamé's parameters, considering non-cohesive particles [46]. This formulation is presented in Appendix A. The corresponding vertical effective stress is denoted as $\sigma_\eta = (\rho_s - \rho_o)g\eta$, where η is the vertical coordinate in the bed and ρ_s is the particle density, taken to be that of quartz, 2650 kgm^{-3}. The presence of the coordinate η, in the effective vertical stress, indicates that the compressibility will vary in the vertical direction. The bed is assumed to be laterally confined, which implies that there will be no horizontal displacements. The vertical dimension of the bed, L_η, is taken to be much less than its horizontal dimension. The vertical bed compressibility is then

$$\alpha(z) = \frac{1}{(2\bar{\mu}(z) + \bar{\lambda}(z))}, \tag{2.5}$$

where $\bar{\lambda}$ is Lamé's effective first parameter and $\bar{\mu}$ is the effective shear modulus. The calculation of the compressibility begins five particle diameters into the bed, making this vertically offset location effectively the top of the bed.

Equation (2.5) indicates that stiffer materials have a lower degree of compressibility. With quartz as the main soil particle constituent, α is found to smoothly vary from 10^{-7} $(Nm^{-2})^{-1}$ at the top of the bed to 10^{-9} $(Nm^{-2})^{-1}$ at the bottom of the bed, for both sand and silt. Larger values of α correspond to the top of the bed, where the effective stress is smaller.

Bed Saturation

In a nearly saturated porous medium, the fluid compressibility is expressed as function of the amount of trapped gas. The fluid compressibility, β', may be given as [181, 15]

$$\beta' = \beta + \frac{1 - S_r}{p_o}. \tag{2.6}$$

Here, S_r is the fraction of trapped gas, β is the bulk modulus of water, $\beta = 2.3 \times 10^9$ $(Nm^{-2})^{-1}$, and p_o is the absolute pore-water pressure. The latter is the background hydrostatic pressure at the bottom of the water column, without the presence of an internal solitary wave. The values of S_r are chosen as 0.97 and 0.99 for all depths [61, 176, 118]. However, it is emphasized that actual field observations of how much gas is trapped at the depths considered by the

present study is not well documented and caution should be exercised when extrapolating values of S_r used here to the field.

2.2.3 Numerical Method

To solve Equation (2.4) numerically, a Fourier-Legendre collocation method is utilized. Through a Fourier discretization in the horizontal periodic direction and a single domain Legendre-polynomial collocation scheme in the vertical direction, higher-order accuracy is achieved [91]. Temporal advancement is performed via an implicit third-order backward differentiation scheme [138]. Figure 2.1 indicates the relevant boundary conditions. The domain is taken to be long enough to avoid any interaction between the ISW-induced pressure signal inside the bed and its periodic image. At the top of the computational domain, a time dependent Dirichlet boundary condition for the wave-induced pressure is imposed. As the wave moves from left to right, the pressure field at the bottom of the water column is interpolated onto the computational grid by cubic splines, using the Galilean transformation $\xi = x - ct$. The bottom boundary condition is a no-flux Neumann boundary condition, representing an impervious layer below the porous bed. In addition, the computational grid is composed of $\left[N_\xi, N_\eta\right]$ grid points in the horizontal and vertical direction, respectively. The timestep is $\Delta t = \Delta\xi/c$, where $\Delta\xi = L_\xi/N_\xi$.

2.2.4 Simulation Description

Application of the algorithm to solve the DJL equation [52] requires supplying the available potential energy, pycnocline thickness, δ_{pyc}, and a density difference of $\Delta\rho$. The dependency between the maximum allowable wave amplitude and the resulting pressure is explored in a sequence of test runs to determine which stratified environment yields the largest ISW-induced pressure. The water depth is taken to be $H = 50$m, typical of continental shelf environments, where nonlinear internal waves and internal solitary waves have been observed [126, 31] and also where the bed properties have been sampled. Three possible pycnocline thicknesses are selected, $\delta/H = 0.02$, $\delta/H = 0.04$ and $\delta/H = 0.06$ [98], along with the two-layer continuous density thickness ratios of $h_1/h_2 = 1/3$, $1/5$, $1/7$ and $1/10$, typical of oceanic and coastal observations of ISWs. Consistent with the Boussinesq approximation of small relative changes in density, the density jump across the two-layer setting is specified as $\Delta\rho = 40$ kgm^{-3}, with a reference density value of $\rho_o = = 1020$ kgm^{-3}, similar to laboratory experiments [118] and environments with fresh, lighter water on top of saltier, heavier water [21]. The reference density is the density at the middle of the pycnocline. The characteristic ISW properties for the above stratification parameter values are shown in Table 2.2.

With the obtained ISW-induced velocity and density fields, the hydrostatic and non-hydrostatic contributions to the pressure at the bed are computed via trapezoidal integration of Equations (2.1) and (2.2) using Matlab's *trapz*, which is spectrally accurate for the Fourier grid of the DJL solver [22]. The pressure at the top of the bed is taken to be the total pressure at the bottom of the water column ensuring a one-way coupling between the wave-induced pressure field

Table 2.2: Properties of Internal Solitary Waves Based on Stratification Parameter Space

δ_{pyc}/H	h_1/h_2	Amplitude (m)	Bottom Pressure (Nm^{-2})
0.02	1/3	-5.2750	-1,833
	1/5	-6.5499	-2,042
	1/7	-7.3475	-2,105
	1/10	-7.7720	-2,027
0.04	1/3	-9.8744	-3,483
	1/5	-12.0698	-3,852
	1/7	-11.9231	-3,434
	1/10	-12.8987	-3,409
0.06	1/3	-12.8337	-4,691
	1/5	-16.2443	-5,594
	1/7	-17.4837	-5,602
	1/10	-17.6312	-5,015

and pore-pressure changes. With the above choices of pycnocline thickness, the test cases shown in Table 2.2 agree with previous studies [98]. Thicker pycnoclines are found to support higher amplitude waves. Therefore, for high bottom pressures induced by ISWs of depression, the pycnocline thickness should be $\delta_{pyc}/H \geq 0.06$ and the two-layer continuous density thickness ratio should be $h_1/h_2 \geq 1/5$, as shown in Table 2.2. Finally, there is also a significant decrease in total pressure observed when transitioning from $h_1/h_2 = 1/7$ to $h_1/h_2 = 1/10$, as the wave amplitude increases. This effect occurs because higher amplitude waves also induce a higher non-hydrostatic pressure. Therefore, in the present study, the *baseline case*, is defined as the propagation of an ISW of depression, in a water depth of H = 50m with two-layer ratio of $h_1/h_2 = 1/7$, which yields the highest wave-induced pressure consistently, regardless of the thickness of the pycnocline and wave amplitude, for all values of δ_{pyc}/H and h_1/h_2, as shown in Table 2.2.

Table 2.3 contains the parameters used to simulate the bed response in this study, including the resulting wave celerity and half wavelength for the speci-

Table 2.3: Simulation Parameters for the baseline case

Parameter	Value	Parameter	Value
N_ξ	4096	Δt	0.36 s
N_η	130	$\Delta\xi$	0.73 m
L_ξ	3000 m	c	1.98 ms^{-1}
L_η	50 m	L_W	100 m

fied water column depth and the two-layer continuous density thickness ratio as noted in the baseline case. The domain length is set by comparing the wave propagation and pressure diffusion time scale, with the average value of α, for the porous medium under the given parameters. From Equation (2.4), an effective diffusion coefficient, κ, is obtained by grouping together the constants associated with both the porous medium and the water column. The coefficient is expressed as,

$$\kappa = \frac{k}{\rho_o g(\alpha(z) + n\beta')}, \tag{2.7}$$

with units of length-squared over time, where the overline denotes the vertically averaged soil compressibility in space. Since the diffusive time scale, L_w^2/κ, is larger than that of the wave, L_w/c, a lag of the wave-induced pressure inside the bed will occur once the wave has passed. This phenomenon has been documented for surface wave-induced pressure [190]. Therefore, a domain length of approximately $L_\xi = 30L_W$ is chosen to allow the wave-induced pore-pressure pattern to achieve its full spatial extent, after the ISW has passed a given, fixed location. In addition, this long domain also respects the periodic boundary conditions imposed in the streamwise direction by the numerical scheme. Finally, the choice of bed thickness also respects the requirement of being larger than the diffusive length.

Table 2.4: Values of the vertical scale, η_o, for the baseline case.

Material	$S_r = 0.99$	$S_r = 0.97$
Medium Sand	6.9450 m	4.4309 m
Fine Sand	3.4720 m	2.2150 m
Coarse Silt	1.3884 m	0.8857 m
Medium Silt	0.6943 m	0.4428 m

2.3 Results

An appropriate scaling is sought to present the results in dimensionless form. In this study, the relevant pressure scale is chosen to be that of the hydrostatic pressure of an ISW, $\Delta\rho gA$, which is the larger contributor near the bed. The relevant horizontal length scale is the half wavelength, L_W, and the time scale is that of the propagating wave L_W/c. The vertical dimension is scaled by the diffusive depth, $\eta_o = \sqrt{\kappa L_w/c}$. The values of η_o, used in this study for the baseline case, are presented in Table 2.4, for saturation values of $S_r = 0.99$ and $S_r = 0.97$.

Thus the nondimensional parameters used in this study are expressed as,

$$\begin{cases} p^+ = \frac{p}{\Delta\rho gA}, \\ \eta^+ = \frac{\eta}{\eta_o}, \\ \xi^+ = \frac{\xi}{L_W}, \\ t^+ = \frac{t}{L_W/c}. \end{cases} \tag{2.8}$$

From the solution of the DJL Equation, for the baseline case, the hydrostatic and nonhydrostatic pressure can be computed using Equation (2.1) and Equation (2.2), respectively. The ISW-induced pressure, at the bottom of the water column, is presented in Figure 2.2, in a reference frame moving with the wave. For an ISW of depression, the total pressure is negative, because the hydrostatic

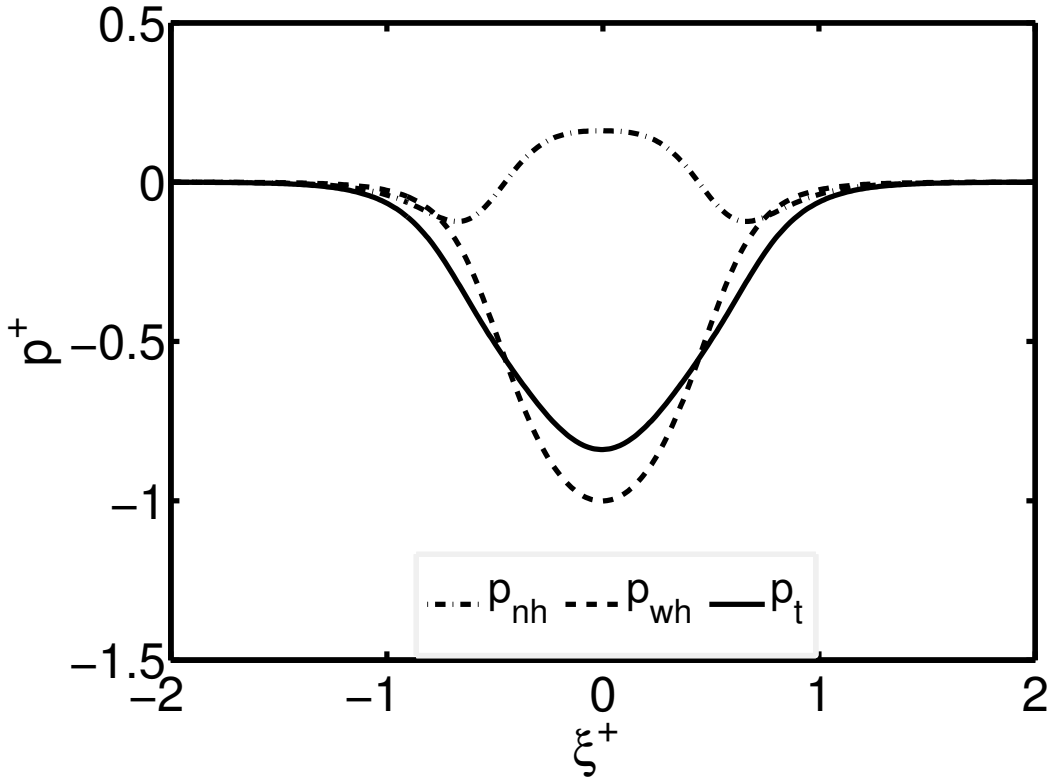

Figure 2.2: ISW-induced pressure at the bottom of the water column for a two-layer, continuously stratified water column with a thickness ratio of $h_1/h_2 = 1/7$ in a water depth of H = 50m (baseline case). The pressure is computed in a reference frame moving with the ISW. The dash-dash line corresponds to the hydrostatic pressure defined in Equation (2.1), the dash-dot line corresponds to the non-hydrostatic pressure, defined in Equation (2.2), and the solid line is the summation of both p_{nh} and p_{wh}. ISWs of depression induce a total negative pressure, due to the dominant hydrostatic component associated with the pycnocline displacement.

component is the largest contributor. As previously mentioned, changing from the moving reference to the fixed reference frame involves the Galilean transformation, denoted by ξ, of the total pressure.

The change in pore pressure induced by the passage of the ISW is shown in Figure 2.3, for a partially saturated bed composed of medium-size sand for the baseline case. During passage, the ISW leaves a diffusive imprint similar to that

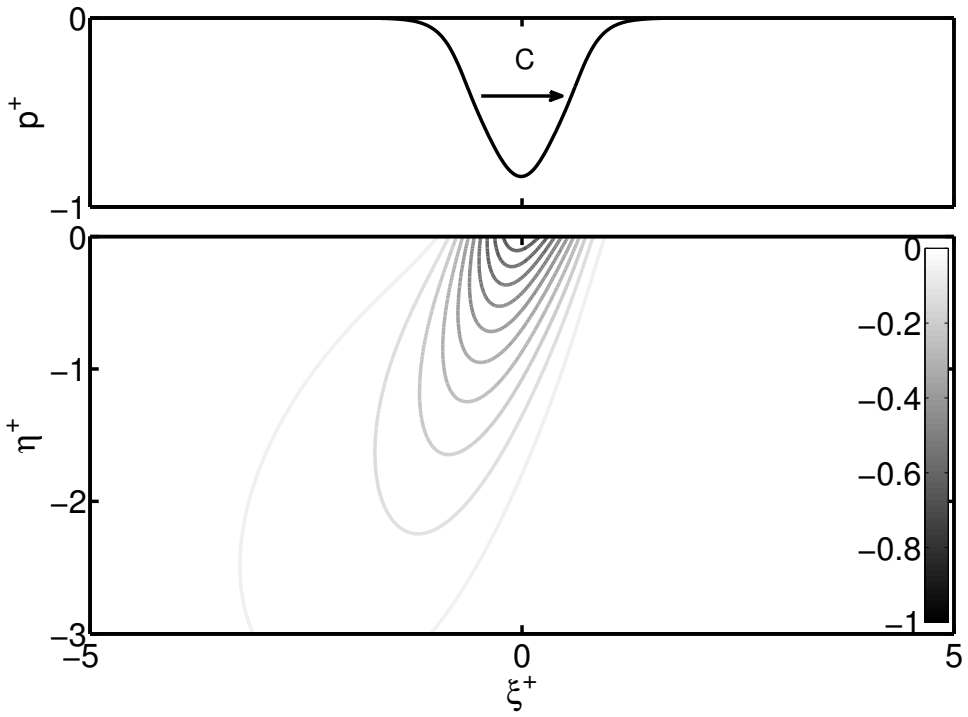

Figure 2.3: Contour of the changes in pore-pressure for a partially saturated bed composed of medium sand, for the baseline case. The ISW travels with celerity c, from left to right. The total ISW-induced pressure, at the bottom of the water column, is shown in the top panel.

under a solitary surface wave [105] . The changes in pore-water pressure not only penetrate deeper into the bed, but persist once the wave has passed.

2.3.1 Vertical profile of the induced changes in pore-pressure

The vertical structure of the change in pore-pressure is shown in Figure 2.4, for a fixed location in the bed with the baseline conditions, during the passage of the ISW. Three instances were chosen to illustrate the change of the pore-pressure: before the wave arrival (Figure 2.4c), directly under the wave trough (Figure 2.4b), and after the wave has passed by (Figure 2.4a). For each location, the

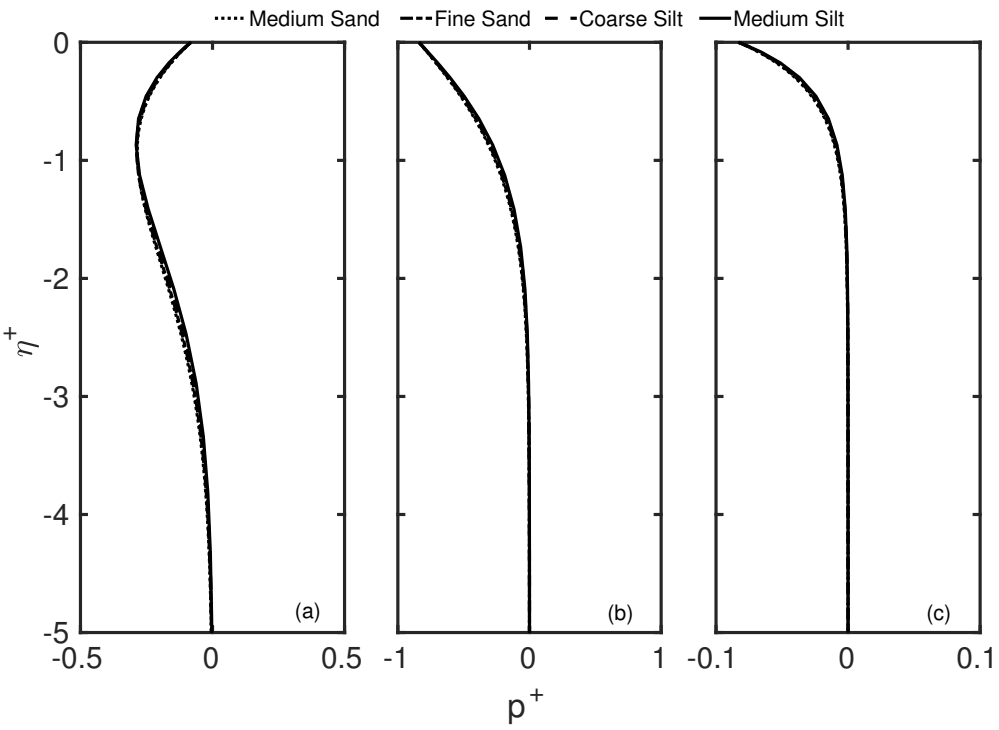

Figure 2.4: Vertical structure of the change in pore-pressure at a fixed location along the bed, during the passage of an ISW of depression, for the baseline case. The ISW propagates from left to right, where (a) is after the passage of the trough, (b) corresponds to the instance under the wave trough, and (c) corresponds to the instance before the arrival of the trough. The dotted, dashed-dotted, dashed, and solid line corresponds to a bed composed of Medium Sand, Fine Sand, Coarse Silt and Medium Silt, respectively. The properties of the bed are included in Table 2.2.2. The scaling parameters collapse the data for both S_r = 0.99 and S_r = 0.97. Note the differences in minimum and maximum values of p^+ in each of the three panels.

range of p^+ has been adjusted, in order to highlight the magnitude of the change in pore-pressure. The instance before and after the arrival of the ISW is defined as the moment at which the ISW-induced pressure is ten percent of the minimum pressure. The remaining bed properties are shown in Table 2.2.2. Since the ISW-induced pressure is negative, the passage induces a deficit in the pre-existing pore-pressure. The deficit is more pronounced under the wave trough and persists after the wave has traveled by.

Table 2.5: Penetration depth, $\eta^{+}_{0.1}$, of the change in pore-pressure during ISW passage.

Material	$\eta^{+}_{0.1}$
Medium Sand	-1.8061
Fine Sand	-1.7378
Coarse Silt	-1.5776
Medium Silt	-1.5776

2.3.2 Depth of penetration for the changes in pore-pressure

A penetration depth, inside the bed, can be computed by considering the depth at which the change in pore-pressure is ten percent of the minimum ISW-induced pressure, located at the wave trough. The depth can be a measure of the extent of the region across which significant seepage might occur. In the present study, this depth is denoted as $\eta^{+}_{0.1}$, and is presented in Table 2.5, for the different bed constituents. Previous studies have considered a penetration depth, as a function of the aspect ratio of the bed, based on sinusoidal pressure wave patterns [134]. This approach essentially serves as a proxy for the ISW-induced pressure of depression-type, forcing the bed. Such analysis has been performed for an observer in a reference frame moving with the wave. In addition, the dependency of the penetration depth on the pressure signal itself was evaluated by changing the wavelength content of the sinusoidal pressure forcing. It was found that for long wavelength perturbations, the penetration depth increased and this depth was further enhanced by increasing the domain length. Thus, internal solitary waves, with a characteristic long wavelength, induce a change in pore-pressure that penetrates deeper into the bed. The results presented in Figure 2.4 indicated that, for a bed composed of a more conductive material, such as medium sand, the penetration depth approaches a distance comparable to the wave amplitude.

2.3.3 Variation of vertical pore-pressure gradient

For a bed material that is less conductive, the deficit in pore-pressure does not penetrate deeper into the bed. If the soil saturation is reduced from $S_r = 0.99$ to $S_r = 0.97$, the corresponding increase in the concentration of trapped gas enhances the build-up of pore-pressure for all materials, giving rise to steeper gradients. The vertical pore-pressure gradient can be a measure of vertical seepage within the bed and, consequently, of possible failure. The gradient can be compared to buoyant specific weight of the porous medium, γ_s, and can determine whether momentary liquefaction can occur [15]. This parameter is expressed as,

$$\gamma_s = (1 - n)(\rho_s - \rho_o)g, \tag{2.9}$$

where ρ_s is the particle density of quartz, 2650 kgm^{-3}. Therefore, bed failure occurs if the vertical pore-pressure gradient is larger than the buoyant weight of the bed, or $-\partial p/\partial \eta \geq \gamma_s$. The sign convention distinguishes between the wave-induced pressure gradient, in the water column, and the vertical pore-pressure gradient inducing upward seepage, within the bed, during the ISW passage. Making the vertical pore-pressure gradient dimensional and, normalizing it by the buoyant weight of the bed, yields the failure criteria as,

$$\Gamma \geq 1, \tag{2.10}$$

where

$$\Gamma = -\frac{\partial p^+}{\partial \eta^+}\left(\frac{\Delta \rho g A}{\gamma_s \eta_o}\right). \tag{2.11}$$

In the present work, the seepage is not symmetric about the wave trough, because the pressure forcing is translating along the bed. As such, the maximum magnitude of vertical pressure gradient is not under the wave trough, as one would expect for a forcing independent of time [134]. The dimensional vertical pore-pressure gradient normalized by the buoyant weight of the bed, for the baseline case, is shown in Figure 2.5, for saturation values $S_r = 0.97$ and $S_r = 0.99$. The gradient is obtained by spectrally differentiating the simulated pressure field [91]. The position, along the wave, at which the maximum magnitude of the vertical pore-pressure gradient is located indicates that subsequent onset of vertical seepage begins before the trough has passed by $\xi^+ \approx 0.5$. When the saturation is decreased from $S_r = 0.99$ to $S_r = 0.97$, the gradient is strong enough to overcome the submerged specific weight and, possibly, cause bed failure.

A measure of the thickness for the failed layer can be obtained by delineating, along the bed, where the condition expressed in Equation (2.10) is valid. In Figure 2.6, the dashed line demarcates the lower boundary of the region where the vertical pressure gradient is higher than the buoyant specific weight of the porous bed. This region is computed to be approximately $\eta^+ = -0.1741$. In addition, the penetration depth, as defined in Section 2.3.2, is also shown in Figure 2.6, and is found to be approximately $\eta^+ = -1.7351$. This scenario suggests that, for a bed with a weak conductivity, the changes in pore-pressure impact approximately the top one meter of the bed, with only 2% of the thickness of the bed subject to failure.

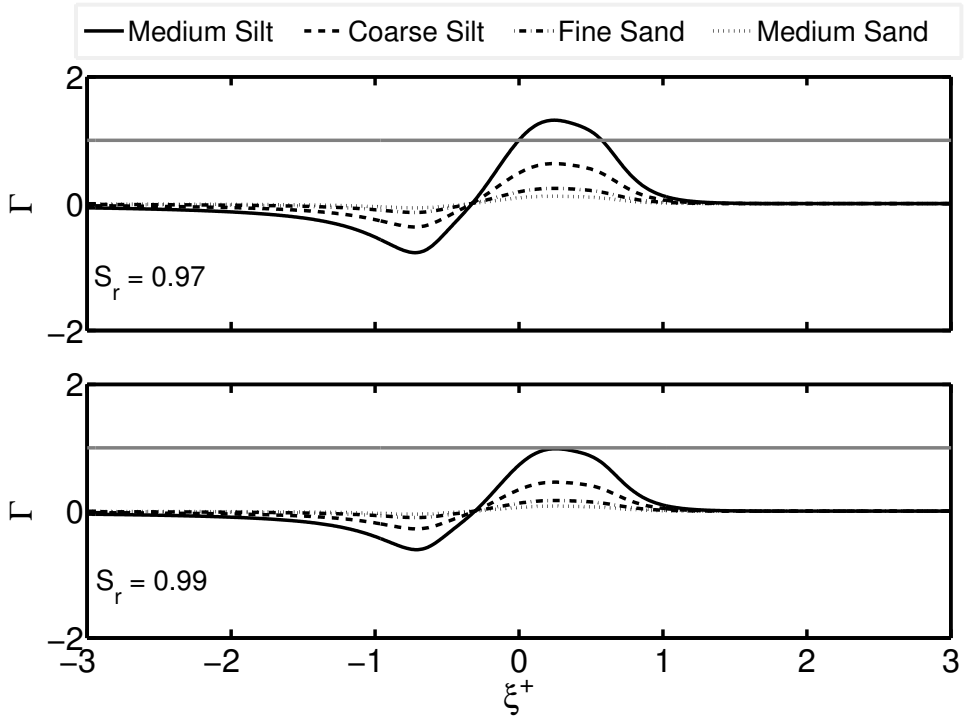

Figure 2.5: Dimensional vertical pore-pressure gradient normalized by the buoyant weight of the bed, and denoted as Γ, defined in Equation (2.11), for the baseline case with a bed saturation of $S_r = 0.97$ (top) and $S_r = 0.99$ (bottom). The decrease in pore-pressure build-up in the less conductive materials (see Table 2.2.2), results in bed failure when the gradient exceeds the buoyant specific weight of the porous medium. The gray line denotes the threshold for failure, as expressed in Equation (2.10).

2.4 Discussion

2.4.1 Penetration depth and thickness of failed layer based on field observations

While there is no experimental or field measurement of the penetration depth for ISW-induced pore-pressure changes, theoretical, experimental and field work, involving surface wave-induced pore-pressure changes, have reported

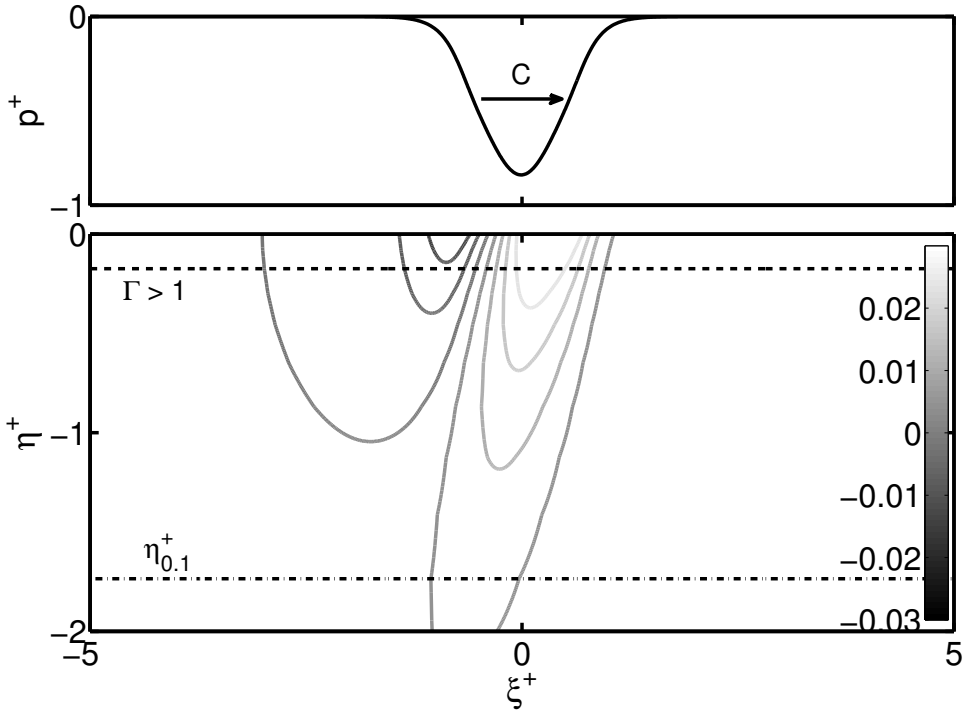

Figure 2.6: Vertical pore-pressure gradient, $-\partial p^+/\partial \eta^+$, for the baseline case, with a bed composed of medium silt and a saturation of S_r=0.97. The ISW-induced pressure, associated with the propagating ISW from left-to-right, is presented at the top, while the contour of the vertical pore-pressure gradient is shown at the bottom. The penetration depth, where the pore-pressure is an order of magnitude above the ISW-induced pressure, is denoted as $\eta^+_{0.1}$, and is shown as the dashed-dot line. The depth inside the bed, where failure criterion denoted in Equation (2.10), is shown as the dashed line.

comparable values. Such studies have predicted depths in excess of 30m [111, 133]. Other surface wave-induced pressure work suggested that the the presence of trapped gas leads to a decrease in the depth of the change in pressure, for depths more than 10m [176]. Wave-induced pore-pressure has been recorded as low as 37m below the seafloor, in 5m-deep water [36]. Such pressure measurements have been associated with surface waves of at least 3m in amplitude [53]. In addition, in waters depths of 13m at the Mississippi Delta, field observations indicate a penetration depth of the change in pore-pressure to be more than 6m into the bed [16]. Thus, in the present study, taking into

account the values of η_o in Table 2.4, penetration depths of similar order are possible.

Field observations of wave-induced bed failure in coastal environments have been associated with liquefaction during storm wave propagation. These waves are characterized by having long wavelength, compared to the depth in which they propagate. For instance, considering soft-sediment deformations of deposits near the Guadalquivir Basin, surface waves, during storm events, are capable of liquefying up to 2m of soil, below the water column [120]. Furthermore, liquefied sediment up to 1.5m thick, has been suspected analyzing sedimentary deformation in the eastern Betic Cordillera, and attributed the bed failure to storm waves with amplitudes greater than 6m in water depths between 10m to 20m [7]. It is noted that, both locations involved deposits that were submerged during the Upper Miocene epoch, and are not an indication of recent wave-induced liquefaction observations in the field. Nevertheless, the present study suggests that if bed failure were to occur during propagation of ISWs, the thickness of the failed layer would be of smaller dimension, than that documented for surface waves.

2.4.2 Comparison with Internal Solitary Waves of elevation in a similar environment

When the pycnocline is located in the bottom half of the water column, ISWs of elevation can form [19, 88, 159, 76, 31]. Assuming properties of the water column similar to the baseline case, with a two-layer continous density ratio with $h_1/h_2 = 7$, an ISW of elevation resembling an inverted ISW of depression can

be obtained from the solution of the DJL Equation. Similar to the total pressure of the baseline case, the hydrostatic and nonhydrostatic component can be obtained from Equation (2.1) and Equation (2.2), respectively.

Due to the dominant hydrostatic pressure, associated with the displacement of the pycnocline, elevation-type ISWs will induce a total positive pressure at the bottom of the water column. Therefore, bed failure, as defined in Equation (2.10) and (2.11) will most likely not occur because although the induced changes produce, effectively, an excess of pore-pressure inside the bed, the now positive vertical pore-pressure gradient at the lee of the wave ($\xi^+ \approx -0.8$ in Figure 2.5 for a depression ISW) is not strong enough to overcome the buoyant weight of the bed. Consequently, other mechanisms of failure need to be explored.

From the analysis of propagating breaking or near-breaking surface waves, it is possible that a steep wavefront could potentially induce a strong horizontal pressure gradient [110], capable of causing bed failure, as long as the gradient is larger than the mobilized internal friction of the grains. In dimensional form, the failure criterion based on the horizontal pore-pressure gradient can be expressed as,

$$\frac{\partial p}{\partial \xi} > \gamma_s tan\phi, \tag{2.12}$$

where ϕ is the internal friction angle of the bed material. Using Equation (2.12), solitary surface waves may be capable of inducing bed failure, but only with a significant portion of trapped gas inside the bed [105]. While ISWs are characterized by a large amplitude, and consequently meet the requirement of a steep

wavefront, in the present study the assumptions on the uniform conductivity and bed dimensions, as presented in Table 2.3, makes less significant the horizontal pore-pressure gradient. Thus, future work will be aimed towards modifying the bed properties and addressing the role of the horizontal pore-pressure gradient induced by ISWs.

2.4.3 Possible failure in deeper environments

The depth considered for the baseline case (H = 50m), in which ISWs propagate, is not unique. Nonlinear, ISW-like, internal waves of depression propagate in water depths in excess of 50m [144] [180] [50]. The results shown so far are limited to a small range of depths in which ISWs have been recorded. Therefore, the sensitivity of our findings to the water column depth must be explored. Using the criterion for bed failure in Equations (2.10) and (2.11), a range of test cases has been examined in deeper waters. The additional depths considered are: 80m, 100m, 200m and 500m. Figure 2.7 shows the dimensional vertical pore-pressure gradient defined in Equation (2.11), for the two-layer, continuously stratified water column with thickness ratio denoted by h_1/h_2, with both saturation values, for each water depth considered. In all of the proposed depths, the maximum available potential energy for the given stratification has been used to generate the strongest ISW. The ISW-induced pressure in increasingly deeper waters is enough to induce failure for weakly conductive materials using the properties in Table 2.2.2, regardless of the bed saturation. Additionally, for this type of bed material, all dimensional vertical pore-pressure gradient result are above unity, regardless of layer thickness ratio, indicating that failure does not depend on the relative depth of the pycnocline.

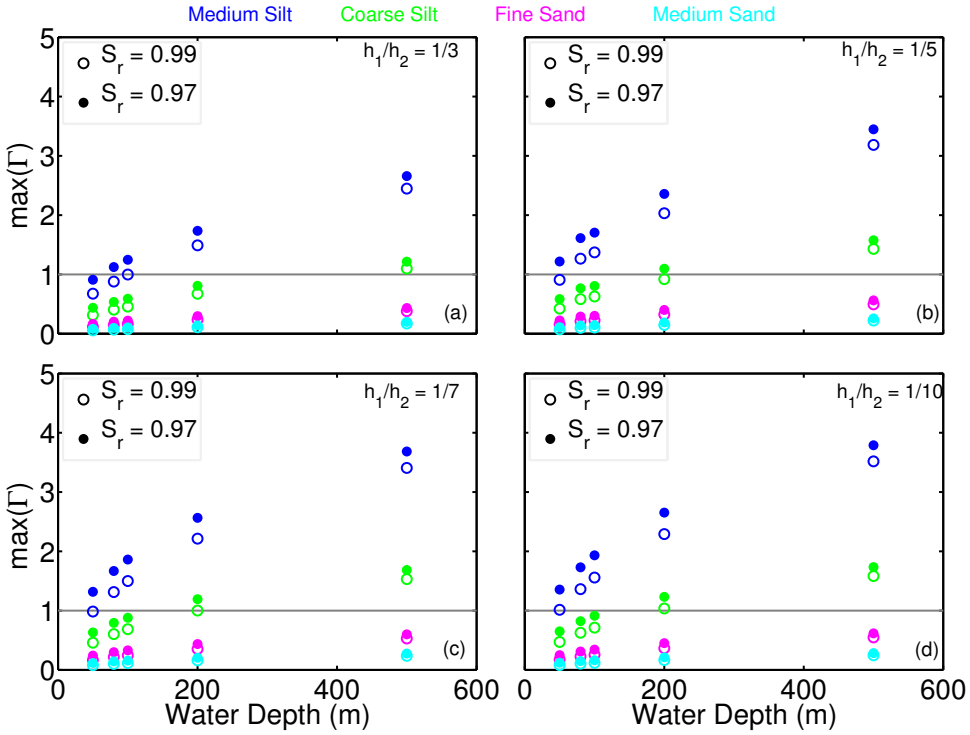

Figure 2.7: Maximum dimensional vertical pore-pressure gradient normalized by the buoyant weight of the bed, as expressed Equation (2.11). The vertical pore-pressure gradient is presented as a function of the water column depth for each type of soil and two-layer continuous density water column with ratio $h_1/h_2 = 1/3$ (a), $1/5$ (b), $1/7$ (c) and $1/10$ (d). The top and bottom figures correspond to saturation values of $S_r = 0.97$ and $S_r = 0.99$, respectively. The grey line denotes the threshold for failure, as expressed in Equation (2.10).

The data presented in Figure 2.7 was obtained from ISWs generated from the DJL Equation ([52]) with a fixed pycnocline thickness $\delta/H = 0.06$, fixed density jump $\Delta\rho/\rho_o = 40/1020$, and a varying two-layer ratio h_1/h_2, for all water depths. Since the maximum available potential energy was supplied in all test cases, ISWs with larger amplitude will be generated when the water column depth is increased. The increasing ISW amplitude, as a function of the water depth, is shown in Figure 2.8 for a two-layer ratio of $h_1/h_2 = 1/3, 1/5, 1/7$ and $1/10$. Due to the dominant hydrostatic pressure component, as presented in Figure 2.2, the amplitude is the primary controlling factor of the absolute maximum ISW

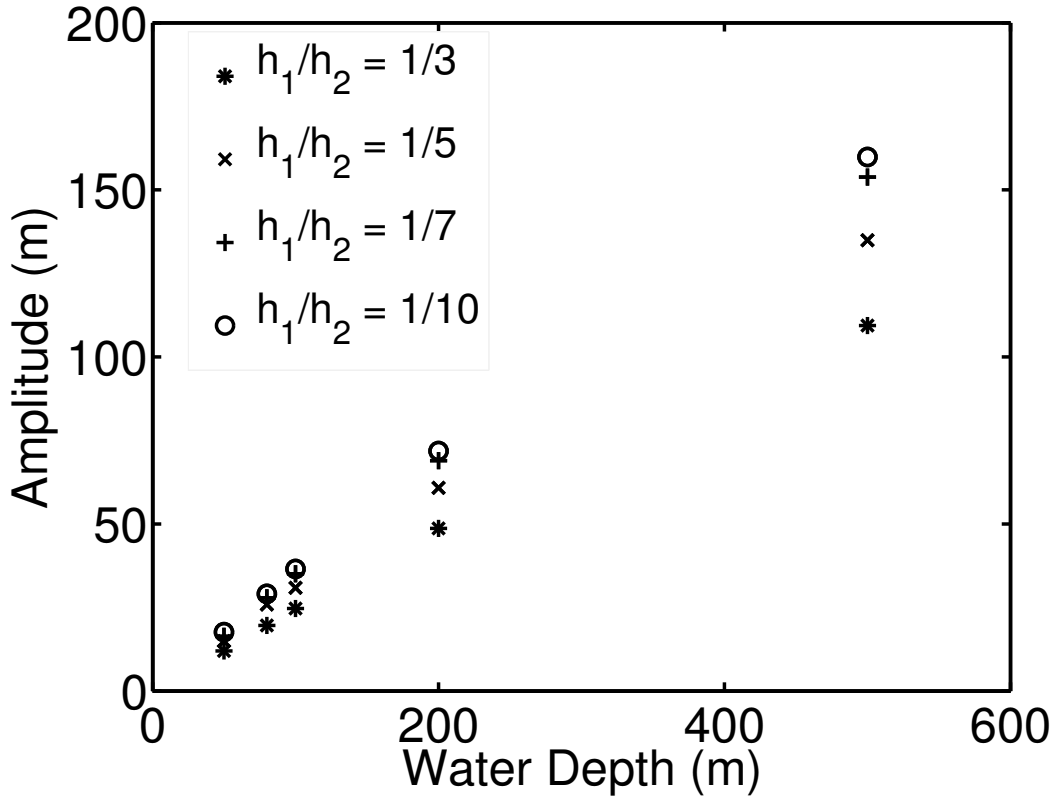

Figure 2.8: Internal solitary wave amplitude as a function of the water depth for a two-layer, continuously stratified water column with ratio h_1/h_2= 1/3, 1/5, 1/7 and 1/10.

wave-induced pressure at the bottom of the water column, because Equation (2.1) describes the dominant pressure component at this location. Thus, the total ISW-induced pressure is expected to become increasingly negative with water depth, producing more favorable conditions for bed failure due to larger pressure values.

In addition to the ISW-induced pressure, bed failure in deeper water depths can also be associated with the bed response. The response is characterized by the diffusive depth, η_o, in the vertical direction inside the bed. A larger diffusive depth implies less accumulation of changes in pore-pressure near the top of the bed, and, consequently, lower likelihood of bed failure. The possibility of bed

failure due to either the larger ISW, or the bed response, can be addressed by examining the ratio $\Delta\rho g A(\gamma_s \eta_o)^{-1}$, originally expressed in Equation (2.11). The results are shown in Figure 2.9, for a two-layer continuous density water column with thickness ratios h_1/h_2 = 1/3 (a), 1/5 (b), 1/7 (c) and 1/10 (d). As the two-layer ratio is decreased from h_1/h_2 = 1/3 (a) to 1/10 (d), $\Delta\rho g A(\gamma_s \eta_o)^{-1}$ exhibits an increasingly nonlinear growth. This growth can be attributed to the increase in the wave speed with water depth [168], as well as the increasing amplitude. Therefore, the possibility of bed failure in deeper environments can be attributed to a combination of both the ISW-induced pressure and the bed response, and is further accentuated by the decrease in the two-layer ratio h_1/h_2.

The present study considers a fixed δ_{pyc}/H and $\Delta\rho/\rho_o$. Clearly the values of both of these parameters can vary in nature. In Table 2.2, it was shown that a smaller value of δ_{pyc}/H will yield lower ISW amplitude. Hence, ISWs propagating in environments with thicker pycnoclines are more likely to cause failure. However, apart from the pycnocline thickness, the density jump, $\Delta\rho/\rho_o$, could play a more significant role in the changes in pore-pressure because, besides the water depth, it is directly linked to the propagation speed of ISWs. The density jump is unique for each environment including oceanic, coastal, and limnological, among others. Values range from $O(10^{-3})$ to $O(10^{-1})$ [88, 125, 159, 129, 142, 161, 8, 21, 102, 103, 186]. Higher $\Delta\rho/\rho_o$ implies faster propagating waves, that will not allow for deeper penetration of changes in pore-water pressure and, increase the build-up of pore pressure near the top of the bed. Caution should be exercised when extrapolating the observations made in this study to deep-water ISWs in the field. In addition to the driving role of the wavelength, the present results highlight the importance of the ISW celerity as controlling factor of penetration depth and, the possibility of bed failure

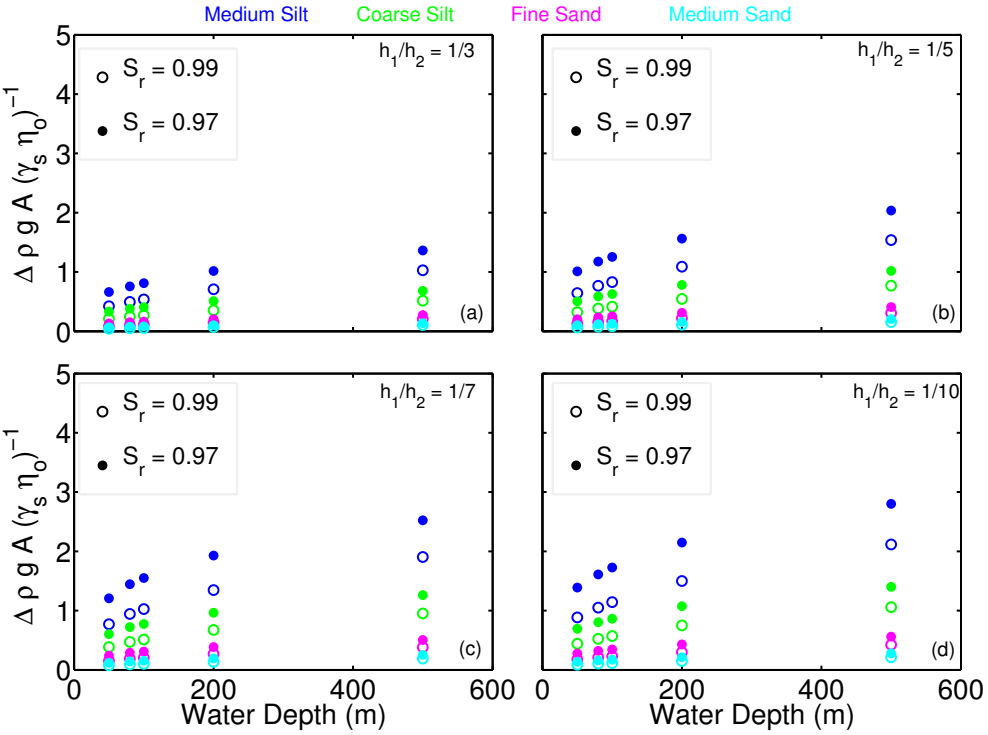

Figure 2.9: Ratio of the ISW-induced pressure, scaled as $\Delta\rho gA$, to the bed pressure scale, $\gamma_s\eta_o$, as a function of the water depth, for a two-layer continuous density water column with ration h_1/h_2 = 1/3 (a), 1/5 (b), 1/7 (c) and 1/10 (d). Internal solitary wave amplitude as a function of the water depth for the two-layer continuous density water column with ratio h_1/h_2= 1/3, 1/5, 1/7 and 1/10. For a fixed pycnocline thickness δ/H and density jump $\Delta\rho/\rho_o$, supplying the maximum available potential energy will yield a larger wave, as required by the method of [52].

[134]. Lastly, it is noted that since ISWs in deeper waters have a larger amplitude, the vertical accelerations, that influence the nonhydrostatic contribution to the pressure, vary with the total depth as well. Thus, difference in the bottom ISW-induced pressure across water depths will not be captured by the current pressure scale.

2.4.4 Role of free-surface induced pressure

The role of the ISW-induced pressure associated with the free-surface displacement [127] has been neglected up to this stage of the study. Nonetheless, its contribution can be quite significant, as it acts to counter the hydrostatic pressure associated with the pycnocline displacement. The observed magnitude of the ISW-induced free surface displacement is reported to be on the order of 10^{-2} to 10^{-3}m [146] and, therefore, its impact is much more pronounced at shallower depths, due to the reduction of the total ISW-induced hydrostatic pressure. The pressure induced by the ISW-driven free-surface, p_{oh}, can be estimated from the horizontal ISW-induced velocity at the surface [127]. This component of the pressure can be expressed as

$$p_{oh} = \rho_o g \eta_o, \tag{2.13}$$

where the surface displacement is obtained by

$$\eta_o = -\frac{1}{g} \int_{-\infty}^{x} \frac{Du_o}{Dt} dx'. \tag{2.14}$$

Here, u_o denotes the horizontal velocity at the top of the water column, at the free-surface. Therefore, the total pressure at the bottom of the water column is now considered as the sum of the hydrostatic pressure, Equation (2.1), the nonhydrostatic pressure, Equation (2.2), and the free-surface induced pressure, Equation (2.13). The dependence on the free-surface induced pressure is considered by computing the vertical pore-pressure gradient and comparing it against the buoyant specific weight, as shown in Figure 2.10 for various water column

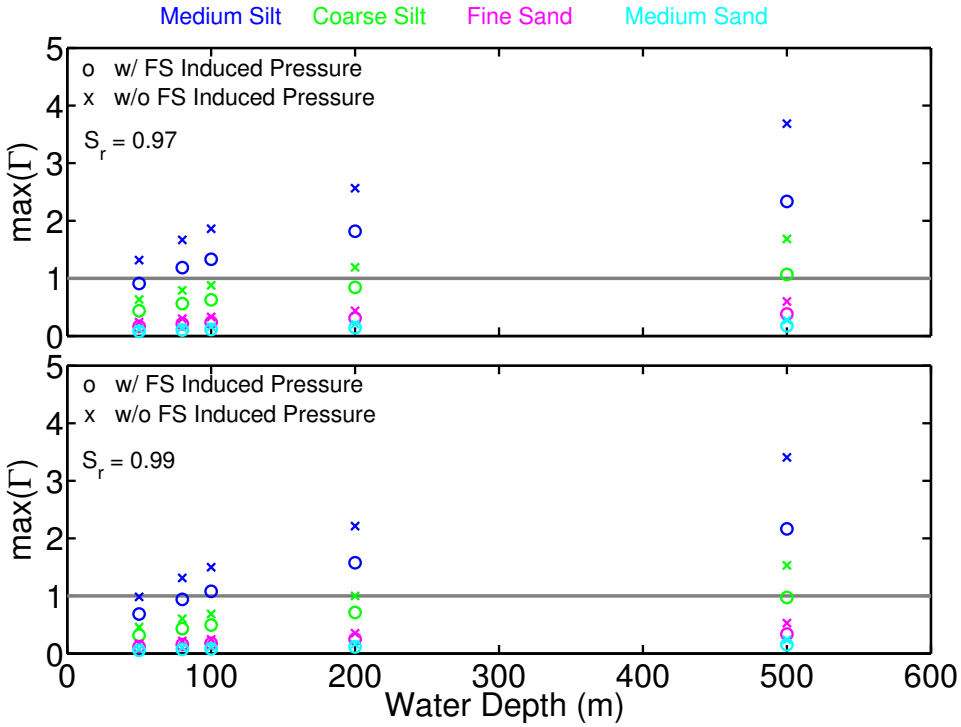

Figure 2.10: Maximum dimensional vertical pore-pressure gradient normalized by the buoyant weight of the bed, as expressed Equation (2.11), as a function of the water column depth, for each type of bed, with and without free-surface induced pressure. The maximum ISW amplitude has been used for a two-layer, continuous density ratio with thickness $h_1/h_2 = 1/7$. The top and bottom figure correspond to saturation values of $S_r = 0.97$ and $S_r = 0.99$, respectively. The gray line denotes the threshold for failure, as expressed in Equation (2.10).

depths. Only the two-layer continuous density thickness ratio $h_1/h_2 = 1/7$ is considered, because it is associated with the strongest ISW-induced pressure, as shown in Table 2.2.

As observed in Figure 2.10, the impact of the ISW-induced free-surface pressure is quite significant. Free-surface pressure acts to increase total bottom pressure. Nevertheless, bed failure in water depths smaller than 100m is still possible only for weakly conductive materials due to the decrease in saturation. However, as the water depth is increased, the possibility of failure also increases and, consequently, at depths $H \geq 100$m, the effects of free-surface induced pres-

sure are not large enough to prevent failure. Hence, the free-surface induced pressure, can be significant enough to prevent bed failure during propagation of an ISW, but only at depths where $H < 100$m.

2.4.5 Possible Impact on Particle Incipient Motion

In the context of particle incipient motion and sediment transport, the vertical pore-pressure gradient can be an additional force to consider, because it acts to reduce the buoyant weight of the particles, in the bed. As such, a modified dimensionless shear stress, or Shields parameter, that considers the vertical pore-pressure gradient can be derived to address the possibility of incipient motion. This modification has been utilized in the study of incipient motion of particles in the bed due to an oscillatory flow [112],. It has been incorporated in the study of surface wave-induced seepage [13] and bed failure due to surface wave runup and rundown [172]. The modified dimensionless shear stress, or Shields parameter, is given as,

$$\theta^{+} = \frac{\tau_b/\rho_o}{g(s-1)d - g\left[-\partial(p/\gamma_l)/\partial\eta\right]d}, \tag{2.15}$$

where τ_b is the shear stress at the top of the bed, s is the density ratio, $s = \rho_s/\rho_o$, d is the particle diameter, and γ_l is the specific weight of the fluid. Equation (2.15) can be regarded as the ratio of the shear force to the modified buoyant force of a particle, where the modification arises from the presence wave-induced vertical pore-pressure gradient. In the present study, the ISW-induced shear stress is not computed, as we consider the inviscid propagation of an ISW where the no-slip condition at the bed is not accounted for. Therefore, it is not possible to directly

compute the ISW-induced shear stress at the top of the bed.

Particle resuspension, during the propagation of an ISW of depression, has been documented in the field [144]. For instances, previous studies proposed that the global instability at the lee of the wave, of the separated wave-induced boundary layer [43, 4], acts as a possible mechanism powerful enough to resuspend sediment. Experimental work has provided additional insight towards the capacity of the instability to drive resuspension [26, 28], as well as, simulations [169]. Furthermore, the ISW-induced resuspension has been parametrized by considering vertical velocity bursts, occurring behind the wave during propagation [3]. This approximation of the ISW-induced shear stress may be expressed as,

$$\tau_{ISW} = \rho_2 c_o^2 \left[0.09 ln\left(Re_{ISW}\right) - 0.44\right]^2, \tag{2.16}$$

where c_o is the linear wave propagation speed in a two-layer continuously stratified water column ($c_o^2 = \Delta\rho g h_1 h_2/(\rho_o H)$) and Re_{ISW} is the momentum thickness Reynolds number based on the wave-induced bottom boundary layer ($Re_{ISW} =\mid U_2 \mid \sqrt{L_W/(\nu(\mid U_2 \mid + c)}$ where ν is the kinematic viscosity and U_2 is the horizontal ISW-induced velocity at the bottom layer). Applying Equation (2.16) to observed nonlinear internal waves [142], suggests that the ISW-induced shear stress with Equation (2.16) to be 8.979 Pa or 8.803×10^{-3} m^{2}s^{-2} [3].

In addition, it is possible to estimate the impact that the ISW-induced vertical pore-pressure gradient can cause on the buoyant weight of a particle, as expressed in Equation (2.15), with the results of the present study. Using the bed properties found in Table 2.2.2, for a medium-sized sand particle, the buoyant

weight, $g(s-1)d$, is computed to be 3.135×10^{-3} m^{2}s^{-2}. From Figure 2.7, for a water depth of 80m, similar to that where NLIWs have been observed [142], with a two-layer ratio of $h_1/h_2 = 1/7$, the contribution of the vertical pore-pressure gradient, $g\left[-\partial(p/\gamma_l)/\partial\eta\right]d$, is 3.154×10^{-4} m^{2}s^{-2} for a saturation of $S_r = 0.97$ and 2.233×10^{-4} m^{2}s^{-2} for a saturation of $S_r = 0.99$. This contribution represents a reduction in the buoyant particle weight of 11% for a saturation of $S_r = 0.97$ and 8% for a saturation of $S_r = 0.99$, and could be significant enough in the presence of a shear-inducing mechanism. Thus, for powerful resuspension events, such as the nepheloid layer [144] or the formation of sand waves due to ISW passage [50], the ISW-induced pressure could drive a substantial contribution, and in the presence of shear stress, facilitate resuspension.

CHAPTER 3

FORMATION OF RECIRCULATING CORES IN INTERNAL SOLITARY WAVES OF DEPRESSION SHOALING OVER GENTLE SLOPES

3.1 Introduction

As mentioned in Chapter 1, Nonlinear Internal Waves (NLIWs) have long been associated with the transport of energy, mass, and momentum in stratified flows. These long nonlinear and nonhydrostatic waves adjust their waveform while propagating over varying bathymetry. This adjustment process is known as shoaling; through the turbulence it enhances inside the NLIW, it is a major mechanism by which mixing in the interior of the water column is intensified [125, 161], nutrients are transported across long distances [121], and particulates are resuspended from the bottom bed [144]. Shoaling NLIWs may profoundly change the properties of the water column, with broader implications for marine habitats and deep-sea exploration.

The largest observed NLIWs have been found in the South China Sea (SCS) [77, 192, 143, 104]. These waves are generated by the interaction between the internal tide and the bathymetry in the eastern Luzon Ridge [9]. Once formed, NLIWs propagate for hundreds of kilometers and arrive at the western continental shelf. Worthy of note is the region regarded as the Dongsha Plateau, or Dongsha Slope, located near Lat. 21^o N, Lon. 117.5^o E. Here, NLIWs have been observed to not break, but rather adjust to the decreasing water column depth and retain their symmetric shape until they reach the shallower continental shelf.

A shoaling NLIW may lose energy via dissipation or scattering onto higher wavenumbers upon encountering variations in the water column depth. In the absence of significant energy dissipation, the wave may be regarded as shoaling adiabatically. Adiabatic shoaling has been addressed in the context of Internal Solitary Waves (ISWs) of depression over idealized and gently varying bathymetry (i.e. $S < 3\%$) [48, 62, 184]. An ISW is a large amplitude, single depression (mode-1) of the pycnocline, where nonlinearity is in balance with dispersion; it is commonly used as a characteristic representation of a NLIW. Simulations of a ISW shoaling over a bathymetry similar to that of the Dongsha Slope suggests that the waves undergo adiabatic shoaling, where their symmetric shape is preserved as they arrive into the shallower continental shelf [99]. Hence, adiabatically shoaling ISWs, such as those found near the Dongsha Slope, do not lose significant energy as a result of propagating over slowly varying bathymetry.

When an ISW shoals over steeper slopes (i.e. $S \geq 3\%$), the wave propagation speed, c, decreases below the maximum wave-induced horizontal velocity, U_{max}, inducing a steepening of the rear of the wave, overturn, and disintegration [83, 183, 5]. However, over gentle slopes the propagation speed may drop below U_{max}, but the ISW will not disintegrate. Instead, it steepens at the rear with heavier fluid plunging forward, becoming entrained above the location of the maximum isopycnal displacement, or trough. The ISW is said to be convectively, or kinematically, unstable [148, 135, 71] because the infringed fluid is heavier than the surrounding and locked with the wave. This trapped region is convectively unstable, with $U_{max} > c$, and may be described as a vortex core, or a region with closed streamlines [39, 6].

A closed streamline core is by definition recirculating and has been observed in ISWs in the field [128, 141, 102, 103, 191], experiments [37, 64, 28, 107], and simulations [94, 95, 57, 100, 72, 165, 87, 30, 108, 99, 109]. The core's convectively unstable nature enhances turbulent mixing and energy dissipation in the water column. Concurrently, ISWs with recirculating cores may also transport mass across large distances (i.e. $O(km)$). The process by which heavy fluid enters the core may be regarded as "breaking", but it is not abrupt enough to cause a complete wave disintegration. As such, ISWs with recirculating cores have undergone convective breaking, and remain convectively unstable due to overturning induced by the recirculating motion itself, as they propagate over the gently varying bathymetry.

The mechanism by which a convective instability and a recirculating core forms during shoaling was first addressed, through experimental and theoretical studies of a wave-driven disturbance propagating in a two-layer density stratification, over an idealized slope-shelf bathymetry [71]. Under such conditions, the amplitude of the incident ISW can be related to the lower layer thickness at the shelf, and to check that convective overturning, characterized by a larger on-shelf velocity than the wave propagation speed, occurs; a convectively unstable shoaling wave has an amplitude that is approximately 40% of the lower layer thickness. Experiments of an ISW shoaling over a continuous slope also have concluded that the wave becomes convectively unstable when the wave amplitude reaches 40% of the bottom layer water depth [69]. Simulations of a shoaling ISW over a slope-shelf bathymetry have also concluded that an ISW breaks over a slope-shelf bathymetry because the amplitude exceeds the 40 % of the bottom layer water depth, but if this condition is not met, the ISW propagates onto the shallow shelf zone [183]. These studies recognized that, the

ISW-induced horizontal velocity exceeds the wave propagation speed immediately before the the wave breaks and that when breaking occurs, waves may transport mass upslope. As such, examining the wave amplitude for a given bed slope, may can indicate the presence of a a convective instability and a recirculating core.

Given a bottom bed slope, it may be possible to extract the wave amplitude required for convective overturn and the formation of a recirculating core [183]. Nevertheless, the fluid properties in the water column may be just as significant as the properties of the bathymetry [94]. Numerical studies have considered the role of the background density and current over idealized slope-shelf bathymetry and established that recirculating cores are possible if there is baroclinially-generated near-surface vorticity present, through the background density field. These have also highlighted the importance of the baroclinic background current during wave propagation [168, 95, 165] . For instance, in the absence of near-surface stratification, trapped cores may be possible so long as there is near-surface shear [165]. Therefore, comparing the ISW amplitude to the bottom layer thickness, for a given bed slope, may be an indicator of convective breaking and recirculating core formation, but so does the preexisting vorticity at the top of the water column. In addition, without near-surface vorticity the ISW will be conjugate flow-limited, where the wave broadens and the trough becomes flat as it shoals over the slope, or shear-instability limited, because the value of the local Richardson Number decreases with increasing wave amplitude [94, 95].

To this date, the theory, laboratory, and simulations of recirculating cores in ISWs have only focused on a category regarded as surface-type, which may

be different than that observed in the field. Surface cores reside at the top of the water column, above the trough. The field observations have also noted that that ISWs of depression can support subsurface cores, located closer to the wave trough [102]. What determines the depth of the core is the sign of the near-surface vorticity associated with the preexisting baroclinic background current, not the density field [67]. A recirculating subsurface core forms as the ISW shoals, because the near-surface vorticity layer in the water column is stretched by the propagating wave, with U_{max} increasing past the wave propagation speed [97]. The comparison between the maximum ISW-induced velocity and propagation speed represents the second criterion to account for the presence of subsurface recirculating cores. Although, if the wave amplitude is compared to the thickness of the bottom layer in the water column, the ISW with subsurface recirculating cores observed are very close to the limit of 0.4 [103]. The amplitude and velocity scale criteria are still applicable to establish the presence of a recirculating core, but the predominant mechanism that leads to core formation remains to be identified.

Within the convectively unstable region, surface recirculating cores are known to contain a single rotating vortex [94, 95, 72]. Subsurface recirculating cores have been observed to have two counterotating vortices [102]. These vortices contribute to the mixing of the fluid inside the core and the dissipation of the turbulent kinetic energy of the wave. It has been argued that the dissipation may be approximately four orders of magnitude higher than that of the open-ocean [102]. In addition, the fluid inside the convectively unstable region is observed to be transported with the ISW. In this context, the associated instantaneous mass transport may be approximately 18Sv. Thus, subsurface recirculating cores provide a mechanism by which mass is transported, fluid is

mixed, and energy is dissipated in the water column.

The field observations of subsurface recirculating cores are based on single-point measurements [102, 103]. Questions still persist regarding the process by which shoaling ISWs reach the convective breaking regime and the ensuing subsurface core formation occurs within the wave. Given the computational resources available nowadays, it is possible to complement the field observations in the Dongsha Slope with high-accuracy/resolution and fully nonlinear/nonhydrostatic simulations. To this date, no study has attempted to simulate subsurface recirculating core formation with observed field conditions. Since, the aforementioned studies also measured the bathymetry, the shoaling process can be simulated with both the observed properties of the water column and the observed water depth. The formation of the convective instability, and subsequent recirculating core, can then be applied to the simulated fields, thereby bridging the gap between localized observations and the full evolution of the shoaling process.

As the foundation of the numerical tool used in this Chapter, the spectral multidomain penalty method (SMPM) [58, 59, 41, 73] , has been successfully applied to the study of small scale stratified flow processes [44, 2, 194, 195], without minimal artificial dispersion and diffusion, including the propagation of Internal Solitary Waves in a uniform depth wave-guide and their 2D study of their interaction with a model no-slip sea floor [43]. Recently, the method was also adapted to include deformed boundaries, while preserving its high-order accuracy, thereby allowing the incorporation of gentle bathymetry over long domains [80]. Thus, the SMPM flow solver can be used to study shoaling ISWs over gentle slopes and long distances, along with the formation of subsurface

cores, based on high-accuracy/resolution simulations that can incorporate the recorded field conditions.

The present study aims to complement the single-point field measurements of the subsurface core performed by collaborator Dr. Ren-Chieh Lien and his team [103]; their study is hereby referred to *RCL14*. The observations were based on two moorings, deployed along a localized region in the Dongsha slope, and ship surveys that tracked the waves, as these approached the moorings. First, the formation of a subsurface core from a shoaling ISW with an initial amplitude comparable to the measured value is explored. Second, the sensitivity of the obtained subsurface core to the initial conditions is addressed by selecting a larger initial wave, modifying the near-surface background current profile, and modifying the SCS bottom slope. The measured background density and current profile, prior to the wave arrival, along with the SCS bathymetry, provide the reference baseline for the simulation performed. The two questions guiding this study are: a) what are favorable conditions for the formation of recirculating subsurface cores in ISWs shoaling over gentle slopes? and b) how do variations in the properties of the water column and bathymetry impact subsurface core formation? Numerical simulations in two dimensions address the shoaling problem over a reduced section of the transect spanned by *RCL14*. Results are compared with field observations to try and match ISW properties and the size of the convectively unstable region. In addition, the amplitude of the ISW is compared to the thickness of the lower layer of the water column, to examine the applicability of the amplitude-shelf criterion [71]. The dissipation of kinetic energy and mass transport are not computed, as these will be the focus of a separate study, within the identified parameter space of the present work. The present study aims to establish the foundation for future 3D simulations of

a shoaling ISW with a subsurface recirculating core.

This Chapter is structured as follows: Section 3.2 discusses the methodology which includes the background field conditions, the governing equations of ISWs with recirculating subsurface cores, problem geometry, and simulation description. Section 3.3 presents the results, detailing the wave properties for a given initial ISW. The effect of the maximum value of the Dongsha Slope is also addressed, as this corresponds to the only region within the SCS where the subsurface cores can be observed. Section 3.4 explores the variations in the initial conditions and how these may impact the results in Section 3.3. Particular emphasis is placed on the initial ISW amplitude and the magnitude of the near-surface shear, associated with the baroclinic background current. Conclusion and suggested future work are included in Chapter 5.

3.2 Methodology

3.2.1 Field Conditions

Figure 3.1 shows the bathymetry of the region of interest in the SCS, along with the bathymetry presented in *RCL14*, in which NLIWs were tracked. Figure 3.1(a) contains the General Bathymetric Chart of the Oceans (GEBCO) 30 arc-second interval grid data. Within the SCS, *RCL14* tracked NLIWs from Lat. 21^o N, Lon. 119^o E to Lat. 21^o N, Lon. 116.5^o E. These coordinates lie along the normal-to-isobath track along which NLIWs are found to propagate. The observed water depth, along this track, is denoted as the solid-black line in Figure 3.1(a) and 3.1(b). Note that the GEBCO data is used only to visualize the South

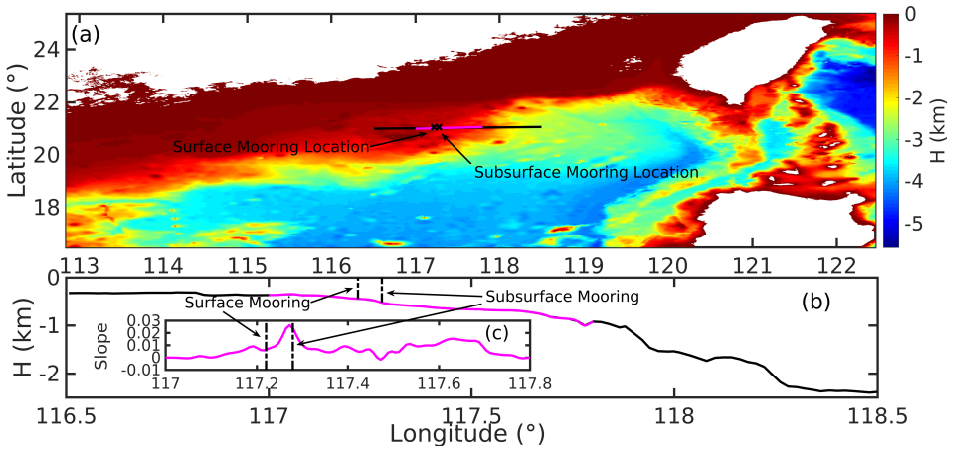

Figure 3.1: (a) Bathymetry of the South China Sea, as found in the General Bathymetric Chart of the Oceans (GEBCO). The landmasses are shown in white. *RCL14* tracked NLIWs from Lat. 21^o N Lon. 119^o E to Lat. 21^o N, Lon. 116.5^o E. This path is denoted as the black solid line in (a). The measured bathymetry is shown in (b). A reduced one-dimensional bathymetric transect of approximately 80km is extracted, over the distance covered by *RCL14*, to simulate ISW propagation in this study (magenta overlaid on black in (a) and (b)). The corresponding bottom slope for the shortened path is shown in (c). *RCL14* deployed subsurface and surface moorings at Lat. 21.07^o N, Lon. 117.27^o E and Lat. 21.07^o N, Lon. 117.22^o E, respectively. These moorings are denoted by the black-cross markers in (a) and as the black-dashed lines in (b) and (c).

China Sea, not to extract any detailed water depth information.

The particular choice of bathymetry profile is crucial in dictating the physics of the shoaling problem. Thus, the characteristic bathymetry necessary for subsurface core formation is taken to from the measured data in Figure 3.1(b). The GEBCO database corresponds to an approximated water depth from an algorithm based on Generic Mapping Tools [1], which may not capture the water depth along the coordinates of interest as accurately as the observational measurements have.

RCL14 deployed subsurface and surface moorings at Lat. 21.07^o N, Lon. 117.27^o E and Lat. 21.07^o N, Lon. 117.22^o E, respectively; these are approxi-

[1] see https://www.bodc.ac.uk/data/documents/nodb/301801/

mately 6km apart and cover the region of the steepest slope. Here, the profiles of temperature, density, and velocity were measured prior, during, and after ISW propagation. The location of the moorings is denoted as the black-cross marker in Figure 3.1(a) and as the black-dashed lines in Figure 3.1(b) and 3.1(b).

Since the NLIWs shoaled over a 2^o West-oriented direction, from a modeling perspective such a long distance can be challenging given the broad range of scales that must be resolved to accurately capture the wave propagating with a subsurface recirculating core. Thus, in this study, a smaller region of interest is extracted, where the shoaling process can be thoroughly analyzed, thereby mitigating the computational overhead. Given that the location where the field observations were made is approximately 1.3^o W from the start of the covered track, the shorter region of interest is focused between Lat. 21^o N, Lon. 117.5^o E to Lat. 21^o N, Lon. 117.0^o E. These new coordinates are shown as the magenta curve in Figure 3.1(a) and 3.1(b). Lastly, the bottom slope corresponding to the gently varying bathymery, for the shorter region of interest, is shown in Figure 3.1(c) as the magenta line. The maximum slope value is 2.8%, or 1.6039^o, and is very close the location of the subsurface mooring. The actual slope values at the subsurface and surface moorings are 1.3710^o and 0.3649^o, respectively.

The governing equations discretized to simulate the shoaling process are formulated in a Cartesian coordinate system. To incorporate the observed bathymetry into the model, the SCS coordinates need to be converted from Lat./Lon. to Universal Transverse Mercator (UTM). Since there is negligible latitudinal change for a given longitudinal displacement, as one moves along the observational path, the small deviations in the northing direction can be neglected. Thus, in a Cartesian framework, x is taken to represent the easting and

z is the depthwise direction. The beginning of the SCS bathymetric transect can be used as a reference point to create a transect, initiating at Zone 50 N 0551964 mE 232222 mN. Finally, when changed to UTM, the NLIWs were tracked by *RCL14* along a distance of approximately 260 km; the SCS bathymetric transect used in this study is approximately 80 km-long, with the water depth varying from 921m at the deepest to roughly 360m at the shallowest location.

3.2.2 Properties of the Water Column Prior to the arrival of the NLIW

The subsurface mooring, located at a water depth of approximately 525m, had one ADCP, 10 temperature sensors and three CTD sensors. The surface mooring was deployed at a water depth of approximately 450m and contained two Acoustic Current Doppler Profilers (ADCP), 14 CTD sensors, and three temperature loggers. The spacing between CTD's varied between 10 and 30m, depending on the location in the water column. For a more detailed description of the equipment, the reader is referred to Section 2 of *RCL14*. The moorings measured for four different days ranging from May 31, 2011 to June 3, 2011. In the present work, emphasis is placed on the data corresponding to June 2, because on this day the authors observed the first subsurface recirculating core.

Figure 3.2 shows the recorded time-averaged background profiles, prior to wave arrival, at the subsurface mooring. These fields are used as the background conditions to simulate wave propagation. Figure 3.2(a), Figure 3.2(b), Figure 3.2(c), and Figure 3.2(d) correspond to the background velocity, shear, density, and Brunt-Väisälä (BV) Frequency, respectively. A negative background

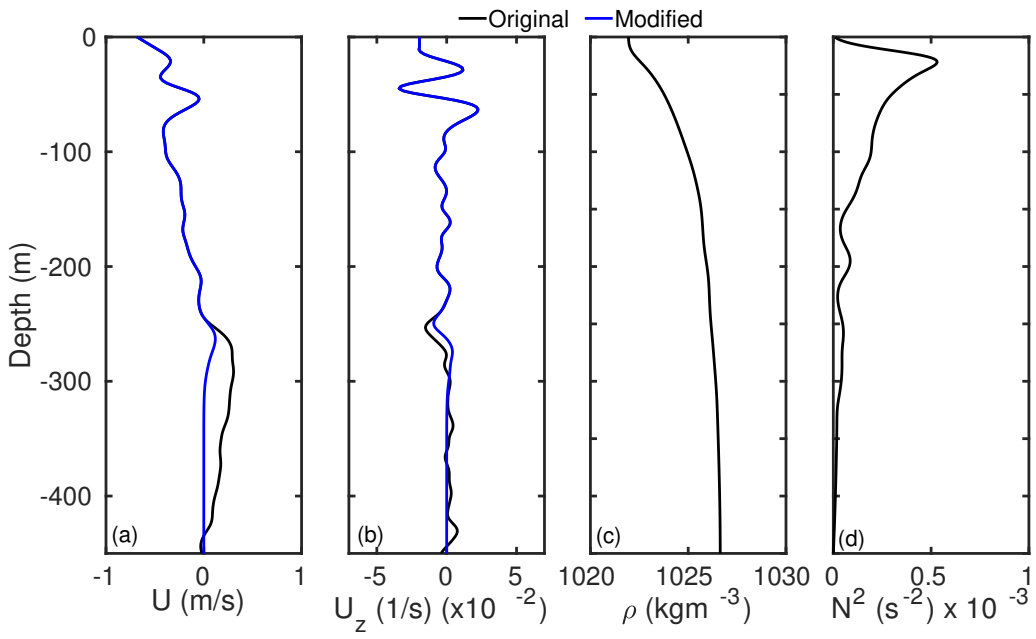

Figure 3.2: Time-averaged vertical profiles of the background current (a), shear (b), potential density (c), and Brunt-Väisälä Frequency (d). The measured profile values were obtained from the surface and subfurface moorings deployed at Lat. 21.07^o N, Lon. 117.22^o E and Lat. 21.07^o N, Lon. 117.27^o E, respectively, by *RCL14*. For (a) and (b), the lower 200m values have been filtered to zero, as shown by the blues lines, to avoid any unwanted hydraulic interaction of the backgorund current with the gently varying bathymetry.

velocity denotes eastward flow (i.e. away from the shore). ISWs propagated in the positive westward direction (i.e. towards shore). Note that this convention is opposite to that typically adopted in the field, and is only applied in the present study. The BV Frequency is defined as $N^2 = -g\rho_o^{-1}d\rho/dz$, where g is the gravitational acceleration and ρ_o is the reference density. The location of the pycnocline, defined as the depth at which the maximum BV Frequency occurs, was observed to be at a depth of $z_o = -22$m. At this depth, the density value was 1022.57 kgm^{-3}; the reference density is then set to $\rho_o = 1022.57$ kgm^{-3} for the present study.

In addition, Figure 3.2(a) and Figure 3.2(b) also show the original (black) and

modified (blue) background current profile, U, and vertical shear, U_z. To avoid hydraulic effects, that may be associated with interactions of the background current with the gently changing bathymetry, values below 300m are smoothed to zero when used in the simulation. Furthermore, note that in Figure 3.2 (b), the near-surface region has negative vorticity; subsurface recirculating cores can be expected on this day, regardless of the near-surface baroclinic vorticity.

Finally, because the water column properties were reported at a single location, any spatial variability in the along-shore direction is ignored. Thus, the background fields used in the model do not vary in the propagating direction, and are taken to be representative of the background conditions. This approach assumes that the time scale of the temporal changes in the background field is larger than that the characteristic propagation time of ISWs, which may be reasonable given that the time scale of the semi-diurnal internal tide may be one order of magnitude higher than that of the ISWs in the South China Sea [51].

3.2.3 Governing Equations

The governing equations for the present modeling study are the incompressible Navier-Stokes Equations under the Boussinesq Approximation (INSB) in two-dimensions [92]. Prior to initializing the flow solver, the velocity field in the horizontal direction is decomposed into a perturbation, $u'(x,z,t)$, and a steady background field, $U(z)$; $w'(x,z,t)$ is used to describe the full vertical velocity. Per the Boussinesq approximation, the density field is decomposed into a reference, ρ_o, a background, $\overline{\rho}(z)$, and a perturbation field, $\rho'(x,z,t)$.

In vector form, for a fixed reference frame without rotation, the mass conser-

vation is

$$\nabla \cdot \mathbf{u} = 0. \tag{3.1}$$

The momentum equation in the along-wave, x direction, is

$$\frac{\partial u'}{\partial t} + u'\frac{\partial u'}{\partial x} + w'\frac{\partial u'}{\partial z} + U\frac{\partial u'}{\partial x} = -\frac{1}{\rho_o}\frac{\partial p'}{\partial x} - w'\frac{\partial U}{\partial z} + \nu\nabla^2 u', \tag{3.2}$$

and

$$\frac{\partial w'}{\partial t} + u'\frac{\partial w'}{\partial x} + w'\frac{\partial w'}{\partial z} = -\frac{1}{\rho_o}\frac{\partial p'}{\partial z} - U\frac{\partial w'}{\partial x} + \nu\nabla^2 w' - \frac{\rho'\mathbf{g}}{\rho_o}, \tag{3.3}$$

in the vertical z direction, where $p'(x,z,t)$ is the perturbation pressure with respect to the reference background state, t is time, ν is the kinematic viscosity, and $\mathbf{g}$ is the gravitational acceleration (depthwise) direction. Rotation is neglected. Note that, during shoaling, the effects of changing water depth dominate over rotational forces [99]. Over constant water depth, rotation results in radiation of long inertia-gravity waves, which gradually decrease the ISW in amplitude [68, 99].

The density equation is

$$\frac{\partial \rho'}{\partial t} + \nabla \cdot [\mathbf{u}\,(\rho' + \overline{\rho}(z))] = \kappa\nabla^2\rho', \tag{3.4}$$

where $\mathbf{u} = (u' + U, w')$ and κ is the mass diffusivity. In Equation (3.2) and (3.4), the diffusion of the background profile is neglected. Lastly, following the Boussi-

nesq Approximation, the reference pressure, $\overline{p}(x,z)$, is in hydrostatic balance with the background field in the absence of any wave propagation:

$$\frac{\partial \overline{p}}{\partial z} = -\left(\rho_o + \overline{\rho}\right) g. \tag{3.5}$$

3.2.4 Numerical Method

Generating the Initial Conditions from Fully Nonlinear Internal Wave Theory

The isopycnal displacement, η, driven by the fully nonlinear Internal Solitary Wave (ISW) and used to initialize the numerical model, is obtained by solving the Dubreil-Jacotin-Long (DJL) Equation. It is a nonlinear eigenvalue problem derived from the steady incompressible Euler Equations under the Boussinesq Approximation, in a reference frame, ξ-ζ, moving with the wave [106, 179]. To solve the DJL Equation, the pseudospectral numerical method developed by [52] is employed. Obtaining a solution requires prescribing the background density and current field, along with a target value for the Available Potential Energy (APE). The APE is defined as the minimum energy required to adiabatically bring a parcel of fluid from its displaced location back to its reference location.

Once the solution of the DJL Equation is obtained, the density field is computed by considering the difference between the reference and perturbed state (i.e. $\rho(x, \zeta\text{-}\eta)$). The wave velocity fields are computed via spectral differentiation of the isopycnal displacement field. Therefore, the DJL Equation provides the

density, horizontal, and vertical velocity which are the initial conditions of the unsteady SCS shoaling simulation. More information on the DJL Equation and how to obtain the ISW velocity and density field from its solution may be found in the Appendix.

Simulating the shoaling of the ISW

Equations (3.1) through Equation (3.4) are solved numerically using a deformed-subdomain variant, in two-dimensions, of the spectral multidomain penalty method (SMPM) [80]; it is collocation-based in the x and z direction. A local Legendre-polynomial expansion is used to approximate the solution at each node of a Gauss-Lobatto-Legendre grid in each element [91]. Time-integration is achieved via a Stiffly-Stable Third order scheme [84].

The boundary conditions, used to solve Equation (3.2), (3.3), and (3.4) of the SCS shoaling problem, are specified as free-slip/no-flux at all four impermeable physical boundaries. In addition, at the left and right boundaries, an artificial Rayleigh-type damper, one ISW half-width thick, is applied to eliminate any possible reflection from the incoming ISW [1]. For Equation (3.4), no-flux boundary conditions are implemented in all four physical boundaries, along with the Rayleigh-type damper at the left and right boundary. Lastly, an exponential spectral filtering technique is applied to dissipate any numerical instabilities.

3.2.5 Simulation Description

Obtaining the Fully Nonlinear ISW Field

The background fields presented in Section 3.2.2 are used to solve the DJL Equation (i.e. Equation (A.1) to Equation (A.6)) at the initial water depth of H_i = 921m; this is the value at the deepest point of the compacted SCS bathymetric transect used in this study (see Figure 3.1(c)). Since the background density was measured up to a depth of 450m, any value below this depth is assumed to be constant. Only the near surface value of the background density is directly linked to the formation of recirculating cores [94]. As such, the effects of the near-bottom stratification in the water column are not examined in the present study.

The DJL solver's computational domain is $20H_i$-long. Such an aspect ratio is required to avoid any interaction between the solution and its periodic image. The DJL-generated initial condition inserted into the SCS shoaling simulation has an APE value of 205MJ, because the corresponding ISW amplitude is close to that observed by *RCL2014* at a water depth of 525m. Note that this solution may not be representative of the observed wave at a deeper location along the SCS transect. Unfortunately, the lack of upstream field measurements on the wave amplitude and energy impact the accurate representation of the initial wave. Thus, an initial condition resembling the observed wave at a location in shallower waters allows for the exploration parameter space of the shoaling problem, which is the focus of this paper.

The density, horizontal, and vertical velocity is projected onto the GLL grid via cubic spline interpolation. Since the solution of the DJL Equation yields a

rightward propagating wave, in the positive ξ-direction, the SMPM coordinate system is set so that the positive x-direction points to the shore (i.e. westward in Figure 3.1); the positive z-direction is directed upward, with the reference datum placed at the free-surface. Note that while the DJL ξ-ζ domain moves with ISW, the SMPM x-z domain is fixed in space, so no Galilean transformation is required to capture the wave propagation. The DJL ISW has an initial amplitude of A_i = 143m, a half-width of $L_{w,i}$ = 1,014m, and a propagation speed of c_i = 1.9258ms^{-1}.

Construction of the Computational Domain

Figure 3.3 shows the computational domain used in the shoaling simulation. The contour variable is the time-averaged background density observed by *RCL2014* on June 2, prior to the wave arrival at the subsurface mooring (i.e. Lat. 21.07^o N, Lon. 117.22^o E or 50 N 54200mN 2329860mE). The computational domain begins at -20km and not 0km, which is the start of the SCS transect. The region ranging from -20km to 0km, and demarcated by the solid red box, is an artificial plateau (i.e. constant water depth) with a length equal to that of the DJL domain; the SCS transect initiates at a range of 0km. The plateau is included to allow the ISW to propagate without shoaling for approximately $10L_{w,i}$. This approach eliminates any non-physical changes to the waveform that would otherwise occur by placing the propagating ISW over actual bathymetry, from the first timestep. Aside from the artificial plateau, four distinct locations are also noted in Figure 3.3: the initial position of the trough (Location I, white-dashed line), the surface and subsurface moorings (black-dashed lines), and the shallowest portion of the transect (Location II, yellow-dashed line). These four

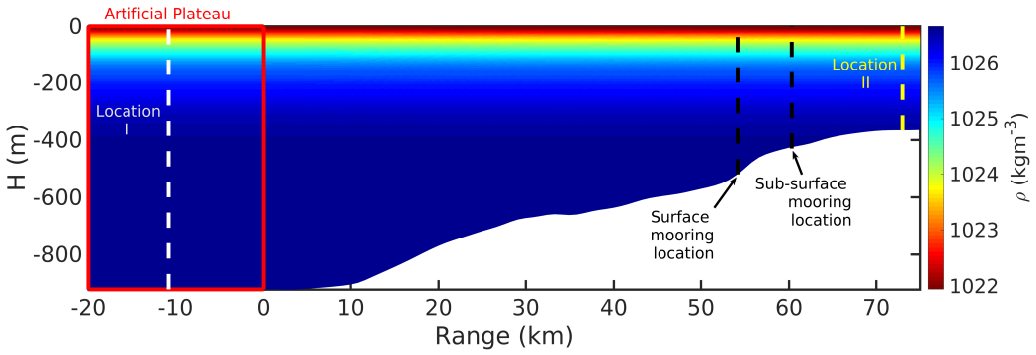

Figure 3.3: SCS bathymetric transect with the time-averaged background density, $\overline{\rho}(z)$, from June 2 (Figure 3.2 (c)), as the contour variable, obtained from *RCL2014*. The transect ranges from Lat. 21^o N, Lon. 117.5^o E to Lat. 21^o N, Lon. 117.0^o E. Location I (white-dashed line) corresponds to trough of the ISW (solid-red line) at the initial position. The artificial plateau, denoted by the red box, corresponds to the location from where the initial ISW is launched; it is 20km in length with a water depth of 921m. Field observations occurred at Lat. 21.07^o N, Lon. 117.22^o E (surface mooring) and Lat. 21.07^o N, Lon. 117.27^o E (subsurface mooring) and these locations are denoted as the black-dashed lines along the transect. Location II corresponds to the shallowest region in the transect, where the water depth is approximately 360m.

locations will be used as reference in the subsequent analysis.

To numerically solve Equation (3.1) through Equation (3.4) with the SMPM, the computational domain is partitioned into m_x subdomains in the streamwise (x) and m_z subdomains in the vertical (z) direction, with n points per subdomain in each direction. The polynomial degree used to approximate the solution within each element is $p = n - 1$. Together, the total number of degrees of freedom is defined as: $\mathrm{n}^2\mathrm{m}_x\mathrm{m}_z$.

The corresponding resolution used in the shoaling simulation analyzed here is determined via a refinement study for the number of subdomains in the horizontal, where a test ISW is allowed to propagate until the subsurface mooring location and then visually examined for changes in the structure of the solution, as a function of the grid spacing. The test simulation is performed with a

fixed n value of 15 and initial m_x = 400 subdomains in the horizontal and m_z = 25 subdomains in vertical direction. The number of points per subdomain is the suggested minimum required to resolve any possible length scale, with a spectral method [22]. Subsequent test simulations are performed up to m_x = 1600. Figure 3.4 shows visualization of the wave for five different cases: m_x = 400, 600, 800, 1200, and 1600. The simulations are stopped at the region of interest, between the subsurface and surface mooring where the water depth is 450m. The number of vertical subdomains is fixed with m_z = 25. No significant different exists in the structure of the solution after m_x = 800; this is the value chosen as the number of subdomains across the horizontal domain, in the streamwise direction, for the SCS shoaling simulation. In addition, a subdomain convergence study in the vertical direction was also performed (not shown) with m_z = 20, m_z = 25, and m_z = 30; no visual difference in the structure of the solution was recorded.

Worthy of note is the choice of m_z, which has a significant impact in the computational overhead associated with solving the governing equations, using the SMPM flow solver. The numerical method utilizes a Schur factorization of the Poisson operator, to solve the Pressure Poisson Equation[81, 80], that scales as $n^2 m_z$. Thus, the larger the number of points per subdomains, or polynomial degree, and the larger the number of subdomains in the vertical, more expensive will be to solve the Pressure Poisson Problem.

The length scale of the vertical overturn observed by *RCL2014*, at the region of interest, was considered to select a value for m_z. Field observations indicated that the length was no larger than 52m. Thus, the vertical number of subdomains is set to m_z = 25, so that for a water depth of 450m, a single subdomain

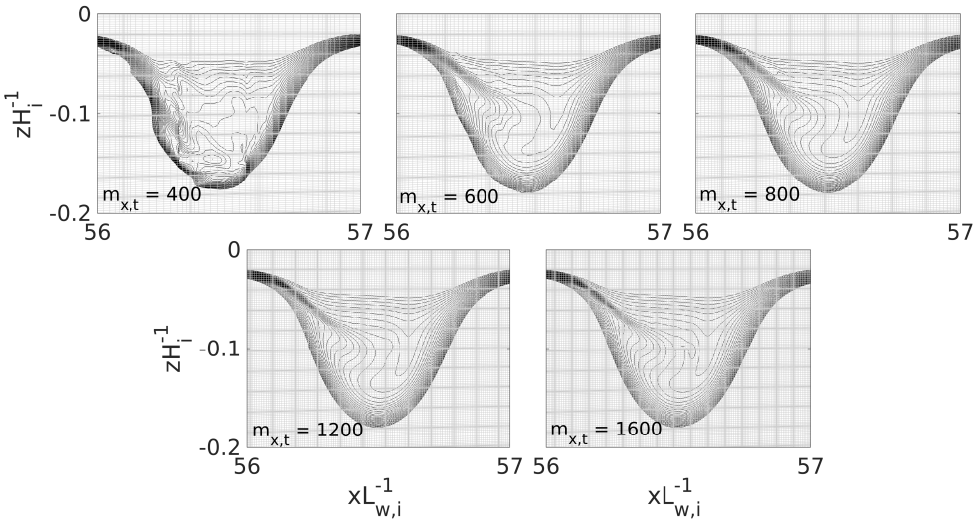

Figure 3.4: Isopycnals of the simulated shoaling ISW, at a water depth of 450m, using the SMPM flow solver. Each panel corresponds to a different number of subdomains in the along-wave, x direction (i.e. m_x); five different values were chosen: $m_x = 400$, $m_x = 600$, $m_x = 800$, $m_x = 1200$, and $m_x = 1600$. The number of subdomains in the vertical is $m_z = 25$ and the number of points per subdomain is $n = 15$. The vertical direction has been nondimensionalized by the intial water depth, $H_i = 921$m and the x direction by the initial ISW half-width, $L_{w,i} = 1{,}014$m, obtained from the DJL solution.

captures a length scale of approximately 20m, in the water column; twice this length scale is less than the observed vertical overturn.

Table 3.1 shows the properties of the computational grid employed in this study. No mesh refinement technique is applied throughout the simulations. The timestep size, Δt, is chosen so as to respect the CFL limit for the initial velocity scale and the grid properties; the limit is set to 0.50 for both the x and z direction. During the shoaling simulation, an adaptive timestepping method ensures that Δt is adjusted, if necessary, across all timesteps; timestep adjustement would result from a change in the wave velocity scales or due to the small-scale features of the subsurface recirculating core. Nevertheless, it is not known *a priori* if a timestep adjustment is necessary. The computational domain has a total of 4.5 $\times 10^6$ degrees of freedom (DOF). For reference, Figure 3.5 shows

Table 3.1: Computational Parameters for the 2D simulations presented in this study. The regions included are: Location I, the subsurface and surface mooring location, and Location II. Note that the Gauss-Lobatto-Legendre (GLL) grid is non-uniform locally in each element.

Parameter	Value	**Parameter**	Value
$\Delta \mathbf{x_{min}}$	2.241m	$\Delta \mathbf{x_{max}}$	13.89m
$\Delta \mathbf{z_{min,I}}$	0.640m	$\Delta \mathbf{z_{max,I}}$	3.967m
$\Delta \mathbf{z_{min,sub}}$	0.314m	$\Delta \mathbf{z_{max,sub}}$	2.254m
$\Delta \mathbf{z_{min,sur}}$	0.296m	$\Delta \mathbf{z_{max,sur}}$	1.838m
$\Delta \mathbf{z_{min,II}}$	0.254m	$\Delta \mathbf{z_{max,II}}$	1.578m
$\mathbf{m_x}$	800	$\mathbf{m_z}$	25
$\mathbf{n}$	15	$\Delta \mathbf{t}$	0.2s

the isopycnals at Location I, along with the SMPM grid superimposed in gray. There are approximately 60 points per ISW wavelength and 60 points per maximum isopycnal displacement. Across the transect, the vertical grid spacing decreases with decreasing water depth, as noted in Table 3.1.

To reduce the computations per time per timestep, the computational domain is partitioned into overlapping windows of approximately m_x = 128 by m_z = 25, which track the ISW as it shoals. Each window is approximately $16L_{w,i}$-long; the overlap region ranges from $6L_{w,i}$ to $7L_{w,i}$, depending on the waveform since the ISW is adjusting to the gently varying bathymetry. Once the wave reaches the end of a window, a new window is generated that contains part of the original window along with the next portion of the domain. The density and velocity fields are then copied inside the overlapping region, from the original to the new window. The total number of windows required for a SCS shoaling simulation is nine. This windowing technique decreases the DOFs to be solved by a factor of 6, thereby accelerating simulation of the shoaling ISW along the transect.

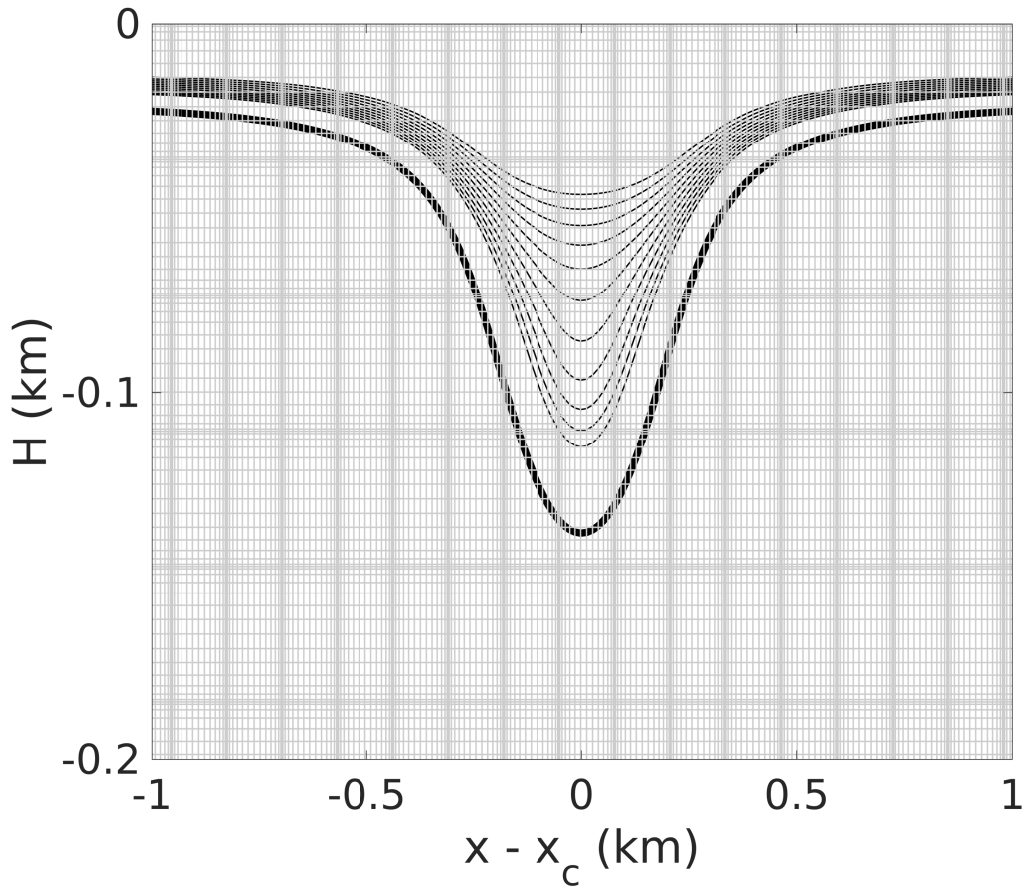

Figure 3.5: Internal Solitary Wave (ISW) at Location I with the superimposed GLL Grid (gray). The range has been shifted with the trough location, x_c. Eleven isopycnals are shown, along with the pycnocline (thicker solid-black line). The ISW field was obtained from the solution of the DJL Equation Solver [52].

Choice of Reynolds and Schmidt Number

The choice of Reynolds Number, $Re_{H_i} = c_i H_i/\nu$, and Schmidt Number, $Sc = \nu/\kappa$, considers that, the two-dimensional parameter space exploration has to be economical in terms of memory and run-time cost. Given that ISW shoaling process encompasses a broad range of scales up to $O(km)$, it is computationally expensive to simulate the shoaling problem with a field value Re_{H_i} and Sc because of the resolution required to describe the gently varying bathymetry over a long

propagation distance, the time-averaged profile of the background density and velocity field, the ISW length scales as the wave shoals, and finer-scales limited to the formation of the subsurface recirculating core and any finer-scale structure within. As such, the parameters were set to $Re_{H_i} = 2 \times 10^6$ and $Sc = 1$. Both are two orders of magnitude below that of the open ocean.

The impact that the chosen Re_{H_i} might have on the potential viscously-driven deceleration of the ISW over long distances, has been explored by simulating an ISW propagating over a flat domain, for a distance of approximately $15L_{w,i}$. Subsequently, the wave propagation speed was computed for both inviscid and viscous case, and compared with the theoretical DJL wave propagation speed. The relative difference was found to be locked at $O(10^{-3})$, for both Re_{H_i}, along the specified distance.

A three-dimensional study is required for examining the turbulent flow engulfed within the recirculating subsurface cores, but not necessarily the propagation of the ISW. Since the field observations of [103] indicated that, near the Dongsha slope, the waves propagates virtually along the same latitudinal coordinate, a two-dimensional approach to explore the shoaling process and the formation of the subsurface cores is justified; it can also provide an insight of the possible core dynamics. Nevertheless, ISW breaking is inherently a three-dimensional process, but the present objective is to explore the conditions that may lead to such breaking. Thus, simulating the shoaling problem with the given Re_{H_i} and a Sc of order unity may be reasonable for exploring the parameter space in this two-dimensional study.

3.3 Results

3.3.1 Wave Properties

The ISW may be tracked by locating the wave trough. At this location, there is a convergent zone [33] where $du'/dx = 0$, above and below the maximum isopycnal displacement. However, during subsurface core formation, the convective instability induces two-dimensional motion, leading to changes in the horizontal velocity. Below the trough no vertical motion motion exists; the convergence zone here can still be used to locate the ISW along the SCS bathymetric transect.

Figure 3.6(a) shows the position of the ISW trough as the solid-black line with markers; it is recorded at every 80 seconds of simulation time. Given that the ISW propagation speed varies along the SCS bathymetric transect, at the initial position, this sampling time corresponds to changes in the trough position of approximately 135m. As the water depth decreases and the ISW decelerates, the variations in position also decreased to approximately 100m.

Errorbounds were obtained by locating the convergence zone at different water depths, below the trough. The relative error is found to be $\leq 1\%$, suggesting that the approach to track the wave is reliable. Errorbars, characterizing the uncertainty in the displacement of the wave, are also included in Figure 3.6(a), but given the small difference these are minute and barely noticeable.

Two other regions within the ISW are identified and tracked: the front and lee of the wave. These may be defined by extracting the density profile for a given water depth, in the along-wave direction, and locating the middle density value from the departure of the reference background density. The front and lee

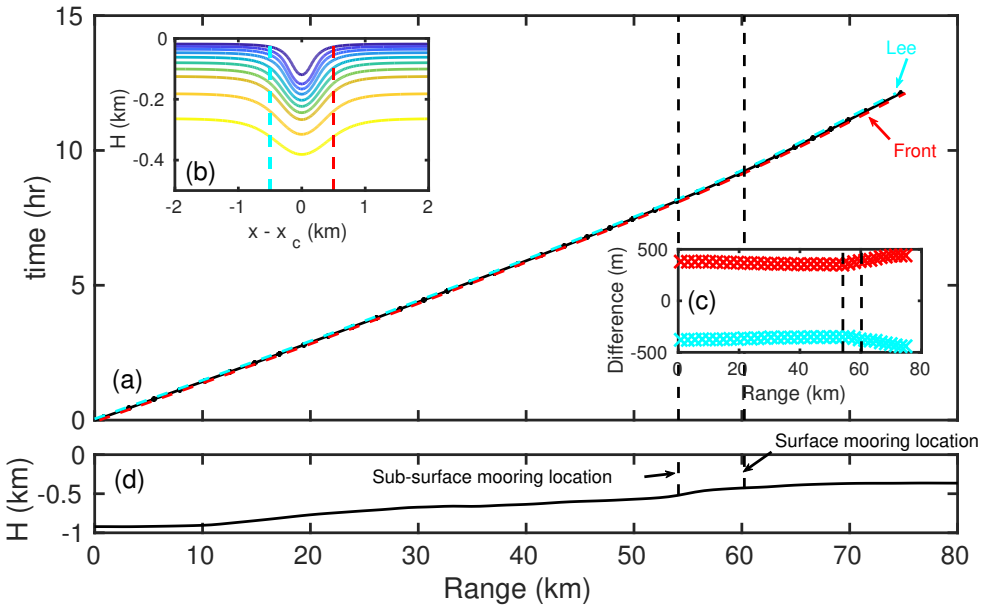

Figure 3.6: Position of the ISW along the SCS Transect. In (a), three distinct regions are tracked: trough (black-solid line), lee (cyan), and front (red); errorbars have been included for the trough position. These are minute, suggesting that the tracking method is reasonable. The exact location of the lee and front are shown in (b), along with the isopycnals of the ISW at Location I. The along-wave spacing between the front and lee relative to the trough is shown in (c). The full SCS transect is included in (d) with the location of the surface and subsurface moorings.

of the wave are shown in Figure 3.6(a) and 3.6(b) as red (lee) and cyan (front), along with the trough (black). Figure 3.6(c) shows the difference in the location of the lee and front, relative to the position of the ISW trough. Tracking these two points may be a proxy for visualizing changes in the wave symmetry during shoaling. The simulation indicates that the ISW is sensitive to the varying water depth, particularly at the subsurface mooring where the lee and front are further displaced from the trough, while propagating over the maximum slope of the transect. Nevertheless, the wave preserves its symmetric shape, agreeing with the adiabatic shoaling observed (see Section 3.1) in the field.

Computing the ISW Propagation Speed

The position of the ISW trough may be used to determine the propagation speed by performing a linear least-squares fit, using a linear model, of the data in Figure 3.6(a) and computing the slope of the linear fit. Such method is commonly applied to the estimate propagation speed in uniform depths. For shoaling ISWs, changes in bathymetry may significantly impact the speed calculation although the method may still applicable [123]. The fit range has to cover a sufficient distance, while considering the wave acceleration/deceleration due to the changing water depth.

The recorded water depth by *RCL2014*, and utilized as the SCS bathymetric transect in the present study (i.e. Figure 3.1), corresponds to a spatial resolution of 1-2 km, depending on the location along the transect. Thus a linear fit of the data in Figure 3.6, encompassing a range that is less than $L_{w,i}$, should provide a reasonable measure of the wave propagation speed. As mentioned in Section 3.3.1, the preset study captures the wave properties at every 80 seconds, or between 135m and 100m. This value is almost one order of magnitude below the distance between successive water depths measurements by *RCL2014*. As such, the linear least-squares fit provides a reasonably measure of the propagation speed, that is crucial to determining the formation of a subsurface recirculating core.

Computing the ISW Amplitude and Half-width

The ISW amplitude, A, is taken to be the maximum isopycnal displacement, obtained from $\eta(x, z, t)$. The half-width, L_w, is computed by first, integrating η in

the along-wave direction, then dividing by the amplitude [90]. For a given time, L_w is,

$$L_w = \frac{1}{A} \int_{-\infty}^{+\infty} \eta(x, z) dx'. \tag{3.6}$$

The ISW is expected to become convectively unstable along the SCS bathymetric transect, with a heavy-over-light fluid configuration (see Section 3.1). As such, the density field needs to be sorted adiabatically, to minimize the potential energy, prior to computing the wave length scales. The adiabatic redistribution of the density is accomplished via a probability density function of the density perturbation profile [189, 178], using a parallel sorting algorithm [154]. Assuming that the background density is invertible with inverse $\bar{z}_r(\rho)$, that satisfies the relation $\eta(x, z, t) = \bar{z}_r(\rho(x, z, t))$, the isopycnal displacement can then be obtained by computing the difference between the fluid parcel height based on the reference background density profile and the adiabatically rearranged density profile in the presence of the wave-driven disturbance, $\bar{z}_r(\rho)$.

Figure 3.7(a) shows the computed propagation speed, c, along with the maximum ISW-induced horizontal velocity, U_{max}. The amplitude, A, and half-width, L_w, of the ISW are shown in Figure 3.7(b) and 3.7(c). Figure 3.7(d) shows the water column depth to provide perspective of the SCS transect. In Figure 3.7(a) to 3.7(d), the black-dashed lines denote the location of the subsurface and surface mooring.

As the ISW shoals, the propagation speed and horizontal velocity decrease while the amplitude increases; an increase in amplitude leads to a decrease in half-width. The maximum amplitude is found to be approximately 153m, oc-

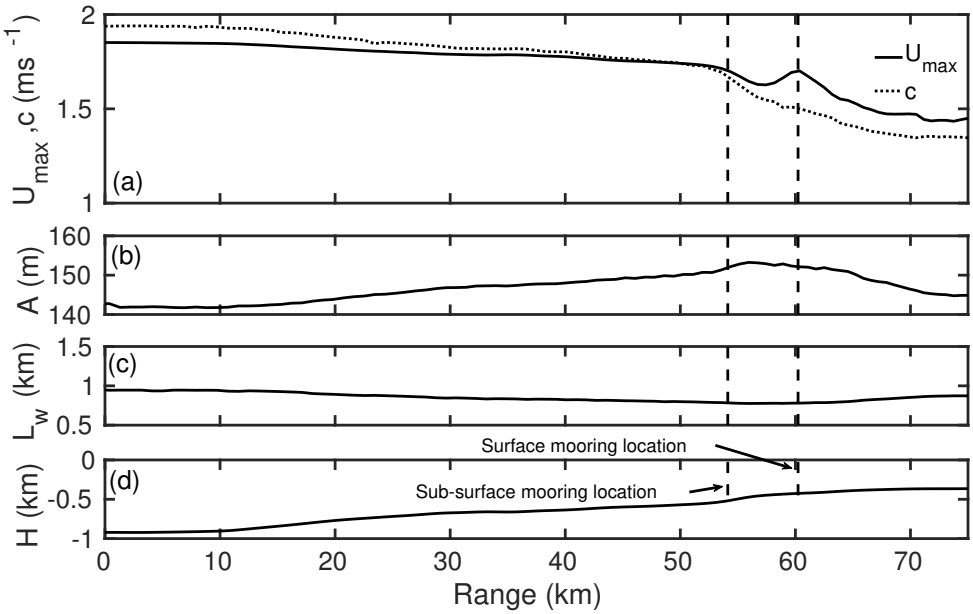

Figure 3.7: Computed properties of the shoaling ISW along the SCS transect. These are: (a) wave propagation speed and maximum horizontal velocity, (b) amplitude, and (c) half-width. The SCS transect is presented in (d) for reference. The black-dashed line corresponds to the location of the surface and subsurface moorings deployed by *RCL2014*.

curring at a range of 55.68km. Here, the half-width is L_w = 775. The changes across the length scales of the wave suggest that energy is conserved, in this two-dimensional study, as the wave grows in amplitude while decelerating.

3.3.2 Examining the presence of a convective instability

When the ISW reaches the location of the subsurface and surface moorings, the propagation speed has already decreased below U_{max}; the wave has entered the convectively unstable regime. Figure 3.8(a) to 3.8(c) show colored contours of the isopycnals of the shoaling ISW, at the subsurface and surface mooring along with Location II, where the SCS transect is the shallowest. In Figure 3.8(a), the isopycnals indicate the presence of a convectively unstable fluid and subsequent

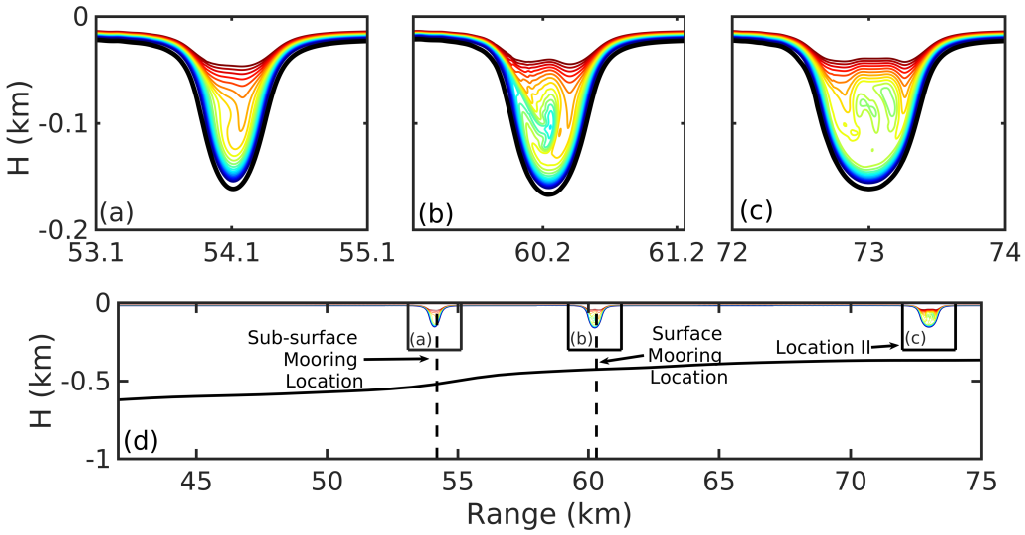

Figure 3.8: Isopycnal contour at select locations, during propagation of the ISW along the SCS transect. Three different snapshots, corresponding to different times after the start of the simulation at Location I. The exploded views in (a) and (b) correspond to the wave at the subsurface and surface mooring location, respectively. In (c), the ISW has reached the shallowest portion of the transect, Location II. In (d), the SCS transect is shown along with the placement of each snapshot.

overturning in the water column; heavy-over-light fluid configuration has been established. Once the ISW reaches the shallowest part of the transect, the ISW is propagating with an enclosed-isopycnal region. Heavy fluid appears to be trapped inside the wave, suggesting the presence of a recirculating core.

Figure 3.7 and Figure 3.8 indicate that the condition $U_{max} > c$ precedes the formation of the convective instability and, possibly, the recirculating core. That is, once the wave propagation speed decreases below the maximum horizontal wave-induced velocity following a short transitional window, a convective overturn ensues and the formation of a region with enclosed isopycnal subsequently occurs. These findings are consistent with simulations [94], and field observations [102, 103], where $U_{max} > c$ always preceded the generation of a

Table 3.2: Properties of the Internal Solitary Wave simulated in this study at the location of the surface and subsurface moorings. ISWs values are from Table 1 of *RCL2014* [103] via a combination of the ship survey and the moorings; these are included here. Their wave propagation speed was obtained near the surface mooring. The properties included are: Amplitude, A (m), half-width, L_w (m), propagation speed, c (ms^{-1}), and maximum ISW-induced horizontal velocity, U_{max} (ms^{-1})

Study	A	L_w	c	U_{max}
RCL2014	137	921	1.71	2.23
Simulation at Subsurface Mooring	151	783	1.67	1.70
Simulation at Surface Mooring	152	781	1.50	1.70

recirculating core. Note that, visualizing the density field may not be a clear indicator of recirculating fluid. A more robust approach would be to examine the streamline pattern in a reference frame moving with the ISW, which is addressed in Section 3.3.3.

Comparing simulated ISW with observations

Table 3.2 shows the observed and INSB-simulated ISW properties. *RCL2014* obtained the wave properties via a combination of the subsurface and surface mooring data with shipboard radar measurements. Some of the properties reported include: amplitude (A), half-width (L_w), propagation speed (c), and maximum horizontal wave-induced velocity (U_{max}).

When compared with the field wave, the simulated ISW varies significantly from that observed. At the subsurface and surface mooring, the wave amplitude is found to be 151m and 152m, respectively, along with a ISW half-width of 783m and 781m. The observed amplitude and half-width were 137m and 921m, respectively. The simulated propagation speed is $1.67ms^{-1}$ at the subsurface mooring and $1.50ms^{-1}$ at the surface mooring, which is 5 to 8% less than the

observational counterpart. Simulations indicate that U_{max} is between 1% to 13% greater than c, as opposed to the 30% observed.

Differences between the observed and simulated wave are expected since the DJL solution, used to simulate the shoaling process, was chosen without any observational input on the upstream conditions. The observed wave by *RCL2014* presumably had much different length and velocity scales at the initial water depth of the present study. At the depth of the moorings, the range of possible stable solutions of the DJL Theory, with the fields shown in Figure 3.2 used as initial background conditions, do not yield an solution for an ISW with the observed properties.

In addition, the assumption of a steady and homogeneous background current may not be realistic near the Donsha Slope. The ratio $U_{max}c^{-1}$ could change considerably if a different background current profile is used upstream. The background current could be steady for the time scales considered in the present study, but have a strong dependence in the normal-to-isobath direction, which can significantly impact the velocity field of the wave as it shoals.

When the simulated evolution of U_{max} and c is compared against the June 3 observed data shown in Figure 8(a) of *RCL2014*, the values in the present study also exhibit a decreasing trend up to the surface mooring. This is the location where the largest difference between U_{max} and c exists and this feature is captured in the simulation. After the surface mooring, the simulated evolution of velocity and propagation speed differs from the field data; the simulations do not exhibit close values of U_{max} and c. Since the present study is two-dimensional, where there is no physical mechanism by which energy can be dissipated, it may be possible that once U_{max} increases past c, the recirculat-

ing core forms and persists as the ISW continues shoaling over SCS bathymetric transect. Thus, the present simulation captures the essential qualitative aspects of the formation of the convective instability and recirculating subsurface core, but does not match quantitatively the observed wave.

3.3.3 Defining the recirculating core boundary

Figure 3.9 shows the simulated ISW, with the subsurface recirculating core at the subsurface (3.9(a)-3.9(c)) and surface (3.9(d)-3.9(f)) moorings, using three different recirculating core boundary definitions. In Figure 3.9(a) and 3.9(d), the visualized isopycnal range is saturated to resolve the trapped fluid. Figure 3.9(b) and 3.9(e) show the region where $U_{max} > c$ and Figure 3.9(c) and 3.9(f) show the streamlines for an observer in a reference frame fixed with the wave. The streamlines are obtained from the streamfunction

$$\psi(x,z) = \int_{-H}^{0} (u-c)dz, \tag{3.7}$$

where $u(x,z) = u'(x,z) + U(z)$; arrows are included to denote the flow movement across the ISW. The wave propagates with speed c, in the rightward direction, as denoted by the black arrow below the trough in 3.9(a) through 3.9(f). In Figure 3.9(a), 3.9(c), 3.9(d), and 3.9(f), localized contours are associated with trapped fluid. Note that, in Figure 3.9(a) and 3.9(d) the amount of contour lines has been deliberately increased to denote the trapped fluid.

Figure 3.9(f) appears to confirm the streamline structure of a subsurface recirculating core, as observed in the field [102]: two counterotating regions are

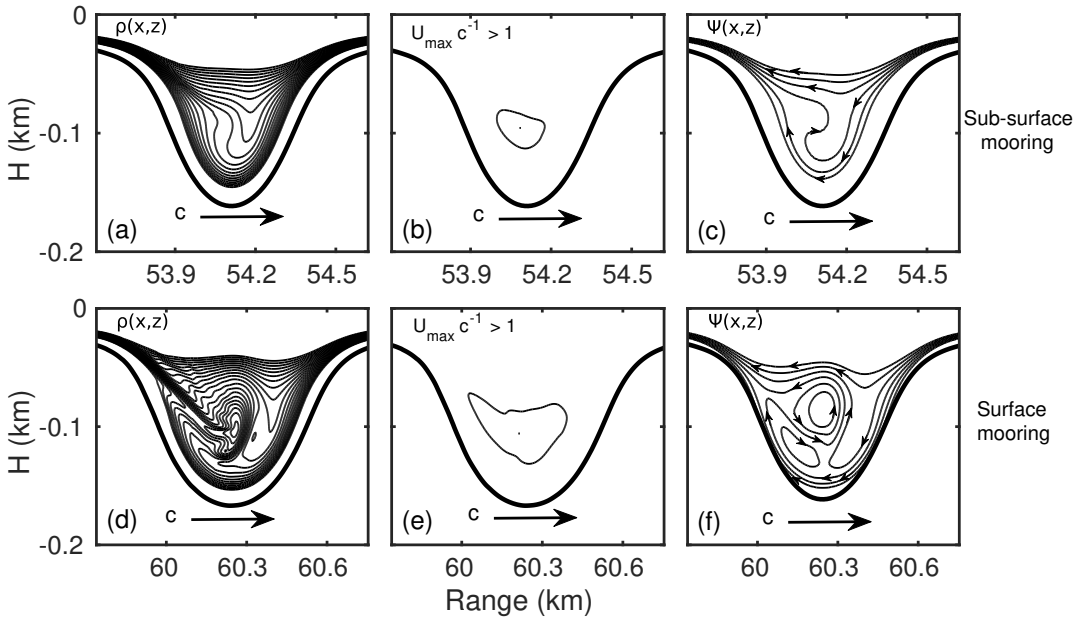

Figure 3.9: Visualization of the trapped fluid at the location of the subsurface ((a)-(c)) and surface mooring ((d)-(f)). Three definitions have been used to identify the recirculating core: (a) & (d) isopycnals, (b) & (e) $U_{max}c^{-1} = 1$, and (c) & (f) the streamfunction ψ for an observer moving with the wave along with arrows denoting the direction of the flow entering the ISW. In (a) through (f), the rightward pointing arrow, below the trough, denotes the wave propagation direction, with speed c. The thick solid-black line corresponds to the displaced pycnocline.

noticeable, as opposed to one which is indicative of surface-type cores (see Figure 2 of Ref. [102]). In addition, if the value $U_{max}c^{-1} = 1$ is used to represent the boundaries of the subsurface recirculating core, then at the subsurface mooring (Figure 3.9(b)) the length and height of the core are found to be $l_c = 180$m and $h_c = 28$m, while at the surface mooring (Figure 3.9(e)) the length and height of the core are found to be $l_c = 370$m and $h_c = 45$m, respectively. Using the same value, *RCL2014* observed $l_c = 306$m and $h_c = 52$m. The simulated core height at the surface mooring is relatively close to the observed values, but the core length is 20% larger, suggesting that more, heavier fluid is trapped than what was actually observed.

Recirculating cores leak the trapped fluid into the ambient during ISW propagation. Therefore, not all the fluid contained within the region $U_{max}c^{-1} > 1$ may be effectively trapped. A more robust definition of the core boundary may involve the use of Lagrangian coherent structures (LCS) [107]. With LCS, the boundary is demarcated by obtaining the intersection between forward and backward ridges of the Finite-Time Lyapunov Exponent (FTLE) field. This method has been used to identify the vortex regions in three-dimensional incompressible flows [65] and also within the framework of high-order spectral methods for gyre flow, vortex advection by uniform flow, and viscous flow around square cylinders [131]. Thus, future subsurface recirculating cores simulations could incorporate an LCS scheme to formalize the boundary definition.

3.3.4 Evaluating the effect of the slope near the moorings

The maximum slope value of the SCS transect, shown in Figure 3.1(c), is computed to be approximately 2.8% and occurs near the location where the mooring were deployed in the field. Field data indicates that only at this region in the SCS are recirculating subsurface cores possible [102, 103]. As such, the maximum slope value may play a pivotal role in core formation. To address the slope effect, a separate simulation is performed with a bathymetric transect where the maximum slope value is attenuated via a combination of filtering and cubic interpolation of the bathymetry data, to maintain continuity of the depth and slope. The result is a modified SCS transect with a maximum slope of approximately 1.5%, as shown in Figure 3.10(a). The original (black) and modified (blue) slope are shown in Figure 3.10(b).

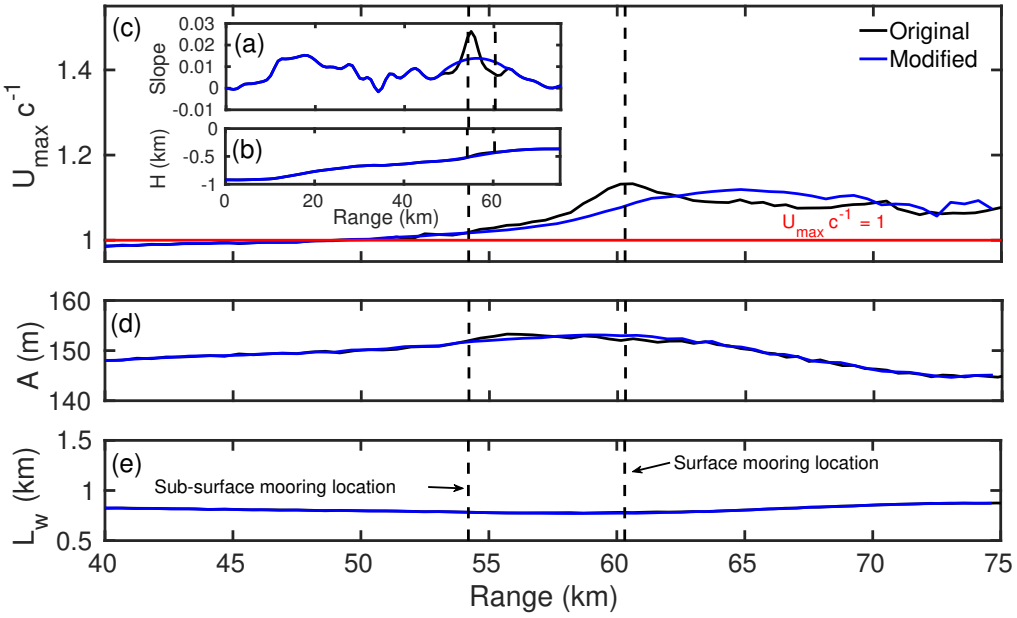

Figure 3.10: ISW properties of a shoaling wave using the original (black) and modified (blue) SCS transect. In (a) and (b), the original and modied slope and bathymetric transect, respectively, are shown. In (c), the value of $U_{max}c^{-1}$ is shown along the transec. The solid-red line corresponds to the convective instability threshold of $U_{max}c^{-1} = 1$. In (d) and (e), the amplitude and half-width are shown. The location of the subsurface and surface moorings is represented by the black-dashed line in (a) through (e).

The maximum horizontal velocity and propagation speed are shown in Figure 3.10(c). The black and blue line correspond to the original and modified transect, respectively. With the modified transect, and the previously chosen DJL solution, the simulation produced no significant change in the formation of a convective instability, since $U_{max}c^{-1} > 1$ still occurred. Consequently, subsurface recirculating cores may be expected. However, the location along the SCS bathymetric transect where $U_{max}c^{-1}$ was the largest changed from approximately 60km for the original to 65km for the modified. Both simulations suggest that the ISW remains convectively unstable with $U_{max}c^{-1} > 1$ throughout the rest of the transect. The maximum recorded bottom slope causes the formation of the convective instability earlier, but the ISW becomes convectively unstable

regardless. Figure 3.10(d) and 3.10(e) show the amplitude and half-width, respectively, for both original and modified SCS transect. No changes in the ISW length scales were noted.

Finally, Figure 3.11(b) and 3.11(d) show the streamline contour for the modified transect at the subsurface and surface mooring location, respectively; closed streamlines are not present for the modified case, although 3.11(d) suggest that the subsurface recirculating core is in the process of forming. In addition, the size of the convectively unstable region may be obtained by considering where $U_{max}c^{-1} = 1$; it is shown as the solid-magenta line in 3.11(b) and 3.11(d). At the location of the subsurface mooring, its length scales are l_c = 120m and h_c = 19m, while at the surface mooring l_c = 330m and h_c = 40m. These values are approximately 10 - 50% smaller than those from the original transect, suggesting that the amount of heavy fluid plunging forward, into the ISW, is influenced by the presence of the maximum slope and possibly it is unique to the region. Thus, convectively unstable ISWs with recirculating subsurface cores may be occurring elsewhere, but not as noticeable as those near the Dongsha Slope.

3.4 Discussion

3.4.1 Variations with Initial ISW Amplitude

Since the examined ISW in Section 3.3.3 had an initial amplitude and propagation speed that may not have corresponded to the observed wave at deeper waters, shoaling simulations are conducted with initial waves obtained from the solution of the DJL Equation with larger isopycnal displacements, at the depth

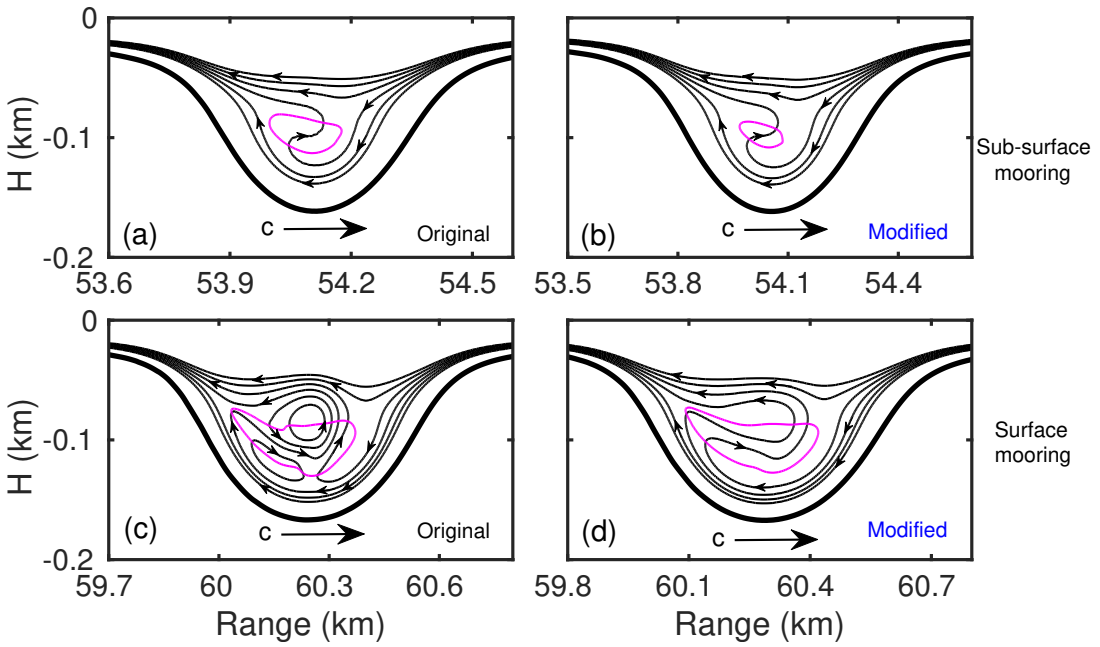

Figure 3.11: Streamlines of the ISW for the original and modified SCS transects, at the location of the subsurface and surface moorings. The ISW propagates from left-to-right with speed c. The streamlines are computed in a reference frame moving with the wave. Arrows are included to denote the direction of the movement of water across the wave. In (a) and (b), the streamlines are shown for the location of the subsurface mooring, while in (c) and (d) for the surface mooring. The region where $U_{max}c^{-1} > 1$ is included in (a) through (d) as the solid-magenta line.

H_i. Larger initial amplitudes are favored over smaller because field observations [102] indicated that for an ISW shoaling over the Dongsha Slope, the wave had a larger amplitude at deeper waters.

An objective of the present study is to examine how the properties of the shoaling ISW, and subsurface recirculating core, vary with initial ISW amplitude. The DJL Solution, corresponding to a initial wave with an amplitude of 167m, was found to be convectively unstable and therefore is set as the upper bound of selected initial amplitudes. The lower bound is the previously studied wave with A_i = 143m.

Figure 3.12 shows the ISW properties, as a function of the initial wave amplitude, for the new simulations. The observed ISW properties are also included as the black-circle marker; the values are obtained from Table 1 of *RCL2014*. Rather than include the separate evolution of U_{max} and c, the ratio of $U_{max}c^{-1}$ is computed and presented instead. Regardless of initial amplitude, a convective instability occurs because $U_{max}c^{-1} > 1$ for all cases; subsurface recirculating cores exist. In addition, the location where $U_{max}c^{-1} = 1$, and consequently convective breaking occurs, varies along the transect for each case. That is, each colored line crosses the $U_{max}c^{-1} > 1$ threshold at different locations along the SCS bathymetric transect; larger ISWs appear to become convectively unstable earlier. Figure 3.12 also shows the ISW amplitude and half-width of the simulations along with the bathymetry. In a two-dimensional framework, the shoaling ISWs are expected to increase in amplitude and decrease in half-width, as they propagate into shallower waters, by virtue of conservation of energy [162]; Figures 3.12(b) and 3.12(c) confirm this argument.

No internal solitary waves are found to reach the observed value $U_{max}c^{-1} = 1.30$, although all waves exhibit the maximum ratio close to the surface mooring as the field observations indicate. In addition, the simulations also do not match the observed amplitude and half-width. Given the simulated profiles of $U_{max}c^{-1}$, a value of 1.30 would be possible for an even larger initial wave. Stable solutions of the DJL Equation, with a larger isopycnal displacement can be obtained, but only in deeper waters. Thus, the transect, including the artificial plateau, would have to be elongated to account for the larger wave. With the larger domain, rotational effects must be included and the shoaling process would result in an ISW that may or may not match the observed wave properties of *RCL2014*.

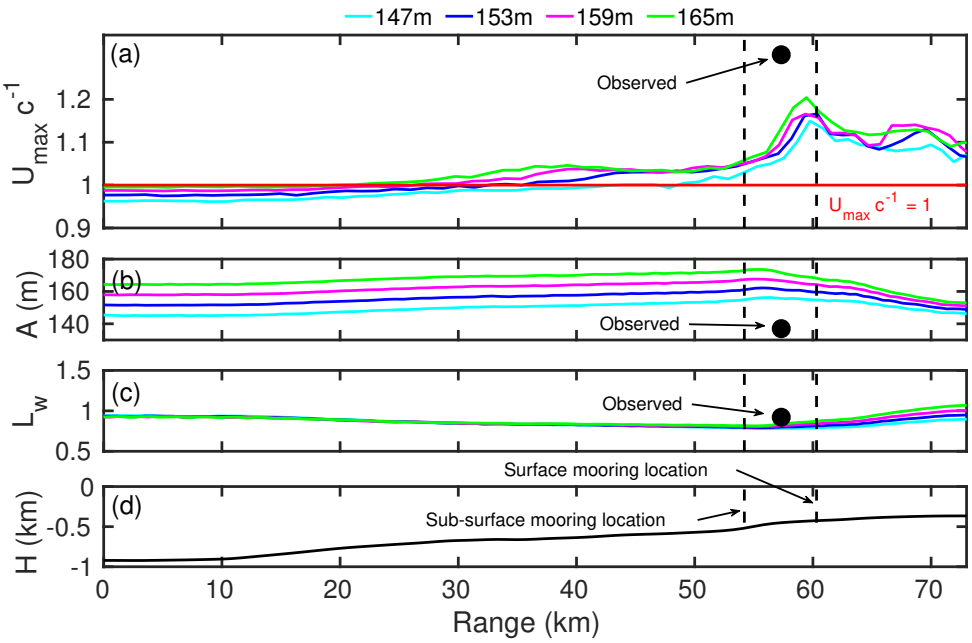

Figure 3.12: ISW properties for various initial amplitudes as a function of location along the SCS transect. Four different amplitude values are shown: $A_i = 147m$ (cyan), $A_i = 153m$ (blue), $A_i = 159m$ (magenta), and $A_i = 165m$ (green). In (a), the ratio $U_{max}c^{-1}$ is shown, including the $U_{max}c^{-1} = 1$ threshold (solid-red line). In (b) and (c), the amplitude and half-width, respectively, is shown along with the observed values (black circle). The SCS transect is included in (d) along with the location of the subsurface and surface moorings (black-dashed lines). The observed values were obtained from Table 1 of *RCL2014*.

If a larger wave is chosen as the initial condition, then, given the framework of the present two-dimensional study, the ISW will have a bigger amplitude near the mooring locations. This contradicts observations where a convectively unstable wave, with a recirculating subsurface core, decreased in amplitude while shoaling [102]; these have noted that the presence of the core contributes to the energy dissipation of the wave as it shoals, thereby reducing the maximum isopycnal displacement.

Finally, the wave properties at the subsurface and surface mooring locations are shown in Table 3.3; the data also includes the height and length of the convectively unstable region where $U_{max}c^{-1} > 1$; it is characterized by a height, h_c,

Table 3.3: Properties of the simulated ISWs at the subsurface and surface mooring location, for a given initial amplitude A_i. The rest of the parameters are: wave propagation speed, c (ms^{-1}), maximum ISW-induced velocity, U_{max} (ms^{-1}), Amplitude, A (m), half-width, L_w (m), convectively unstable region length, l_c (m), and convectively unstable region height, h_c. The convectively unstable region is defined as the part in the interior of the wave where $U_{max}c^{-1} > 1$.

A_i (m)	mooring	c	U_{max}	A	L_w	h_c	l_c
147	subsurface	1.68	1.73	154	787	25	170
	surface	1.51	1.73	154	789	41	330
153	subsurface	1.69	1.77	160	795	36	240
	surface	1.51	1.76	159	815	41	420
159	subsurface	1.70	1.78	167	801	37	300
	surface	1.51	1.77	164	838	45	480
165	subsurface	1.72	1.81	172	816	41	330
	surface	1.51	1.79	168	869	47	530

and a length l_c. Simulation results indicate that a larger initial ISW, that results in a greater isopycnal displacement near the moorings, will develop also a larger unstable region. However, the field observations of *RCL2014* indicate that the observed unstable region had a height of approximately 52m; no ISW reaches the observed value although all achieve the largest unstable region dimensions at the surface mooring location. As such, the present two-dimensional simulations do not match the observed wave properties but they do describe the process by which the ISW becomes convectiely unstable and a subsequent subsurface recirculating core forms, with the recorded field data.

3.4.2 Variations in near-surface background shear

The sensitivity of the formation of the subsurface recirculating cores to the background current is explored in this study by modifying near-surface region (i.e. $H > -20m$) of the latter. Figure 3.13(a) shows the original baroclinic back-

ground current profile, $U(z)$ (solid-blue line), along with two new profiles: $U_r(z)$ (dashed-blue line) and $U_l(z)$ (dotted-blue line). The background shear, $U_z(z)$, for all profiles, is shown in Figure 3.13(b). The $U_r(z)$ and $U_l(z)$ profiles are obtained from the $U(z)$ profile, except for the top 20 meters of the water column where the interpolation basis function is modified to result in a different value at the surface; all background current profiles are identical below 20m. The resulting profile for $U_r(z)$ has a maximum shear of -0.257 s^{-1} and -3.377 s^{-1} for $U_l(z)$; both are located the surface. The values are significantly different than the original $U = -1.955$ s^{-1}, also at the surface, and are a result of the choice of basis function; these cannot be changed without impacting the continuity in the solution, when differentiating the background current profile. Note that regardless of the near-surface value, subsurface recirculating cores may be expected so long as the background current vorticity is opposite to that of the wave [67].

The solution of the DJL Equation, used for the study of the near-surface variation in the background current profile, has a prescribed initial amplitude of A_i = 143m. Figure 3.13(c) to 3.13(e) show the evolution of the wave properties of the ISW, along the shoaling track, with the original and modified background velocity profiles. In Figure 3.13(c), the profile of the ratio $U_{max}c^{-1}$ for both modified profiles follows that of the original; all three achieved $U_{max}c^{-1} > 1$. In Figure 3.13(d) and 3.13(e) no significant difference in the ISW properties is observed for the modified profile cases. As such, the magnitude of the near-surface background shear does not change the properties of the shoaling ISW.

Finally, Table 3.4 shows the properties of the ISW at the location of the surface and subsurface mooring. There is no variation in velocity, wave propagation speed, amplitude, and half-width between profile (i.e. $< 1\%$). However,

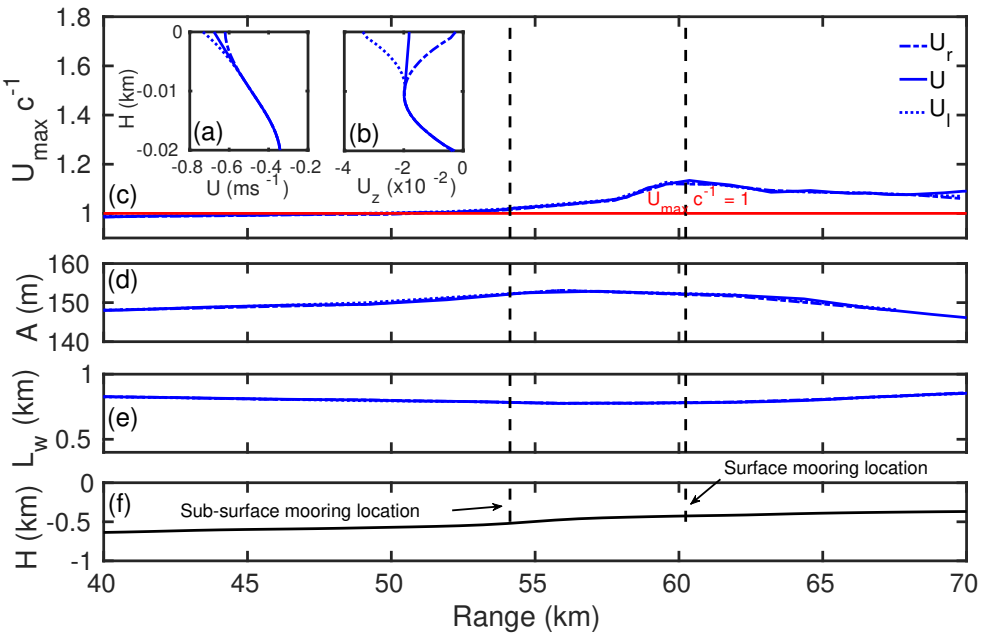

Figure 3.13: ISW properties along the SCS transect for the case of modified and original near-surface time-average profile of the background current. The time-averaged profiles of background current, U, and shear, U_z, are included in (a) and (b) respectively. The original profile is the solid-blue line, used in all previous simulations. The modified profiles are U_r (dashed-dotted line) for a magnitude smaller than U and U_l (dotted line) for a magnitude smaller than U. In (c), the ratio of $U_{max}c^{-1}$ is shown throughout the transect. The amplitude and half-width is shown in (d) and (e). The SCS transect is shown in (f) (c). In (c) through (f), the black-dashed lines corresponds to the location of the subsurface and surface moorings deployed by *RCL2014*.

the length scales of the convectively unstable region slightly vary at the surface mooring location, across cases. For instance, the height, h_c, is larger for the simulation with $U_l(z)$ than that of U and $U_r(z)$, with the difference between approximately 6% and 30%, respectively. As such, the magnitude of the shear at the free surface influences the size of the convective instability and, possibly, the size of the subsurface recirculating core: the larger the magnitude the larger the unstable region.

Table 3.4: Properties of the simulated ISW, with the modified background current profile presented in Figure 3.13, at the subsurface and surface mooring location. The parameters include wave propagation speed , c (ms^{-1}), maximum ISW-induced velocity, U_{max} (ms^{-1}), Amplitude, A (m), half-width, L_w (m), convectively unstable region length, l_c (m), and convectively unstable region height, h_c (m). The convectively unstable region is defined as the part in the interior of the wave where $U_{max}c^{-1} > 1$.

Profile	Mooring	c	U_{max}	A	L_w	l_c	h_c
U_l	subsurface	1.66	1.70	152	779	150	20
	surface	1.50	1.71	152	777	340	48
U	subsurface	1.67	1.70	151	783	180	28
	surface	1.50	1.702	152	781	370	45
U_r	subsurface	1.66	1.70	151	784	120	20
	surface	1.50	1.71	152	782	330	37

3.4.3 Examining the presence of a convective instability based on the ISW amplitude

The convective breaking of an ISW may be established by comparing the incident wave amplitude, A, with the thickness of the bottom layer of the water column, for a given bed slope. The bottom layer thickness is obtained by subtracting the pycnocline depth, z_o, from the total water depth, H. Experimental and theoretical data proposed three different regimes that describe the breaking processes a shoaling ISW experiences: convective breaking if $A/(H - z_o) > 0.4$, shear breaking if $0.3 < A/(H - z_o) < 0.4$, and no breaking (stable) for $A/(H - z_o) < 0.3$. Previous work found in the literature considered experimental and theoretical studies, using an idealized steep slope-shelf [71] and steep slope bathymetry [69].

In the present study, the amplitude breaking criterion is applied to all simulations, using the background conditions shown in Figure 3.2. Figure 3.14 shows

the results for $A_i = 143m$ (black), $A_i = 147m$ (cyan), $A_i = 153m$ (blue), $A_i = 159m$ (red), and $A_i = 165m$ (green). The modified bottom slope results are also included as the black-circle markers. Note that these have a different slope value at the corresponding mooring locations. The threshold values noted in the literature [69, 183] are specified as the red and black solid lines, respectively. All simulated ISWs with the original slope reach the convective breaking value of 0.4 at the surface mooring location, not at the subsurface mooring location. The field observations of *RCL2014* reported an approximate value of 0.4 near the moorings, for their June 2 wave.

However, the modified slope results do not reach the convective instability limit. At the subsurface mooring location, the wave is considered stable while at the surface mooring location, it is within the shear instability region. Nevertheless, as shown in Figure 3.10 and 3.11, the wave does experience a convective instability as $U_{max} > c$. Hence, convective breaking may also be associated with the preexisting background current and density field [94, 168, 95, 165], and not only with the wave length scales.

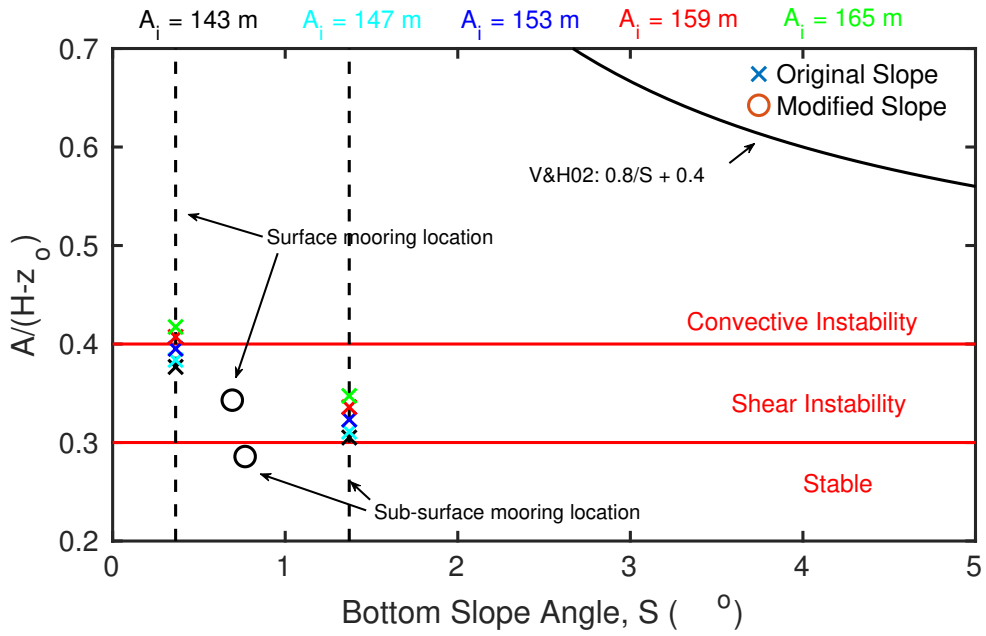

Figure 3.14: Breaking criteria based on the bottom bed slope, S, vs the ISW amplitude normalized by the thickness of the bottom layer of the water column. The results of five different simulations with the observed SCS bottom slope are included as colored-cross markers; these are: A_i = 143m (black), A_i = 147m (cyan), A_i = 153m (blue), A_i = 159m (red), and A_i = 165m (green). The dashed-black lines corresponds to the location of the subsurface and surface moorings for the original slope. Results for the modified slope with A_i = 143m are included as black-circle markers. The solid-red lines corresponds to the instability threshold values, proposed in the litrature [71, 69]: convective breaking above 0.4, shear breaking between 0.4 and 0.3, and stable below 0.2. The numerical fit (V&H02)[183] is denoted as the solid-black line.

CHAPTER 4

AN ALTERNATIVE PERSPECTIVE ON THE INSTABILITY IN AN INTERNAL SOLITARY WAVE OF DEPRESSION SHOALING OVER GENTLE SLOPES

4.1 Introduction

Internal Solitary Waves (ISW) of depression in the ocean, characterized by their large displacement of the pycnocline, have been observed to become unstable as they propagate over gentle slopes [125, 102, 103]. As mentioned in Chapter 1.3 and 2.1, an unstable ISW dissipates its kinetic energy, through the wave-shear, enhances turbulence-induced fluid mixing, and may transport suspended material across significant distances; such features can have a profound impact in the properties of the water column. The wave also interacts with the bottom by inducing a boundary layer separation, that may be strong enough to produce vortex shedding and impact the bed [20, 43, 169].

When Internal Solitary Waves shoal, any possible change in waveform can induce an instability that may result in wave breaking. Shoaling occurs when the wave adjusts to the changing water depth, as it reaches shallower waters. The instability can either be shear-based or convective-based. A shear-based instability occurs when the shear force is significant, relative to the buoyant force associated within the stratified water column; buoyancy inhibits vertical motion, dampens turbulent motion, and suppresses turbulence production from the velocity shear.

The dimensionless parameter that characterizes how significant is the shear

force in a stratified flow is known as the Richardson number. A commonly used definition of the Richardson number is the Gradient Richardson number (Ri), defined as,

$$Ri = \frac{N^2}{\left(\frac{\partial u}{\partial z}\right)^2}, \tag{4.1}$$

where N^2 is the Brunt-Väisälä Frequency (BV) and $\partial u/\partial z$ is the horizontal velocity shear, in the along-wave direction. The BV Frequency is defined as,

$$N^2 = -\frac{g}{\rho_o}\frac{d\overline{\rho}}{dz} \tag{4.2}$$

where g is the gravitational constant, ρ_o is the reference density, and $\overline{\rho}$ is the background density profile, in the absence of any wave-driven pertubation. The reference density is usually taken to be the density value at the pycnocline, where the maximum N^2 occurs. The canonical critical Richardson number, required for stability in a stratified and *parallel* shear flows is $Ri = 1/4$ [119]; flows with values above the critical limit are considered stable whereas flows with values below are prone to shear-based instabilities. Since ISW have a different time scale than that of flows with a critical $Ri = 1/4$, studies indicate that the critical Ri is closer to 0.10 [55, 14, 56, 30].

The most common manifestation of shear instabilities in a ISW is the Kelvin-Helmholtz (KH) Instability, where the interface of the velocity shear profile coincides with pycnocline location [89]. As the interface is perturbed, the density rolls up into billow-like structures that entrain and mix ambient fluid within; the mixing thickens the interface. KH instabilities have been observed in shoaling

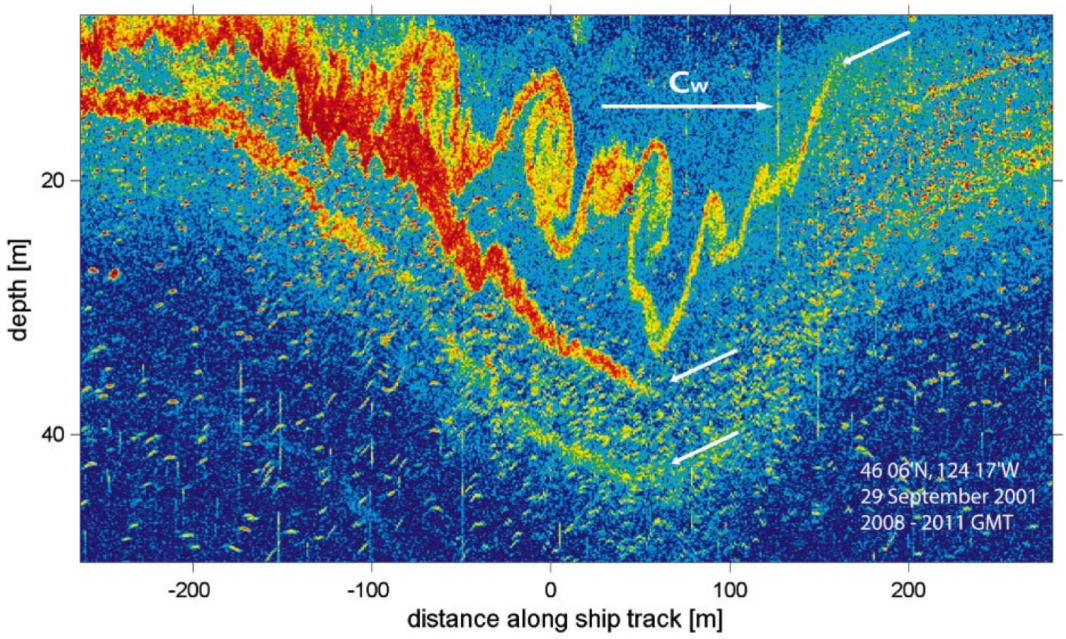

Figure 4.1: Echosounder image of a propagating ISW, in the Oregon Continental Shelf, exhibiting shear instabilities of KH-type. The image was obtained from Ref. [125]. The wave propagates from left-to-right.

ISWs [125] and also in simulations [55, 14, 56, 29, 30].

As explored in Chapter 3, the convective instability occurs when the wave-induced horizontal velocity exceeds the wave propagation speed [148, 37, 135, 48, 114, 83]. That is,

$$U_{max} > c, \tag{4.3}$$

where U_{max} is the maximum ISW-induced horizontal velocity and c is the wave propagation speed. An ISW that experiences a convective instability is characterized by the sudden steepening at the rear, caused by the rise of heavy fluid from the lower layer of the water column. This heavy fluid enters the region above the wave trough, where lighter fluid resides, causing an unstable fluid

configuration. As the fluid restratifies, highly turbulent convective motion occurs, enhancing mixing and dissipating energy in the water column. Internal Solitary Waves that become convectively unstable have been observed in the field [128, 141, 102, 103, 191], experiments [71, 69, 64, 28, 107], and simulations [94, 95, 57, 100, 72, 165, 87, 30, 108, 99, 109]. Concurrently, convectively unstable ISWs may also transport mass across large distances (i.e. $O(km)$) [121].

When an ISW shoals over gentle slopes (i.e. $S < 0.03$), the wave may become convectively unstable, and possibly develop a recirculating core. The core compresses the pycnocline, and may induce shear-type instabilities that are generated at the trough and washed downstream as the wave propagates [28, 30]. As such, both convective and shear instabilities may coincide [97], further increasing energy dissipation and mixing in the water column.

The existence of cores may be linked to the presence of near-surface background vorticity, associated with either the background density profile or the background current profile, or both. If there is no preexisting vorticity, then the ISW may become convectively unstable [71] but no core will form [94]. In addition, depending on the sign of the near-surface vorticity from the background current profile, cores may be either surface or subsurface [67]. Surface cores are characterized by a single recirculating region at the free-surface. Subsurface cores have been observed to contain two recirculating regions closer to the maximum isopycnal displacement [102]. ISWs with subsurface cores have been shown to be result in the largest energy dissipation and mass transport, yet only observed in a single location, near the Dongsha Slope in the South China Sea (SCS)[102, 103].

As previously mentioned, an ISW may be subjected to both types of instabil-

ities, although no field observations have noted the existence of such wave. It is possible that the measuring instruments lack the spatio-temporal resolution necessary to capture both types of instabilities, simulatenously. Observations of ISWs with subsurface recirculating cores do not show an ISW also exhibiting shear-instabilities [102], yet the water column properties are favorable for their formation [103] because the Richardson number was $Ri < 0.10$.

The observed ISWs with subsurface recirculating cores also exhibited favorable conditions for the presence of shear instabilities [103]. Realizing the likelihood of the existence of both instability mechanisms, it may be possible to perform highly accurate numerical simulations, that incorporate the observed background water column properties, in the absence of the waves. In Chapter 3, the formation of convective instabilities and subsquent recirculating subsurface core, over gentle slopes, was explored. It was found that while the wave properties of the simulated wave did not match the observed wave [103], the cores would still form regardless of the magnitude of the near-surface vorticity or the maximum slope located near the subsurface and surface moorings. No shear-based instabilities were simulated, although it was still possible that, at the trough of the wave, the shear force was strong enough to trigger the instabilities; yet with the chosen computational resolution these were not captured.

To address the shoaling of an ISW, the spectral multidomain penalty method (SMPM), originally developed for the study of turbulent wakes in stratified flows [41], has been adapted to incorporate high-order polynomial interpolation for representation of boundaries [80], thereby being able to make use of observed bathymetric profile also studied in Chapter 3. It has also been extended to include a third, lateral direction with a Fourier expansion, preserving

the highly-accurate nature for capturing the flow physics. The 3D SMPM spectrally solves the incompressible Navier-Stokes Equations under the Boussinesq Approximation [92], by penalizing the discretized operators [58, 59, 73] and applying a spectral filter in all three directions, considered to be a stand-alone subgrid-scale model [22, 42].

For a shoaling ISW over gentle slopes, convective instabilities may be anticipated by examining the background current and density structure. As long as there is near-surface vorticity, associated with the vertical gradient of either the background current or density field, convective instabilities may be expected [94, 97, 67]. In the context of shear instabilities of KH-type, these would be noticed near the trough of the wave, where initially $Ri < 0.25$.

Aside from the critical Richardson number of 0.10, there are two other requisites necessary for the formation of shear instabilities in shoaling ISWs. First, the region where initially $Ri < 0.25$ at the trough, must be large enough as the wave shoals for the instability to be triggered; this region has to be approximately 86% of the ISW half-width [56]. Second, the growth rate of the instability has to be larger than the ISW timescale [177]; otherwise any possible instability that would result in a KH-type instability would simply be damped out, or appear as small oscillations of the pynocline [14], behind the wave. Typically, the instability timescale has to be five times larger than that of the propagating ISW [14, 29].

Motivated by the field observations of subsurface cores in shoaling ISWs over gentle slopes, and the results obtained in Chapter 3, in this Chapter the shoaling process is also examined with the water column properties recorded by Dr. Ren-Chieh Lien and his team in the SCS, during the summer of 2011.

Since the team also recorded the varying water depth, as they tracked the waves, both the fluid properties and the SCS bathymetry can be incorporated to the 3D SMPM flow solver. Similar to Chapter 3, the work published from their deployment is thereby referred to as *RCL2014* [103]. Worthy of note is the direction of propagation of the ISWs, which was fairly constant and locked at approximately Lat. 21^o N, towards the west. Thus, no changes in water depth need to be included in the lateral direction (i.e. into the page), and the use of a Fourier expansion along this dimension is justifiable.

In the SCS, the ISWs were tracked for four days, near the Dongsha Slope in the SCS, at Lat. 21^o N, Lon. 117.5^o E. The data was obtained from two deployed moorings and ship measurements. The *RCL2014* study is the second ever record of subsurface recirculating cores, formed after the ISW has become convectively unstable; the first one was also accomplished by Dr. Lien and his team [102]. With the *RCL2014* measured density and background current profiles, and the results of Chapter 3, one known type of instability can be expected. No shear instabilities were recorded during their expedition, although it may be possible that these were not captured by the deployed instruments, due to resolution limitations, despite the water column properties being favorable for their formation.

The formation of the subsurface recirculating core was studied in Chapter 3, in two-dimensions. To this date, no previous work has examined the formation of subsurface recirculating cores, in three-dimensions, although three-dimensional studies of convectively breaking gravity waves have been accomplished. These have highlighted the excitation of higher modes during the breaking process [10] and the emergence of secondary, spanwise structures that

generate potential vorticity [188]. According to Ertel's Theorem of Potential Vorticity (PV), any changes in PV are caused by energy dissipation [92]. In addition, the lateral structures contribute development of finer motion that leads to mixing and dissipation [49, 55, 12]. As such, the present three-dimensional study may set precedent for how energy is redistributed and possibly dissipated, as the ISW shoals, breaks convectively, and a subsurface core is formed.

The objective of the present study is to examine the formation of either convective, shear, or both, instabilities for the shoaling ISW over gentle slopes, originally introduced in Chapter 3. The focus is placed on whether the observed field conditions of *RCL2014* can support the simultaneous instabilities, using a high-order simulations. The following questions guide the study: are shear instabilities also possible for the shoaling ISW over gentle slopes? Is the expected convective instability predominantly 2D? What role does the background current play in the ISW energetics? How does the evolution of the gravest lateral instability compares with the 2D development of the convective overturn?

The simulations build on the explored parameter space presented in Chapter 3, by utilizing the baseline ISW, with an initial amplitude of 143m, along with the observed background density and current profiles of June 2, 2011 from *RCL2014*, in addition to the measured water depth in the South China Sea. The computational grid resolution is doubled in the horizontal, in anticipation of smaller scale structure development; no refinement is needed in the vertical as the used resolution is assumed to be adequate. A two-dimensional run is initialized until the location of interest in the SCS, defined as that where *RCL2014* deployed the subsurface and surface moorings. Once the ISW is known to be convectively unstable, the simulation is restarted in three-dimensions, shortly

before the instability occurs, and the wave evolution modeled.

The work contained in this chapter is presented as follows: Section 4.2 discusses the methodology which includes the problem geometry, governing equations, and simulation description. Section 4.3 includes the results in two-dimensions along the lateral vorticity and Richardson number. The evolution of Kinetic Energy (KE) and Available Potential Energy (APE) is also introduced. Section 4.4 examines the lateral dimension of the computational domain that will allow for the capture of the instabilities associated with the propagating wave. The spanwise structured of the flow is also examined, along with a characterization of the lateral instability and the evolution of the wave properties in 3D (i.e. amplitude, propagation speed, half-width, APE, and KE). Section 4.5 discusses the role of the background current in the ISW energetics and length scale of the convective overturn, which can ultimately be used to understand the turbulent enhancement within the subsurface recirculating core. Concluding remarks and suggested future work are included in Chapter 5.

4.2 Methodology

4.2.1 Problem Geometry

Figure 4.2(a) shows a diagram of the shoaling problem, along with an ISW, in three-dimensions, and Figure 4.2(b) shows the ISW over a flat surface, along with its properties: amplitude, A_i, half-width, L_w, and a propagation speed, c. The wave propagates over a domain that has a length, L_x, a depth, H, and width, L_y. In both 4.2(a) and 4.2(b), the coordinate system is placed at the free-surface,

where $H = 0$. The along-wave, streamwise, direction is positive towards the shallower water depth; it is also denoted as the horizontal x-direction. Similar to the study of Chapter 3, the ISW propagates towards positive x, and this configuration is opposite to that used in *RCL2014*. The vertical, depthwise, direction is negative towards the bottom. Since the water depth changes in the the along-wave direction, $H \rightarrow H(x)$. In the lateral, or spanwise, direction, positive y is into the page. If the simulation is two-dimensional, no spanwise direction is used.

In Figure 4.2(b), the amplitude is defined as the maximum isopycnal displacement, from the reference state. The half-width is the integral of this displacement, along the wave-propagation direction [90], and the propagation speed corresponds to the translation of the wave trough, or the downward displacement of the pycnocline. The profile of the steady background density, $\rho_o + \rho(z)$, along with the steady background current, $U(z)$, is also included in 4.2(b).

The initial water column properties are those originally discussed in Chapter 3.2, with the pycnocline depth at z_o = -22m and the reference density ρ_o = 1026.58 kgm^{-3}. These properties were obtained from the deployed moorings used in *RCL2014*, which consisted of a subsurface mooring, at Lat. 21.07^o N, Lon. 117.27^o E and a surface mooring, at Lat. 21.07^o N, Lon. 117.22^o E; the moorings were approximately 6km apart and covered the region of the steepest slope in the SCS bathymetric transect. Here, the ISWs were observed to be convectively unstable and contain a subsurface recirculating core. Figure 3.1 of Chapter 3.2.1 shows the SCS bathymetric transect along with the mooring locations.

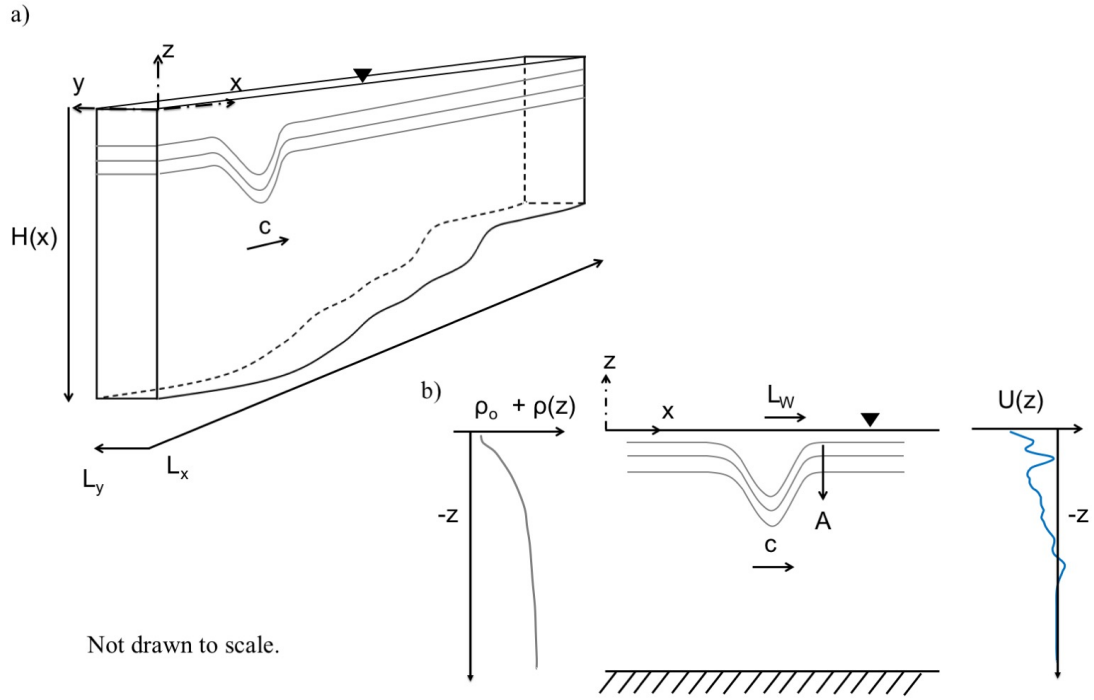

Figure 4.2: Schematic of the shoaling problem for an internal solitary wave of depression. The three-dimensional transect is presented in (a) along with initial wave and its properties in (b). The wave properties are: half-width , L_w, amplitude, A, and propagation speed, c. The reference datum is placed at the free surface. The transect has a streamwise length, L_x, a width, L_y, and a variable depth, $H(x)$; it is taken to be constant in the spanwise, y, direction (i.e. no lateral variations). In (b), the time-averaged background density profile, $\rho_o + \rho(z)$, is denoted as the grey-solid line, while the time-averaged velocity profile, $U(z)$, is given as the solid-blue line.

4.2.2 Governing Equations

The governing equations for the present study are the three-dimensional incompressible Navier-Stokes Equations under the Boussinesq Approximation (INSB) [92]. These are formulated in a Cartesian coordinate system. As such, akin to Chapter 3.2.3, the SCS bathymetric transect data from *RCL2014* is converted from Lat./Lon. to Universal Transverse Mercator (UTM), where the Cartesian framework is valid. More information on the conversion and corresponding

UTM Coordinates can be found in Chapter 3.2.1.

Prior to initializing the flow solver, the velocity field, in the along-wave propagation direction, is decomposed into a perturbation, $u'(x,y,z,t)$, and a steady background field, $U(z)$; $v'(x,y,z,t)$ and $w'(x,y,z,t)$ are used to describe the full lateral and vertical velocity. Per the Boussinesq approximation, the density field is decomposed into a reference, ρ_o, a background, $\overline{\rho}(z)$, and a perturbation field, $\rho'(x,y,z,t)$.

The conservation of mass, in vector form, is given as,

$$\nabla \cdot \mathbf{u} = 0, \tag{4.4}$$

where $\mathbf{u}$ is the three-dimensional velocity field (i.e. $\mathbf{u} = (u' + U, v', w')$). The momentum equations are

$$\frac{\partial u'}{\partial t} + u'\frac{\partial u'}{\partial x} + v'\frac{\partial u'}{\partial y} + w'\frac{\partial u'}{\partial z} = -\frac{1}{\rho_o}\frac{\partial p'}{\partial x} - U\frac{\partial u'}{\partial x} - w'\frac{\partial U}{\partial z} + \nu\nabla^2 u', \tag{4.5}$$

in the along-wave, x, direction,

$$\frac{\partial v'}{\partial t} + u'\frac{\partial v'}{\partial x} + v'\frac{\partial v'}{\partial y} + w'\frac{\partial v'}{\partial z} = -\frac{1}{\rho_o}\frac{\partial p'}{\partial y} - U\frac{\partial v'}{\partial x} + \nu\nabla^2 v', \tag{4.6}$$

in the lateral, y, direction, and

$$\frac{\partial w'}{\partial t} + u'\frac{\partial w'}{\partial x} + v'\frac{\partial w'}{\partial y} + w'\frac{\partial w'}{\partial z} = -\frac{1}{\rho_o}\frac{\partial p'}{\partial z} - U\frac{\partial w'}{\partial x} + \nu\nabla^2 w' - \frac{\rho'\mathbf{g}}{\rho_o}, \tag{4.7}$$

in the vertical, z, direction. Here $p'(x, y, z, t)$ is the perturbation pressure with respect to the reference background state, t is time, ν is the kinematic viscosity, and $\mathbf{g}$ is the gravitational acceleration direction. Rotation is neglected. The effect of changing water depth dominates over rotational forces [99]. However, over constant water depth rotation results in radiation of long inertia-gravity waves, which gradually decrease the ISW in amplitude [68, 99].

The density perturbation equation equation is

$$\frac{\partial \rho'}{\partial t} + \nabla \cdot [\mathbf{u}\,(\rho' + \overline{\rho}(z))] = \kappa \nabla^2 \rho', \tag{4.8}$$

where κ is the mass diffusivity. In Equation (4.5) to (4.8), the diffusion of the background profile is neglected. Lastly, following the Boussinesq Approximation, the reference pressure, $\overline{p}(x, z)$, is in hydrostatic balance with the background field in the absence of any wave propagation:

$$\frac{\partial \overline{p}}{\partial z} = -\left(\rho_o + \overline{\rho}\right) g. \tag{4.9}$$

4.2.3 Simulation Description

Equation (4.4) to Equation (4.8) are solved numerically via the three-dimensional deformed-domain variant of the spectral multidomain penalty method (SMPM) [80]; it is collocation-based in the x and z direction and equidistant in the y direction. A local Legendre-polynomial expansion is used to approximate the solution at each node of a Gauss-Lobatto-Legendre (GLL) grid in each element [91]. The velocity and density fields are expanded with a Fourier

Basis in the lateral. Time-integration is achieved via a Stiffly-Stable Third order scheme [84].

The boundary conditions, used to solve Equation (4.5) to Equation (4.8) of the SCS shoaling problem, are specified as free-slip/no-flux at all four physical boundaries and periodic in the lateral direction. In addition, at the left and right boundaries (i.e. $x = 0$ and $z = 0$), an artificial Rayleigh-type damper, one ISW half-width thick, is applied to eliminate any possible reflection from the incoming ISW [1]. For Equation (4.8), no-flux boundary conditions are implemented in all four physical boundaries, along with the Rayleigh-type damper at the left and right boundary, and periodicity in the lateral direction. Lastly, an exponential spectral filtering technique is applied in all directions to dissipate any numerical instabilities.

Similar to Chapter 3.2.5, the initial conditions, representing the ISW, are obtained from the Dubreil-Jacotin-Long (DJL) Equation (i.e. Equation (A.1) to Equation (A.6)) [106, 179], solved via a spectral technique [52]. The obtained solution corresponds to an ISW that propagates over a flat bottom, with the water column properties observed by *RCL2014* and discussed in Chapter 3.2.2. Such wave has an initial amplitude of $A_i = 143$m, a half-width of $L_{w,i} = 1014$m, and a propagation speed of $c_i = 1.9258\text{ms}^{-1}$.

Initializing the SCS Shoaling Simulation

The present study encompasses two parts: a two-dimensional simulation of the shoaling ISW over gentle slopes and a three-dimensional restart once the ISW is noted to be unstable. The restart is performed shortly before the instabil-

ity arises. Afterwards, the ISW is then allowed to become unstable in three-dimensions. The computational domain used for both the 2D and 3D study is the same as that originally discussed in Chapter 3.2.5. The solution of the DJL Equation is placed over a flat bottom, where the ISW is allowed to propagate without artificially inducing shoaling.

To numerically solve Equation (4.4) through Equation (4.8) with the SMPM flow solver, the computational domain is partitioned into m_x subdomains in the horizontal and m_z subdomains in the vertical direction, with n points per subdomain in each direction. The degree of the polynomial used to approximate the solution inside each element is $p = n - 1$. In the lateral direction, the number of points is denoted as m_y. The total number of degrees of freedom is defined as: $n^2 m_x m_z m_y$.

The number of subdomains in the horizontal is set to $m_x = 1600$; this value is twice as that used in Chapter 3. Such increase is justified in anticipation of smaller scale structure development, consequence of the three-dimensional breaking. The maximum grid spacing, for the GLL grid, is now approximately $\Delta x = 6$m; this value is less than the length of observed KH-type instabilities in the field [125]. The convective breaking is better resolved, along with the flow inside the subsurface recirculating core. The number of subdomains in the vertical remains unchanged, such that $m_z = 25$. It is assumed that the vertical resolution previously used is adequate. Lastly, the number of points per subdomain is also kept fixed, a $n = 15$. Note that it is not known *a priori* if the assumed resolution is sufficient.

Similar to the previous study of Chapter 3, the computational domain is partitioned into overlapping windows of approximately $m_x = 128$ elements, that

Table 4.1: Computational Parameters for the 2D simulations presented in this study. The regions included are: Location I, the subsurface, and surface mooring location. Note that the Gauss-Lobatto-Legendre (GLL) grid is non-uniform locally in each element. The total number of gridpoints in the lateral direction is $m_y = 1$.

Parameter	Value	**Parameter**	Value
$\Delta\mathbf{x_{min}}$	1.120m	$\Delta\mathbf{x_{max}}$	6.619m
$\Delta\mathbf{z_{min,I}}$	0.640m	$\Delta\mathbf{z_{max,I}}$	3.967m
$\Delta\mathbf{z_{min,sub}}$	0.314m	$\Delta\mathbf{z_{max,sub}}$	2.254m
$\Delta\mathbf{z_{min,sur}}$	0.296m	$\Delta\mathbf{z_{max,sur}}$	1.838m
$\mathbf{m_x}$	1600	$\mathbf{m_z}$	25
$\mathbf{n}$	15	$\Delta\mathbf{t}$	0.2s

track the ISW as it shoals; this approach reduces the computational time per timestep. The window size is approximately $16L_{w,i}$ with an overlapping length of approximately $6L_{w,i}$ to $7L_{w,i}$, depending on the ISW location and propagation speed along the transect. Table 4.1 shows the properties of the computational grid employed in this study. The timestep size, Δt, is specified so as to respect the CFL limit for the initial velocity scale and the grid properties; the limit is set to 0.50 for both the x and z direction. During the shoaling simulation, an adaptive timestepping method ensures that Δt is adjusted, if necessary; timestep adjustement would result from a change in the wave velocity scales or due to the small-scale features of the subsurface recirculating core. Nevertheless, it is not known *a priori* if a timestep adjustment is necessary.

Figure 4.3 shows the isopycnals at Location I, along with the SMPM grid superimposed in gray. With the increase in horizontal resolution, there are approximately 120 points per ISW wavelength and 60 points per maximum isopycnal displacement. Across the transect, the vertical grid spacing decreases with decreasing water depth, as noted in Table 4.1.

The parallelization scheme of the flow solver is based on a Message Passing

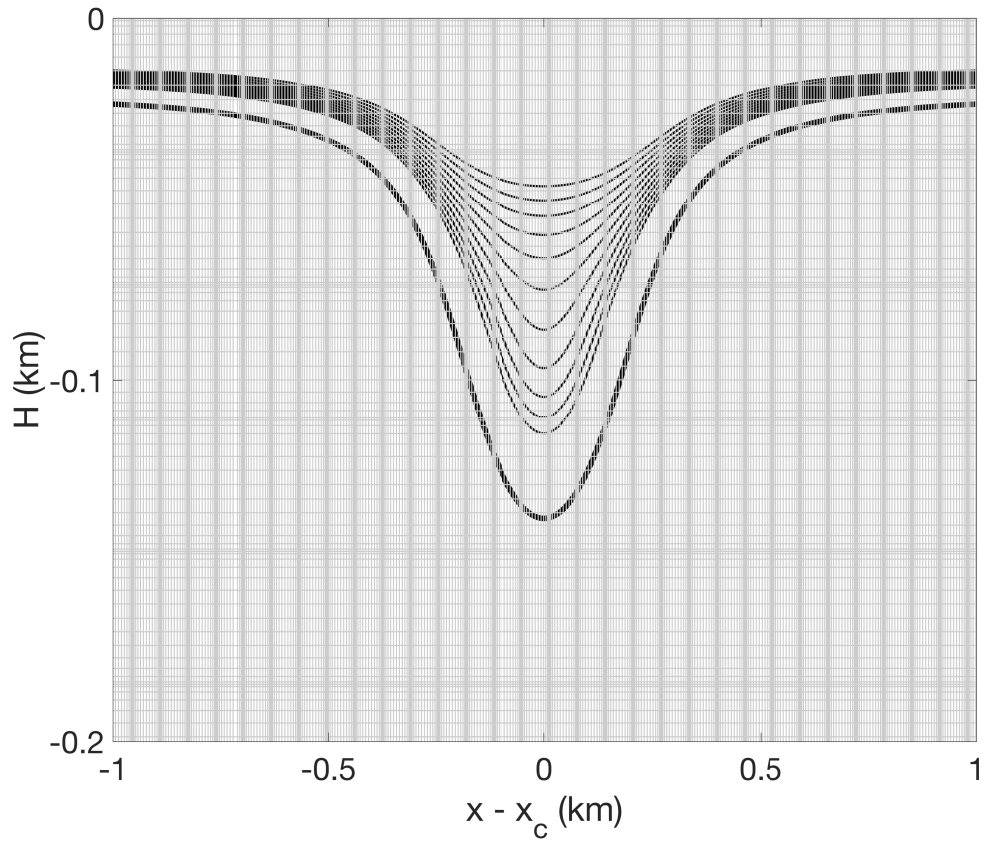

Figure 4.3: Internal Solitary Wave (ISW) at Location I with the superimposed GLL Grid (gray). The range has been shifted with the trough location, x_c. Eleven isopycnals are shown, along with the pycnocline (thicker solid-black line). The ISW field is obtained from the solution of the DJL Equation Solver [52]. The position of the ISW has been shifted by a distance of $x_c = 10H_i$.

Interface (MPI) implementation. The SMPM computational domain is partitioned in the along-wave x-direction, such that each processor solves a problem with size $n^2 m_z (m_x/nprocs)$, where $nprocs$ is the number of processors. The maximum number of processors, that can be used at any given time with the SMPM flow solver, is equal to m_x. For a 2D simulation, by increasing the number of subdomains in the horizontal there is an increase in wall-clock time, but no increase in memory requirement and the computational time per timestep is the same as that of Chapter 3. Once the simulation is restarted in 3D, then the mem-

ory requirement and the computational time per timestep increases.

With regards to the choice of resolution in the vertical, the most expensive part of the SMPM flow solver is computing the solution of the Pressure Poisson Equation (PPE), which is based on a Schur Factorization of the Poisson matrix that scales as $n^2 m_z$ in 2D [80] and $n^2 m_z m_y$ in 3D. Any increase in either n or m_z results in a significant increase in the memory cost which ultimately leads to an increase in computational time. Thus, increasing the vertical resolution or the degree of the polynomial used to approximate the solution in each element must be justified.

Migrating from 2D to 3D

To migrate the 2D grid to 3D, a domain extrusion is applied, where the x-z grid is repeated m_y times. No lateral changes to the SCS bathymetric transect are imposed because the observed ISWs propagated along the same latitude, in the normal-to-isobath direction [103]. Subsequently, when the simulation is restarted in 3D, prior to the ISW becoming unstable in 2D, the fields are perturbed to ensure that the breaking process becomes three-dimensional. The perturbed density, ρ'^*, horizontal velocity, u^*, and vertical velocity, w'^*, are defined as,

$$\rho'^*(x, y, z) = (1 + \alpha R)\, \rho'(x, z), \tag{4.10}$$

$$u'^*(x, y, z) = (1 + \alpha R)\, u'(x, z), \tag{4.11}$$

and

$$w'^{*}(x, y, z) = (1 + \alpha R)\, w'(x, z) \tag{4.12}$$

where α is the noise amplitude, chosen to be 10^{-3}, and R is a uniformly distributed random number ranging from -1 to 1 [55]. No perturbation is introduced in the v' velocity. The perturbed fields are then set as the initial condition for the three-dimensional restart.

In the three-dimensional study, the choice of m_y, and the lateral width, are not known *a priori*. Therefore, one of the objectives of the present work is to determine the required values to accurately capture the unstable shoaling ISW. The choice of lateral domain is nontrivial. Studies of breaking interfacial waves suggest a lateral width between 1/2 to 2 times the water column depth [55, 12].

At the location of the moorings, where a subsurface recirculating core exists, the water depth can be used as the reference length scale to determine the lateral width. According to *RCL2014*, the subsurface mooring recorded data up to a depth of 450m. With this length scale, the ISW shoaling simulation can be performed using selected values of L_y. Four simulations with varying lateral width are performed, where the ISW is allowed to propagate until the location of the subsurface mooring; here, the differences between each L_y-based solution can be studied visually, to determine any possible changes. The selected L_y values are: 25.7m, 67.5m, 100m, and 135m; these values correspond to a fraction of the 450m water depth. The number of gridpoints in the transverse is initially set to $m_y = 32$.

Once the lateral width is chosen, the ISW shoaling process is simulated with the obtained L_y and an increased lateral resolution of $m_y = 64$. The increment

allows for more Fourier modes to not be filtered. The exponential filter order in the transverse is kept fixed at a value of 11, equal to that in the x-z domain. It may be possible that 32 points or 64 points in the transverse is not an adequate resolution to capture the lateral evolution of the ISW. Lastly, the timestep size is initially set to 0.2s, with the adaptive ensuring that the CFL limit is not violated; these are limits are fixed at 0.5 in x and z and at 0.25 in y.

4.3 Characterizing the instability in a two-dimensional shoaling ISW over the SCS bathymetric transect

4.3.1 Properties of the two-dimensional ISW propagating over the SCS transect

The two-dimensional shoaling ISW is performed until the wave reaches the location of the surface mooring, at a distance of approximately 60km from the start of the SCS bathymetric transect. As the wave propagates, its properties are computed using the same approach as Chapter 3.3.1. Figure 4.4 shows the computed propagation speed, maximum ISW-horizontal velocity, amplitude and half-width. In the presence of a convective overturn, where there is a heavy-over-light fluid configuration, the density field is first adiabatically sorted, then the amplitude is computed. The density rearrangement is accomplished via a probability density function of the density perturbation profile [189, 178], using a parallel sorting algorithm [154].

Figure 4.4(a) corresponds to the wave velocity scales: U_{max} and c. At approx-

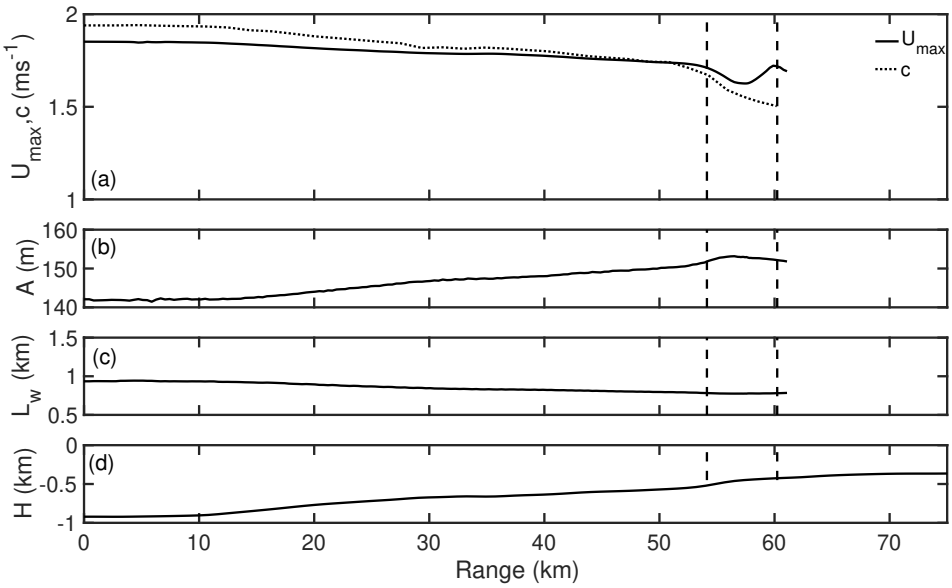

Figure 4.4: Computed properties of the shoaling ISW along the SCS transect. The simulation was stopped once the ISW reached the location of the surface mooring at approximately 60km. The included properties are: (a) wave propagation speed, c, and maximum horizontal velocity, U_{max}, (b) amplitude, A, and (c) half-width, L_w. The SCS transect is presented in (d) for reference. The black-dashed line corresponds to the location of the surface and subsurface moorings deployed by *RCL2014*.

imately 50 km from the start of the transect, the propagation speed decreases below U_{max}, leading to convective breaking; this is approximately at the same distance as shown previously in Figure 3.7, for the coarsely resolved simulations. Figure 4.4(b) and 4.4(c) show the ISW amplitude and half-width, along the SCS bathymetric transect; the transect is included in 4.4(d) for reference. As the ISW shoals, the amplitude increases and the half-width decreases. In the context of two-dimensional shoaling over gently varying bathymetry, an increase in amplitude leads to a decrease in propagation speed [162] and this process is captured by the present simulation.

4.3.2 Examining the primary two-dimensional instability

To examine the possibility of shear instabilities, the Richardson Number is computed using Equation (4.1); the result is shown in Figure 4.5. Any Ri value that is above the critical threshold of Ri = 1/4 [119], or below 0, is removed; values above this threshold correspond to strongly stratified regions, where there is no shear present, while values below 0 indicate an overturn, where there is a heavier-over-light fluid configuration. The overturn is an indication of a convective instability.

Figure 4.5 also shows the first isopycnal undergoing convective breaking as the red-solid line; its value is found to be $\rho_c = 1022.26\ kgm^{-3}$. The black-solid line is the pycnocline, where the density value is the reference ρ_o. The value of Ri at the trough of the ISW is approximately 0.15, but at the convectively breaking location, where ρ_c is overturning, Ri is below 0.10; here is where shear instabilities could be present [14, 29]. It may be conjectured that, for the background field conditions used in the present study, the convective instability seems to precede any possible shear instability.

At the ISW trough, the length of the region where $Ri < 1/4$, defined as l_u, is approximately 400m. The ISW half-width is shown as L_w; at the subsurface mooring its value is approximately 781m. When the ratio of l_u/L_w is computed its value is 0.511 which is not larger than 0.86 [56]. Thus, no roll-up motion akin to KH-type billows is expected at the pycnocline. Alternatively, the size of the region, where shear is significant, is not large enough for the instability to develop.

To further verify the possible presence KH-type instabilities, which are char-

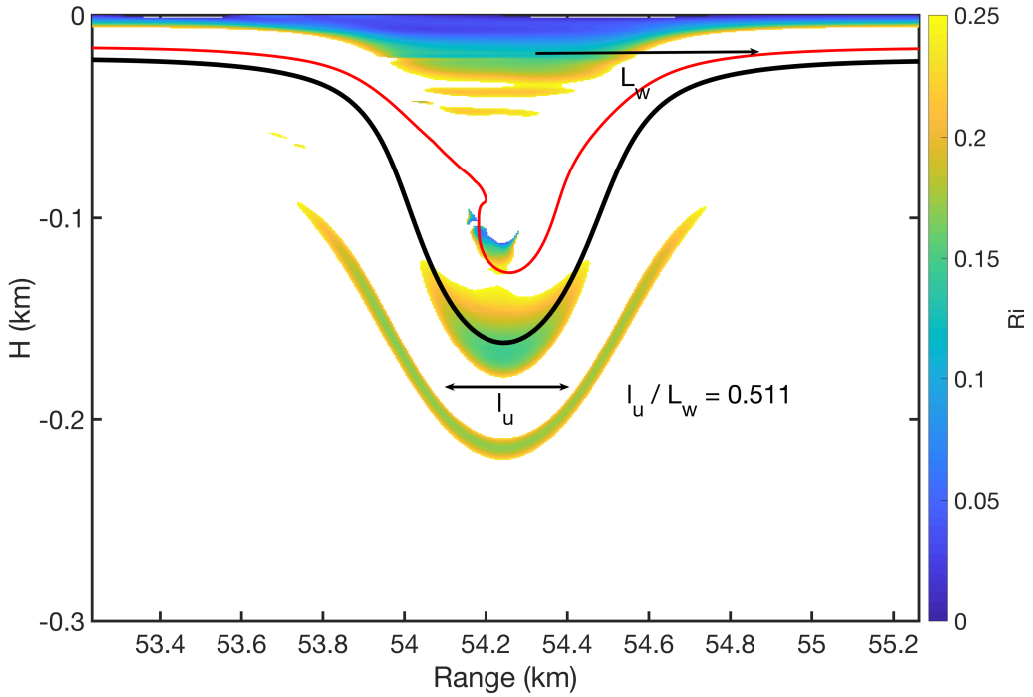

Figure 4.5: Richardson number, as defined in Equation (4.1) at the subsurface mooring location for the SCS shoaling simulation. Only the range $0 < \text{Ri} < 1/4$ is included; values above $1/4$ are regarded as strongly stratified and values below 0 are associatd with an overturn, where there is a heavy-over-light fluid configuration. The isopycnal corresponding to the reference density, $\rho_o = 1022.58\ \text{kgm}^{-3}$ is denoted as the black-solid line while the isopycnal undergoing convective overturning, with a value of $\rho_c = 1022.26\ \text{kgm}^{-3}$ is shown as the red-solid line. The length of the region, below the trough, where $Ri < 0$, is denoted as l_u. Here the minimum Ri is obtained to be 0.16. The half-width of the ISW is included as L_w. The ratio l_u/L_w can be used as an indicator of the possibility of shear-instabilities [56]. At the subsurface mooring location, this ratio has an approximate value of 0.511.

acterized by coherent vortical motion, the vorticity in the lateral direction, ω_y, is computed at the subsurface mooring location. The lateral vorticity is defined as,

$$\omega_y = -\left(\frac{\partial w'}{\partial x} - \frac{\partial u}{\partial z}\right), \tag{4.13}$$

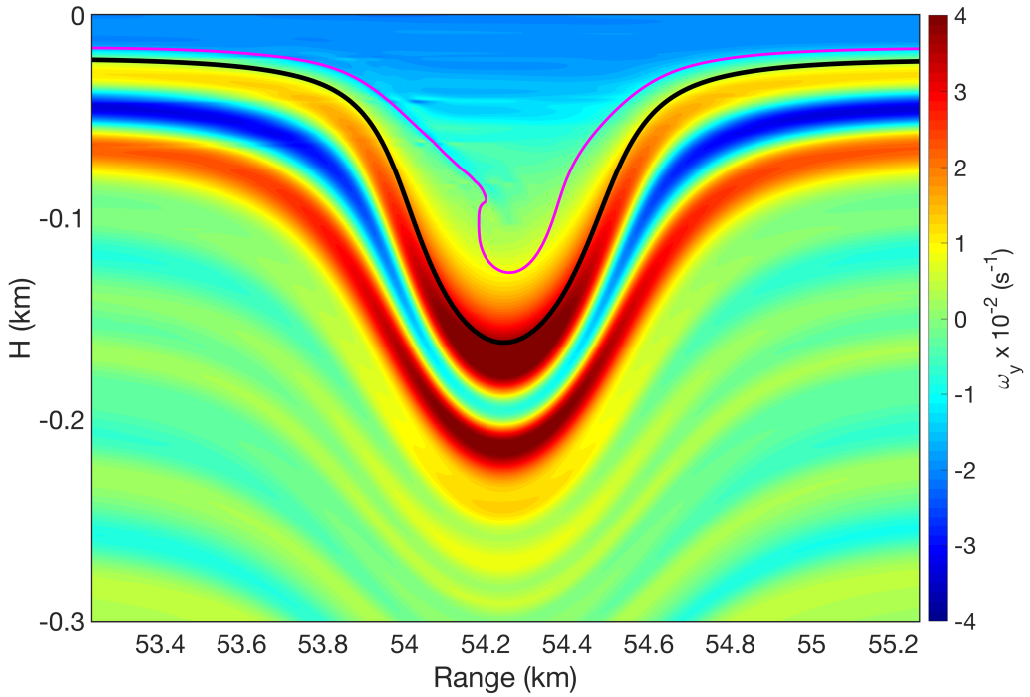

Figure 4.6: Lateral vorticity, ω_y, at the subsurface mooring location. The isopycnal experiencing convective overturning first, ρ_c, is included as the magenta-solid line; it has a value of approximately 1022.26kgm^{-3}. The pycnocline is included as the black-solid line.

where $u = u' + U$. If the KH-type shear instabilities are present, they can manifest as lobes of ω_y. The lateral vorticity is shown in Figure 4.6, along with the ρ_c isopycnal as the magenta-solid line, and the pycnocline as the solid-black line. No indication of coherent vortical motion is near the pycnocline.

According to *RCL2014*, when the ISW reaches the surface mooring location, a subsurface recirculating core has already formed. The Shipboard ADCP and CTD measurements have also suggested the presence of shear instabilities close to the core of the ISW. Figure 4.7 shows the computed Richardson number within the range $0 < \text{Ri} < 1/4$, at the surface mooring location. The isopycnal that first exhibited convective breaking, ρ_c, is shown as the red-solid line; the pynocline is shown as the black-solid line.

With fluid further being displaced above the trough, the Richardson number decreases below the critical value of 0.10 and at some instant becomes negative (not shown), indicating the presence of overturn. The smallest Ri are located close to the core of the wave, that is surrounded by ρ_c. Thus, the convective breaking, originally noted at the surface mooring location, may create favorable conditions for shear instabilities, although near the core. The possibility of shear instabilities closer to the region where the subsurface recirculating core exists was also reported by *RCL2014*. Near the ISW trough, the length of the region where Ri $< 1/4$ is 500m; the half-width is found to be $L_w = 780$m. Thus, the value of l_u/L_w is 0.640. Under length scales, no shear instabilities are expected at the pycnocline [56].

The lateral vorticity, ω_y, is computed at the surface mooring location and shown in Figure 4.8; the ρ_c isopycnal is included as the magenta-solid line, along with the pycnocline, as the black-solid line. No coherent vortical motion, characteristic o KH-type instabilities, exists near the pycnocline. Thus, it is believed that the dominant instability in the shoaling ISW, for the given background current and density profile, is convective and not shear.

Lastly, from Figure 4.8, the prexisting background shear, or background vorticity, appears to be intruding from the near-surface region into the wave, just above the trough. As the negative vorticity penetrates, positive vorticity, near the pycnocline, is dislodged and pulled into the trough. Because subsurface recirculating cores are characterized by two-counterotating regions [102], this intrusion of negative and positive vorticity may be used to highlight the importance of the background current in the formation of a subsurface recirculating core [67].

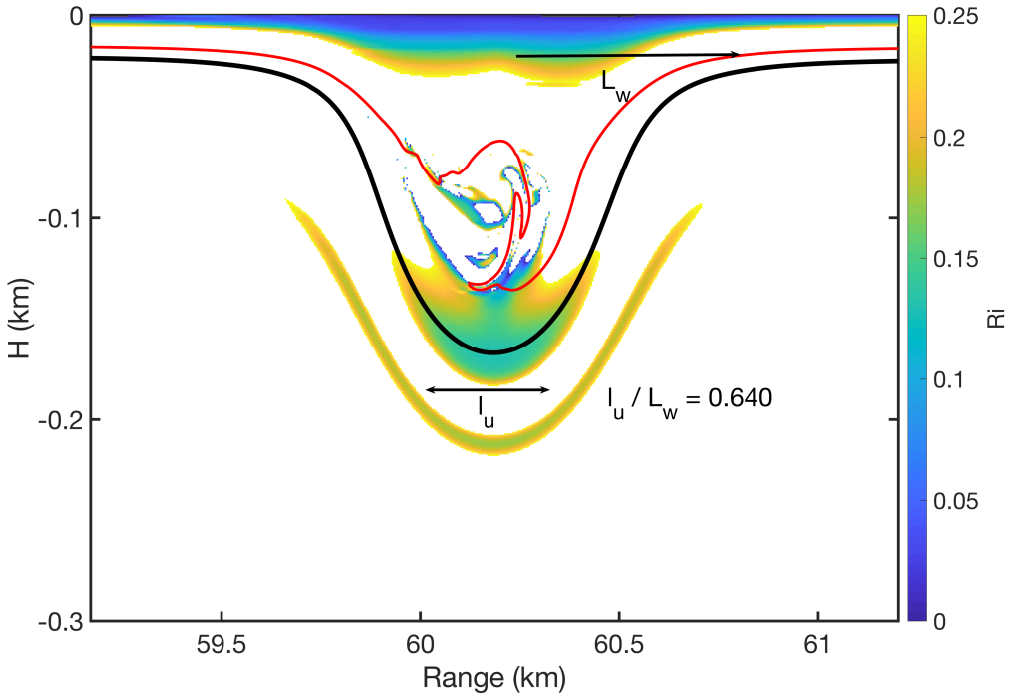

Figure 4.7: Richardson number, as defined in Equation (4.1) at the surface mooring location for the SCS shoaling simulation. Only the range $0 < \text{Ri} < 1/4$ is included; values above 1/4 are regarded as strongly stratified and values below 0 are associated with an overturn, where there is a heavy-over-light fluid configuration. The pycnocline is denoted as the black-solid line and the isopycnal the first exhibited convective breaking, ρ_c, is shown as the red-solid line. The length of the region, below the trough, where $Ri < 0$, is denoted as l_u. Here the minimum Ri was simulated to be 0.15. The half-width of the ISW is included as L_w. The ratio l_u/L_w can be used as an indicator of the possibility of shear-instabilities [56]. At the surface mooring location, this ratio has an approximate value of 0.64.

4.3.3 Examining the energetics of the shoaling ISW over the SCS bathymetric transect in two-dimensions

In addition to the velocity and length scales, the ISW may also be characterized by its distinct Kinetic Energy (KE) and Available Potential Energy (APE). The APE is defined as the minimum energy required to adiabatically bring a displaced fluid parcel back to its reference location [96, 189]. To obtain the APE,

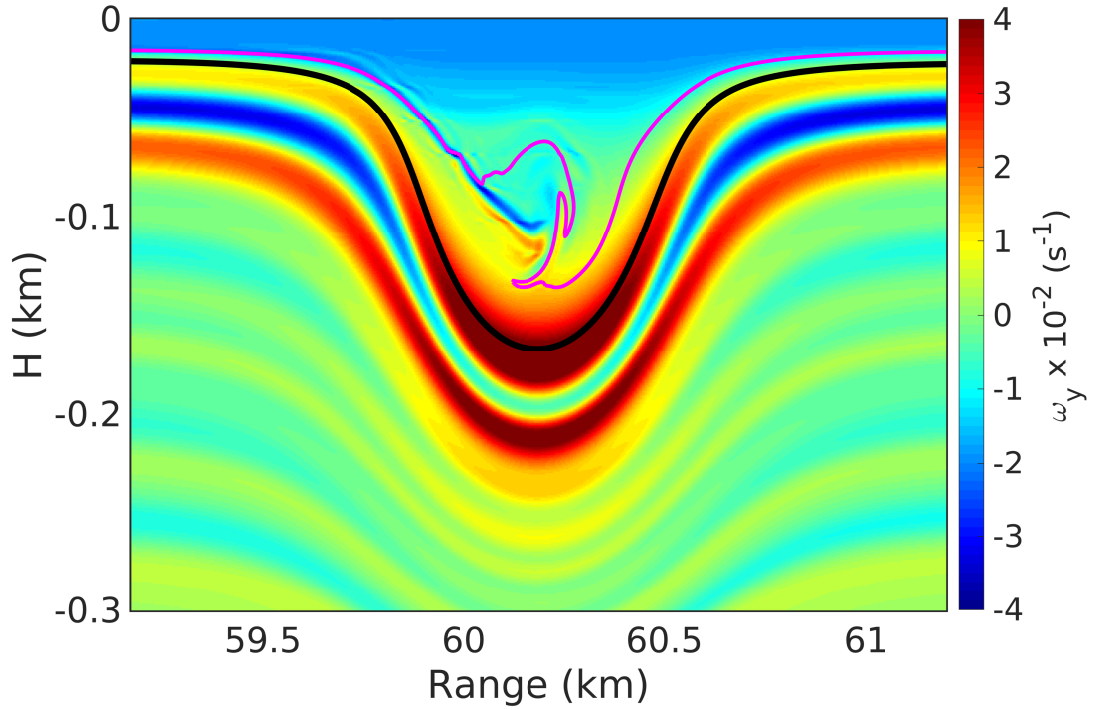

Figure 4.8: Lateral vorticity, ω_y, at the surface mooring location. The isopycnal that first exhibited convective breaking, ρ_c, is included as the magenta-solid line along with the pycnocline as the black-solid line.

the APE Density, E_a, is computed first, by integrating the density profile between the fluid parcel at its reference location and at its displaced location, in the vertical. The APE is then obtained by taking the volume integral of E_a.

However, in the presence of a convective overturn, the density is adiabatically sorted, into a stable configuration, such that it is monotonically increasing [189, 178, 154]. Assuming that the background density is invertible, with inverse $\bar{z}_r(\rho)$, that satisfies the relation $\eta(x,z,t) = \bar{z}_r(\rho(x,z,t))$, where η is the isopycnal displacement, E_a can then be obtained by integrating across the difference between the fluid parcel height at the reference background density profile, and the adiabatically rearranged density profile associated with the wave-driven disturbance, $\bar{z}_r(\rho)$ [96].The APE Density, E_a, is then[123, 124, 96, 98]

$$E_a(x,z,t) = g \int_{\overline{\rho}(z)}^{\rho(x,z,t)} (z - \overline{z}_r(r'))\, dr'. \tag{4.14}$$

The APE is the volume integral of E_a (e.g. in 2D, APE = $\int\int E_a dz dx$). The ISW Kinetic Energy (KE) is the volume-integral of the KE Density, E_k, defined as [98],

$$E_k(x,z,t) = \frac{\rho_o}{2}\left(u^2(x,z,t) + w^2(x,z,t)\right), \tag{4.15}$$

where $u = u'(x,z,t)$ and $w = w'(x,z,t)$; these velocity fields are the wave-induced horizontal and vertical velocity, respectively; no background current is included in the computation of the wave KE.

Figure 4.9 shows the KE and APE for the shoaling ISW. In 4.9(a), the KE and APE evolution are shown; in 4.9(b), the KE and APE relative change are shown, based on their respective energy value, E_i, at the start of the SCS bathymetric transect, which is included for reference in 4.9(c). The initial ISW KE and APE value are 252MJm^{-1} and 198 MJm^{-1}, respectively. The location of the subsurface and surface mooring is denoted as the black-dashed lines in 4.9(a) through 4.9(c).

From Figure 4.9, the APE is increasing as the wave shoals. The increase in APE is consistent with the increase in amplitude and the decrease in propagation speed, shown in Figure 4.4; the wave is adjusting to the changes in water depth. Because the SCS bathymetric slope is regarded as gentle, the ISW is thought to shoal without losing significant energy [162]. Such a process is also referred to as adiabatic shoaling [48, 62, 184, 99].

Conservation of energy dictates that, as the APE increases, the KE should be

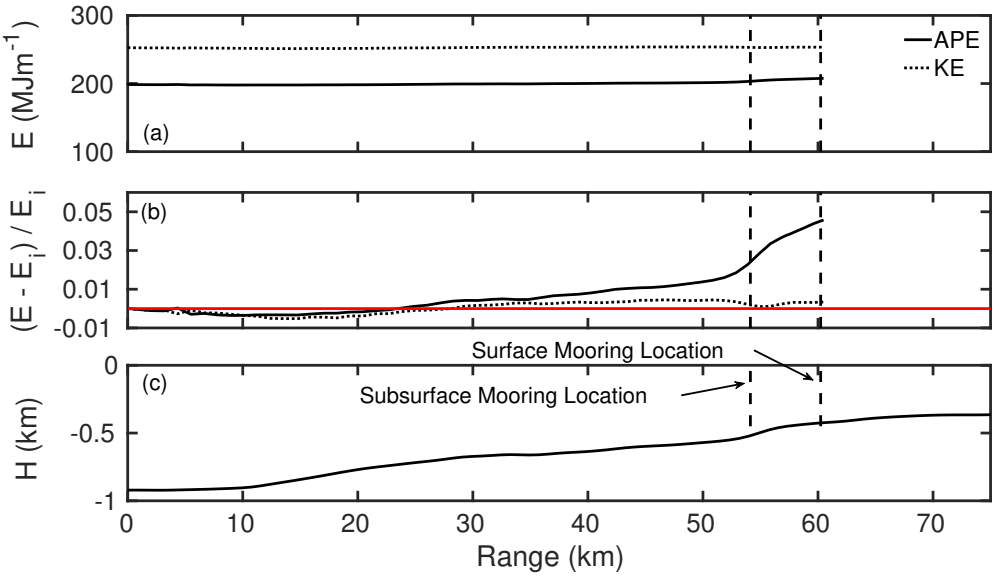

Figure 4.9: Evolution of the Kinetic Energy (KE) and Available Potential Energy (APE) for the shoaling ISW. In (a), KE and APE are computed from intgrating Equation (4.15) and Equation (4.14), respectively. In (b), relative difference for the APE and the KE with respect to their initial value is computed and shown; the red-solid line corresponds to the 0 value. In (c), the SCS bathymetric transect is included for reference.

decreasing [98]. Nevertheless, Figure 4.9(a) and 4.9(b) show that the KE remains relatively constant. To verify the computation of the APE and KE, a second simulation was performed for a shoaling ISW, *without* any background current, U(z), but with a DJL Solution that had the same initial wave amplitude of A_i = 143m; this special shoaling simulation had a reduced number of subdomains, in the along-wave direction, of m_x = 800. The ISW propagated until the end of the SCS bathymetric transect.

Figure 4.10 shows the KE and APE of the propagating ISW *without* the presence of a background current. In 4.10(a), the evolution APE and KE are shown. In 4.10(b), the relative difference, for the APE and KE, is shown along the SCS bathymetric transect, which is included in 4.10(c) for reference. The location of

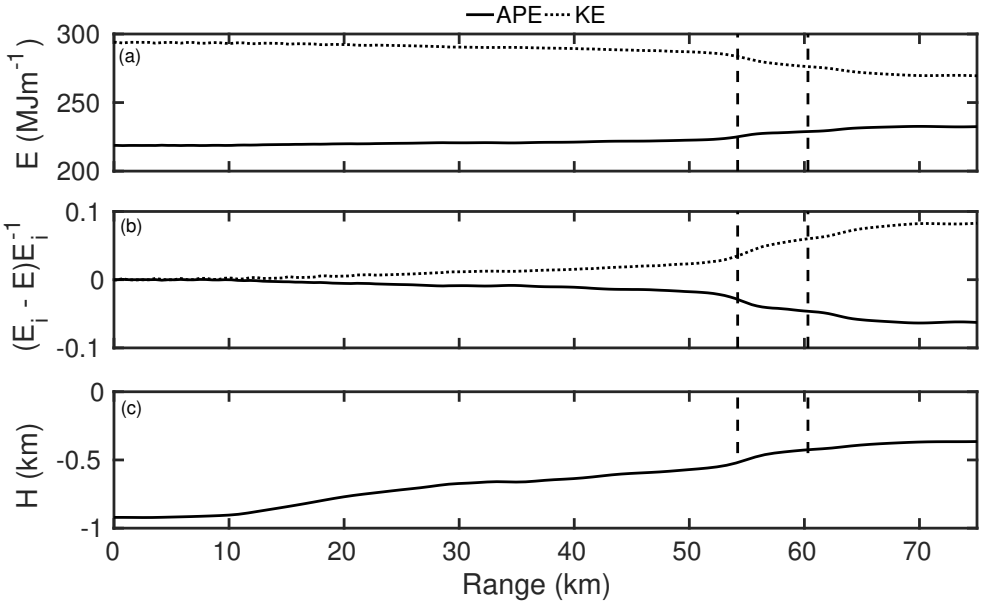

Figure 4.10: Evolution of the Kinetic Energy (KE) and Available Potential Energy (APE) for the shoaling ISW *without the presence of a background current*, $U(z)$. In (a), KE and APE are computed from integrating Equation (4.15) and Equation (4.14), respectively. In (b), relative difference for the APE and the KE with respect to their initial value is computed and shown; the red-solid line corresponds to the 0 value. In (c), the SCS bathymetric transect is included for reference.

surface and subsurface mooring is denoted as the black-dashed lines in 4.10(a) through 4.10(c).

From Figure 4.10, the APE is increasing as the KE decreases. This phenomenon is consistent with conservation of energy, although the numerical scheme of the SMPM flow solver has as exponential filter active and finite viscosity value; both of these terms dissipate energy. Thus, there should be a net change in total energy as the ISW shoals. Nevertheless, the decrease in KE and increase in APE is consistent with a shoaling wave, without a background current [98].

According to the energy evolution in stratified flows, the interchange be-

tween KE and APE occurs through the buoyancy flux term, $\rho' w' g$ [175]; this term shows up in both the conservation of APE and conservation of KE [82]. The APE increases because of an increasing buoyancy flux, and an increase in this flux leads to a decrease of KE. This is the only active source of energy related to the ISW-induced density perturbation and velocity pertubation. However, under the presence of a background current, the background shear provides kinetic energy to the wave. As such, it may be conjectured that, in the present study, where the ISW shoals under the presence of a background current, the constant KE shown in Figure 4.9 is associated with the presence of $U(z)$, which could be supplying most of the energy converted to APE. Further analysis will be addressed in Section 4.5.

Lastly, Figure 4.9 also shows a KE value that is higher than the APE value, for any given position along the SCS bathymetric transect, yet *RCL2014* observed a higher APE than KE. ISWs are known to have a higher KE than APE [98]. Worthy of note is the approach used by *RCL2014* to compute the ISW energy. Here, the KE was computed by subtracting the background current's KE, averaged for 30 min prior to the wave arrival at the mooring locations. If the same approach is applied to the simulated data of the present study, shown in Figure 4.9, then the KE is lower than the APE, from the start of the simulation (not shown).

However, the KE from the simulated ISW may be obtained directly from the ISW-induced horizontal and vertical velocity, without the inclusion of the background current. This difference in definition may explain why the simulated KE value is higher than the APE, because using the horizontal velocity decomposition, $u = u' + U$, then $\frac{1}{2}\rho_o U^2 \neq \frac{1}{2}\rho_o (u' + U)^2$. Nevertheless, the difficulty in separating ISW-induced horizontal velocity from the background current, using

observed data, makes the KE computation nontrivial in the field. The method utilized by *RCL2014* is believed to be correct, yet the KE values would be different. Note that, from the equation describing the evolution of the KE [82], the KE may be regarded as the energy available for dissipation. As such, an overestimate/underestimate could have an impact on the energy budget of a shoaling ISW.

4.4 The formation of the three dimensional convective instability in a ISW shoaling over the SCS bathymetric transect

4.4.1 Restarting from two dimensions to three-dimensions

The first step, in simulating the shoaling of the ISW in 3D, is to specify the domain width, L_y. The process of determining L_y begins with a simulation coarsely resolved in the lateral direction, where m_y= 32 gridpoints are chosen, and the domain width is varied. The ISW is then allowed to propagate from the restart location to the subsurface mooring location, where it is already convectively unstable; here, the lateral structure of the solution is analyzed.

The objective, of this part of the study, is to find the minimum domain width that will not produce any discernible difference in the solution structure, in the context of the development of transverse structure. The values chosen for L_y are: 25.7m, 67.5m, 100m, and 135m. These are obtained by considering the maximum water depth that the subsurface mooring, in the field, captured (see *RCL2014*), and taking a fraction of this depth; this depth is noted as 450m. Ide-

ally, the lateral dimension should be associated with the length scale of interest of the problem, which may be the size of the observed overturn. However, for the field data corresponding to June 2, such scale is not known. Thus, a domain width convergence study based on the water depth is performed instead.

The three-dimensional simulation is restarted prior to the ISW becoming convectively unstable. It is assumed that the shoaling process is two-dimensional prior to convective breaking. Once the wave propagation speed decreases below the ISW-induced horizontal velocity, the breaking process should be three-dimensional [55].

From Figure 4.4, the location where $U_{max} > c$ occurs at approximately 50km into the SCS bathymetric transect. The shoaling simulation is then restarted prior to 50km. Figure 4.11 shows the location of the ISW prior to restart; it is approximately 20 km before the location of the subsurface mooring. The ISW-induced velocity and density field are slightly perturbed upon restart, to ensure that the three-dimensional breaking process occurs. It is assumed that, without any perturbation no 3D breaking will occur, as no self-excited 3D breaking mode has been reported in the literature for convectively unstable ISWs.

4.4.2 Visualizing the convectively breaking ISW

The shoaling ISW may be visualized from a single contour level, with value ρ_c = 1022.26 kgm^{-3}, as introduced in Section 4.3. This is the contour level that first becomes convectively unstable in 2D. Figure 4.12 shows the convectively unstable ISW at the subsurface mooring location with L_y = 25.7m and m_y = 32. In addition to the isosurface corresponding to ρ_c, a second isosurface associated

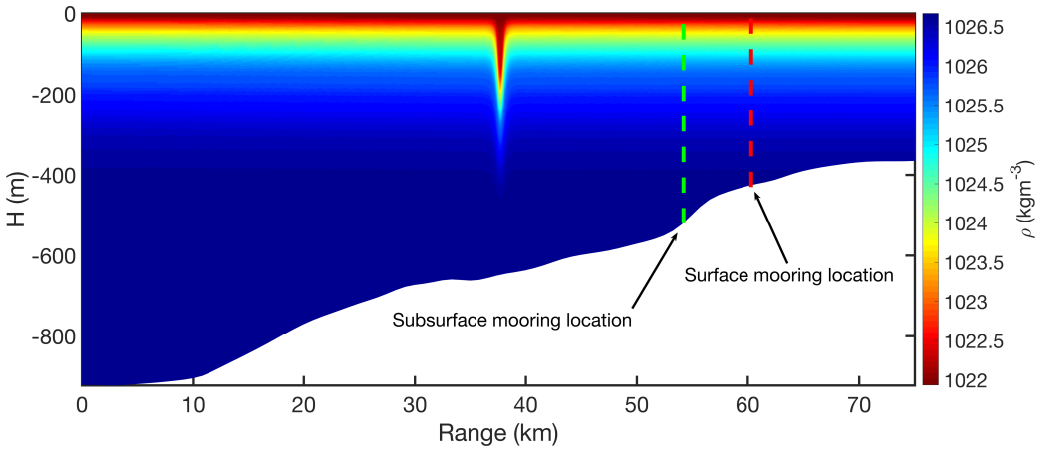

Figure 4.11: SCS bathymetric transect with the location of the wave-driven perturbation where the restart run in three dimensions occurs. The contour variable is the total density field, ρ, which includes the steady background density profile, $\overline{\rho}$, and the density perturbation ρ'. The locations of the subsurface and surface mooring are also included as the green-dashed and red-dashed lines, respectively. The SCS bathymetric transect with the background density profile is originally shown in Figure 3.3.

with the reference density, ρ_o, is also included as grey; this isosurface is the pycnocline. The wave is not drawn to scale, as its dimensions need to be adjusted so that it can be observed within the field of view of the visualization software. The along-wave direction is decreased by a factor of 10 and the lateral direction is increased by a factor of 2. The black-solid line arrow indicates the direction of wave propagation.

4.4.3 Establishing the lateral domain width

Changes in the simulated wave, along the lateral direction, are first reported through the vertical component of vorticity, ω_z, that is computed as,

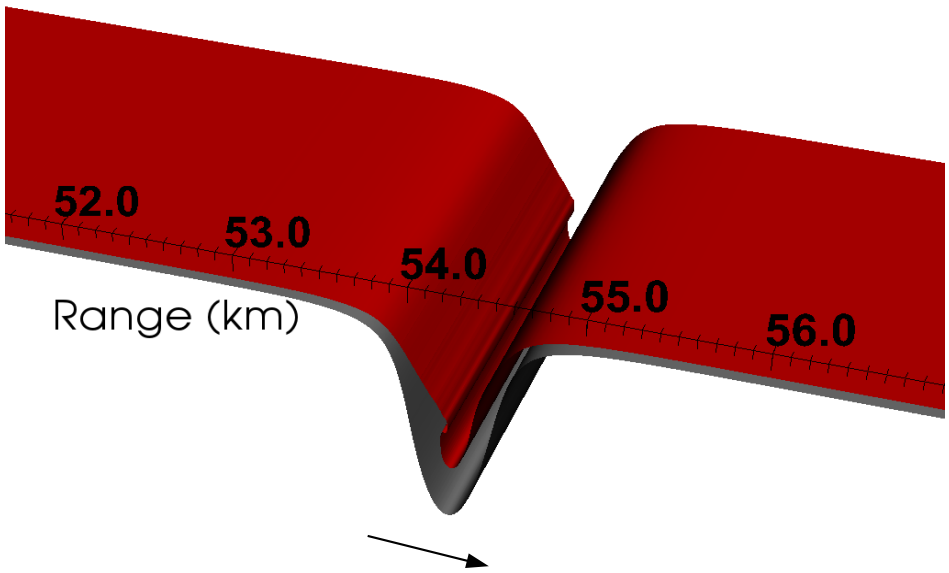

Figure 4.12: Isosurfaces of the convectively unstable ISW, shoaling over the SCS bathymetric transect, at the location of the subsurface mooring; this location is approximately 54.2km into the transet. Two isosurfaces, representing two isopycnal values, are shown: ρ_c = 1022.26 kgm^{-3} (red) and ρ_o = 1022.58 kgm^{-3} (grey). Note that the wave is not shown to scale. The domain is adjusted so that the ISW can be observed within the window size of the visualization software. The along-wave direction is decreased by a factor of 10 and the lateral direction by 2. The domain length is set to L_y = 25.7m with m_y = 32 gridpoints in the lateral.

$$\omega_z = \left(\frac{\partial v'}{\partial x} - \frac{\partial u'}{\partial y} \right) \hat{\mathbf{k}}. \tag{4.16}$$

This property indicates the presence of the spanwise instabilities, that originate from changes in the lateral velocity, v'; it can be visualized in the x-y plane, at a depth of $H = -100$m, where ρ_c exhibits convective breaking as previously shown in Figure 4.5 and Figure 4.6.

Figure 4.13 shows the ω_z contour with $m_y = 32$ gridpoints, for the various values of L_y. The isopycnal corresponding to ρ_c is included as the red-dashed line. In Figure 4.13(a), the domain length is $L_y = 25.7$m, $L_y = 67.5$m in 4.13(b), $L_y = 100$m in 4.13(c), and $L_y = 135$m in 4.13(d). The structure of the lateral instability varies from 4.13(a) to 4.13(c); the instability at 4.13(a) is first visualized as a positive and negative ω_z lobe, but as the value of L_y increases, the vertical vorticity field converges to six lobes: three positive and three negative.

The vertical vorticity lobes can be associated with a particular wavenumber, that corresponds to the most energetic mode in Fourier space. Given the lobe structure (i.e. three positive and three negative) in Figures 4.13(c) and (d), the most energetic wavenumber is defined as $k_{int} = 2\pi/(L_y/3)$, so that for $L_y = 25.7$m, $k_{int} = 0.7334$ radm^{-1}, for $L_y = 67.5$m, $k_{int} = 0.2793$ radm^{-1}, for $L_y = 100$m, $k_{int} = 0.1885$ radm^{-1}, and for $L_y = 135$m, $k_{int} = 0.1396$ radm^{-1}.

Since the lobes can be clearly discerned with $L_y = 100$m and $L_y = 135$m, in Fourier space the wavenumber of spacing, obtained from $k = 2\pi/L_y$, cannot be larger than $k_{int} = 0.1885$ radm^{-1}. With a lateral width of $L_y = 67.5$m, this wavenumber is captured, but given the $m_y = 32$ gridpoints, more resolution is needed to resolve the vortical motion in greater detail. The domain width is then set to $L_y = 67.5$m, with an increase in lateral gridpoints to $m_y = 64$, because this value should capture the lobe structure noted in Figure 4.13(c) and (d).

Figure 4.14 shows the contour of ω_z for $L_y = 67.5$m with $m_y = 64$ gridpoints; the ρ_c isopycnal is included as the red-dashed line. Notice that the solution now exhibits the same vortical structure as that in Figure 4.13(c) and Figure 4.13(d): three lobes of positive/negative vorticity. More information on the lateral instability, along with the Power Spectral Density (PSD) function, will be discussed

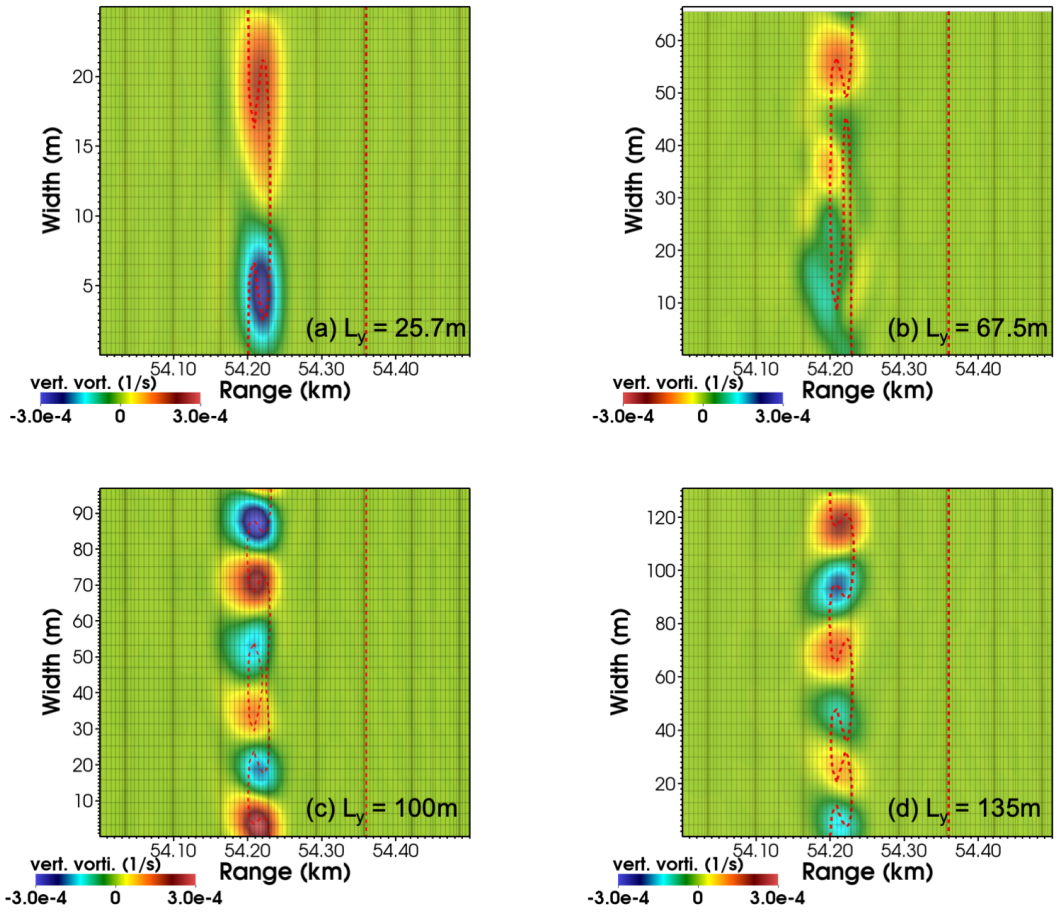

Figure 4.13: Contour of ω_z computed with Equation (4.16) at the subsurface mooring location. Four lateral widths, L_y, are included: L_y = 25.7m in (a), L_y = 67.5m in (b), L_y = 100m in (c), and L_y =135m in (d). The isopycnal corresponding to ρ_c is included as the red-dashed line. In (a) through (d), the number of lateral gridpoints is m_y = 32.

in Section 4.4.5. The remaining analysis of the three-dimensional shoaling simulations is now based on a lateral domain width of L_y = 67.5m with m_y = 64 gridpoints.

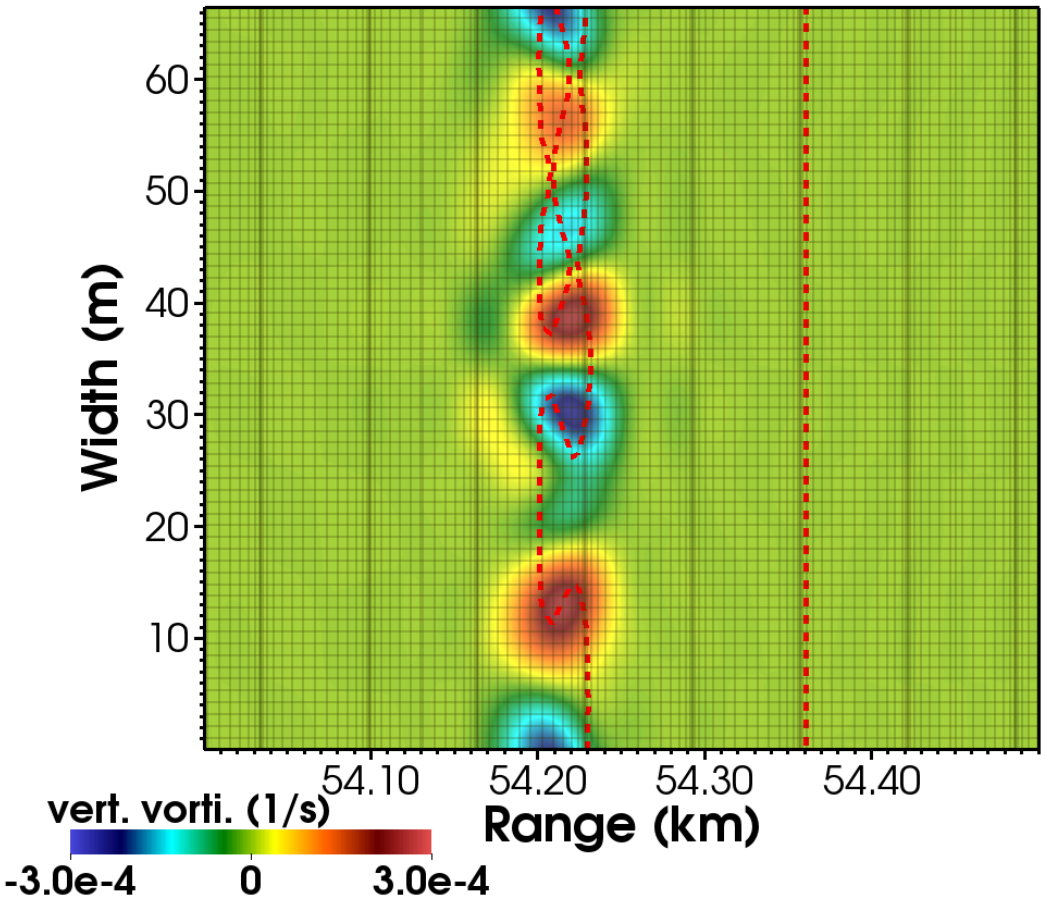

Figure 4.14: Contour of ω_z computed with Equation (4.16) at the subsurface mooring location, for a width of L_y = 67.5m. The isopycnal corresponding to ρ_c is shown as the red-dashed line. The number of lateral gridpoints is m_y = 64.

4.4.4 Convectively unstable shoaling ISW in three-dimensions

Visualizing the ISW at the moorings

The 3D simulated ISW shoaling at the subsurface and surface mooring is shown in Figure 4.15 and Figure 4.16, respectively. Two isosurface values are included: ρ_c (red) and ρ_o (grey). The domain is adjusted so that the ISW can be observed within the window size of the visualization software. The lateral domain is

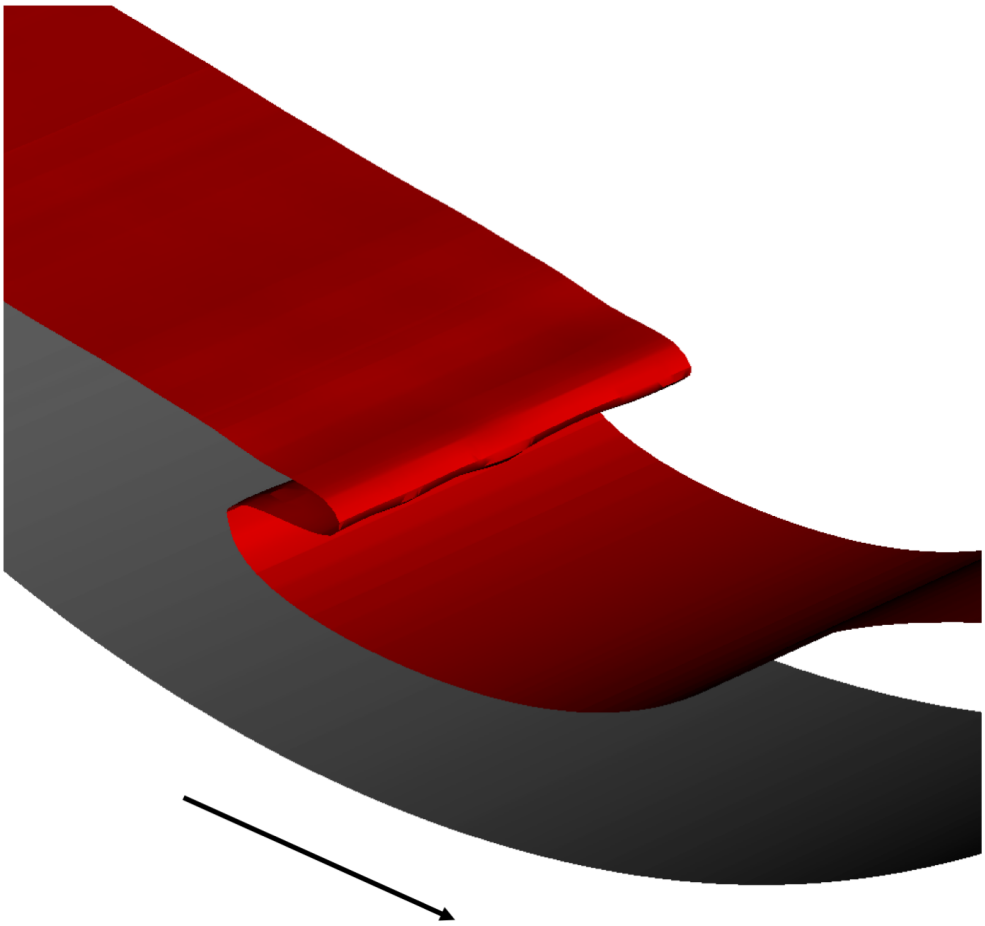

Figure 4.15: Isosurfaces of the convectively unstable ISW shoaling over the SCS bathymetric transect at the location of the subsurface mooring. The isosurface values are: ρ_c (red) and ρ (grey). The domain is adjusted so that the overturning isosurface can be noticed; the lateral domain is increased by a factor of 1.5. The domain length is set to L_y = 67.5m with m_y = 64 lateral gridpoints. The black arrow indicates the direction of propagation.

increased by a factor of 2. The domain with is set to L_y = 67.5m with m_y = 64 lateral gridpoints. The wave propagates in the direction noted by the black-solid arrow, with propagation speed c.

In Figure 4.15, any lateral instabilities are barely noticeable through isosurface visualization, although the ISW does exhibit convective instability, in the

along-wave direction. When the ISW arrives at the surface mooring location (Figure 4.16), lateral instabilities are evident as the ρ_c isosurface exhibits distinct wave-like structures along this direction; this isosurface is also overturning and the pycnocline isosurface remains unperturbed. Given that a subsurface recirculating core exists at this location, it may be breaking in three-dimensions, as the ISW propagates into shallower water retaining its original form.

ISW Properties along the SCS bathymetric transect

To characterize the ISW as it shoals over the SCS bathymetric transect, the maximum ISW-induced velocity, U_{max}, propagation speed, c, amplitude, A, and half-width, L_w, are computed using the procedure discussed in Section 3.3.1, albeit with a modification to account for the lateral dimension. Each wave property is now computed in the x-z plane and averaged along y, with an uncertainty bound obtained by computing the standard deviation. For the propagation speed, first the ISW is located on each lateral x-z plane. Afterwards, the position is averaged in the lateral and the linear least-squares model, with the linear fit, is applied to this average wave location.

The ISW properties are shown in Figure 4.17, along with those from the two-dimensional simulations from Figure 4.4. In Figure 4.17(a) to 4.17(c), the properties of the three dimensional simulations are shown as the blue line and the properties of the two-dimensional shoaling simulation as the black lines. The SCS bathymetric transect is shown in Figure 4.17(d) for reference. The location of the subsurface and surface moorings is also shown as the black-dashed line. Uncertainty bounds are also included in for the 3D simulation, nevertheless these are minute (i.e. $< 10^{-2}$) and barely noticeable.

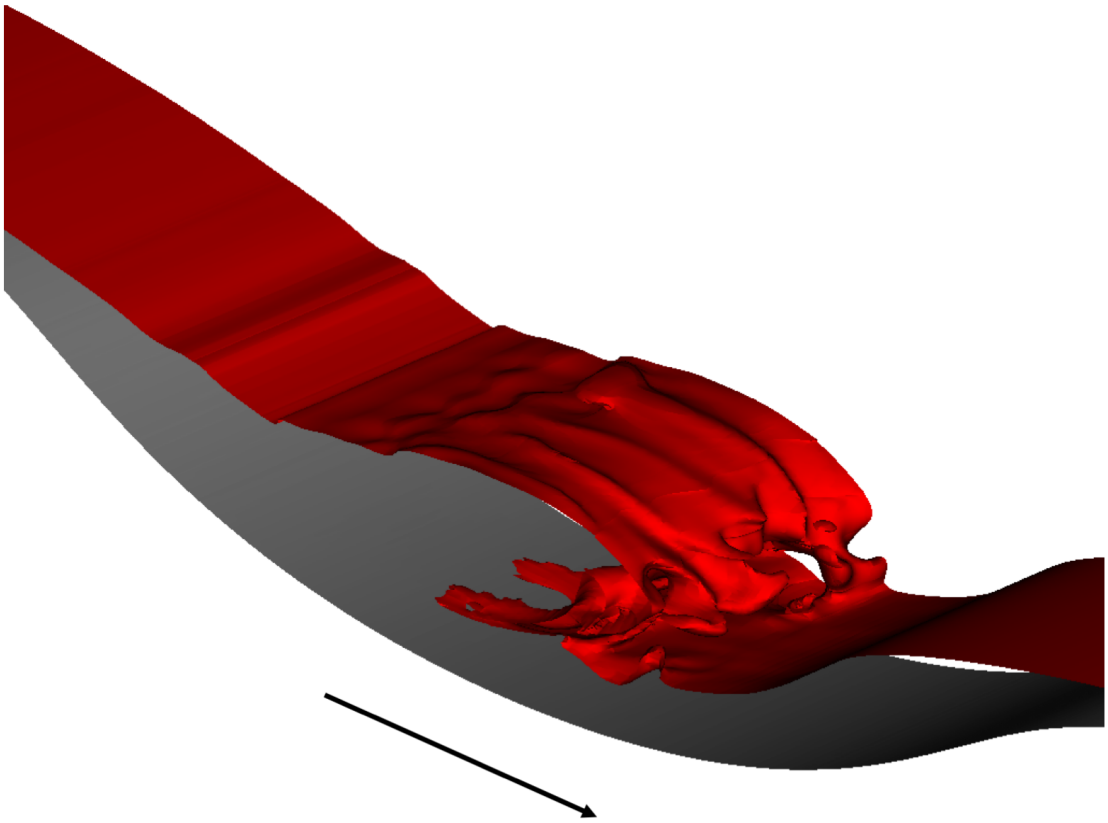

Figure 4.16: Isosurfaces of the convectively unstable ISW shoaling over the SCS bathymetric transect at the location of the surface mooring. The isosurface values are: ρ_c (red) and ρ (grey). The domain is adjusted so that the overturning isosurface can be noticed; the lateral domain is increased by a factor of 1.5. The domain length is set to L_y = 67.5m with m_y = 64 lateral gridpoints. The black arrow indicates the direction of propagation.

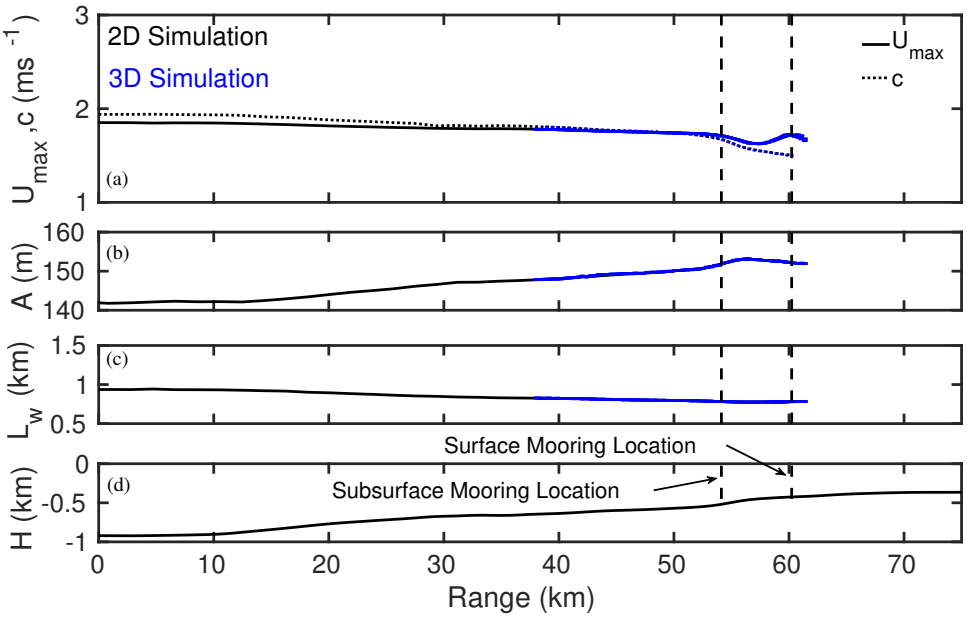

Figure 4.17: Properties of the SCS shoaling simulation in two vs three-dimensions. The properties corresponding to the two-dimensional simulations, originally presented in Figure 4.4, are included for reference as the black-solid line. The properties of the three-dimensional shoaling ISW are included as the solid-blue line; these are computed in every x-z plane and averaged in the lateral y direction. Uncertainty bounds have been included for the 3D simulation. The properties include: maximum ISW-induced velocity, U_{max}, and propagation speed, c, in (a), ISW amplitude, A, in (b), and ISW half-width, L_w, in (c). The SCS bathymetric transect is included in (d) for reference. The location of subsurface and surface mooring is demarcated as the black-dashed lines in (a) through (d).

In Figure 4.17(a), the maximum ISW-induced horizontal velocity is shown as the solid line, along with wave propagation speed as the dashed-line. The three-dimensional simulations exhibit similar values as the two-dimensional simulations, as the curves for U_{max} and propagation speed overlap, in 2D and 3D. Given the definition used for the wave properties, it is possible that while the wave is experiencing three-dimensional breaking near the surface mooring. However, the changes in the wave do not impact neither its translation nor the maximum displaced isopycnal and half-width.

The Available Potential Energy (APE) and Kinetic Energy (KE) are computed

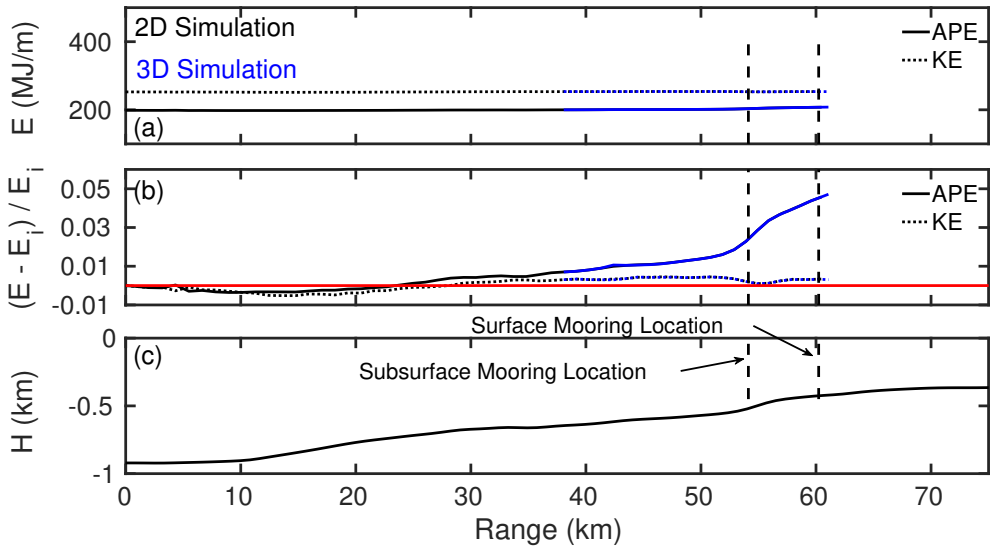

Figure 4.18: Energy of the shoaling SCS in two dimensions (black) and three-dimensions (blue). In (a), the Available Potential Energy (APE) is show as the solid line while the Kinetic Energy (KE) is shown as the dotted line. In (b), the energy relative difference is computed, with respect to their initial value respectively. The solid-red line denotes the zero value. The SCS bathymetric transect is included for reference in (c). In (a) to (c), the location of the surface and subsurface mooring is included as the dashed-black lines. The standard deviation at the subsurface mooring location is 1.03×10^{-4} MJm^{-1} and at the surface mooring location is 0.0245 MJm^{-1}.

and shown in Figure 4.18, along with the two-dimensional simulation data for reference; the former corresponds to the blue lines while the latter to the black lines. Similar to the method used to compute the wave length scales and propagation speed, the APE and KE are computed in the x-z plane, for every lateral gridpoint, and averaged. An an uncertainty bound is obtained from the standard deviation along this direction.

The evolution of APE and KE seems to coincide with those of the two-dimensional shoaling simulations; as the APE increases, the KE remains relatively constant. As such, the simulations may be considered two-dimensional.

Nevertheless, at the surface mooring, Figure 4.16 revels a lateral structure confined to the interior isopycnals. Here, the standard deviation has increased from 1.03×10^{-4} MJm^{-1} to 0.0245 MJm^{-1}, suggesting that the ISW may have lost homogeneity in the lateral direction.

When the ISW experiences convective breaking, over gentle slopes, part of the wave energy is utilized to mix the fluid within the core while other is dissipated [102]. However, given that the present study indicates no net decrease in energy, one might conjecture that, in the field, the energy used for mixing and dissipation is being provided by the background current and not the wave itself.

4.4.5 Visualizing the lateral instability at the moorings

In addition to the vertical vorticity field, shown in Section 4.4.3, the along-wave vorticity, ω_x, the lateral velocity, v', and the isopycnals, ρ, may be used to visualize the lateral instability at the subsurface and surface mooring location. The horizontal vorticity, ω_x is defined as,

$$\omega_x = \left(\frac{\partial w'}{\partial y} - \frac{\partial v'}{\partial z} \right) \hat{\mathbf{i}}. \tag{4.17}$$

Figure 4.19 shows the contours of the horizontal vorticity (a), the lateral velocity (b), and an outweighed density defined as $\sigma = \rho - 1000$ (c); all the properties are shown at the location of the subsurface mooring, in the y-z plane. The ρ_c isopycnal is included as the red-solid line; this is the first isopycnal to become convectively unstable, from the 2D simulations. The oscillations noted in the

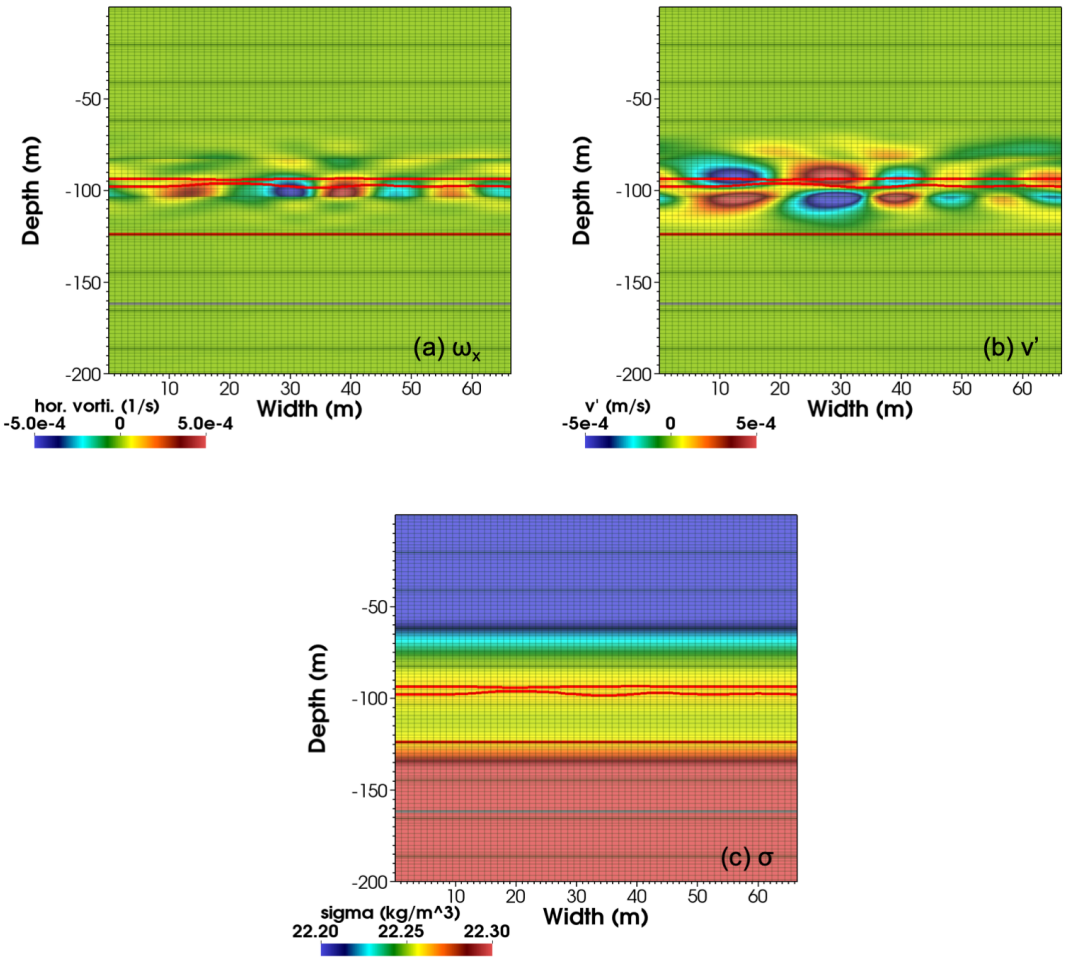

Figure 4.19: Visualization of the lateral instability with the horizontal vorticity, ω_x in (a), the lateral velocity, v', in (b), and outweighed density, $\sigma = \rho - 1000$, in (c) at the subsurface mooring location, in the y-z plane. The horizontal vorticity is computed from Equation (4.17). In (a) through (c), the isopycnal corresponding to $\rho_c = 1022.26$ kgm^{-3} is included as the red-solid line. In (c), σ ranges from 22.20 kgm^{-3} to 22.30kgm^{-3}.

ρ_c isopycnal are an indication of convective breaking. The heavy fluid, pulled from behind the ISW into the region above the trough, displaces light fluid. As the lighter fluid is displaced, lateral motion is induced. Lateral motion induces horizontal vorticity, as shown in Figure 4.19(a). The outweighed density values, in Figure 4.19(c), range from 22.20 kgm^{-3} to 22.30kgm^{-3}.

In addition to visualizing ω_x and v', the lateral instability, originally shown in Figure 4.13, may be characterized by a highly-energetic wavenumber, in spectral space, corresponding to the actual length scale of the instability. In Section 4.4.3, the characteristic wavenumber was found to be $k_{int} = 0.7334$ radm^{-1}. If the Power Spectrum Energy (PSD) [140] function of the lateral velocity, $G_{v'v'}$ is computed, over a volume that covers the convectively unstable portion of the ISW, a peak value should reside at the k_{int} wavenumber.

Figure 4.20 shows the PSD for the lateral velocity v', $G_{v'v'}$, along with a horizontal cut (i.e. x-z plane) of the convectively unstable portion of the ISW. In Figure 4.20(a), the horizontal cut shows the ρ_c isopycnal profile at every lateral gridpoint. The PSD is computed, for every point in the x-z plane, along the lateral direction; the resulting PSD is included as a grey-solid line in Figure 4.20(b). An average in x-z of the solid-grey lines is computed and shown as a solid-blue line. In addition, a reference line with a slope of $m = -5/3$ is included and shown as the magenta-dashed line; this slope value corresponds to that of the inertial subrange for homogeneous and isotropic turbulence [140]. It is not known *a priori* if the flow associated with the ISW becomes turbulent, and the representative magenta-dashed line may be regarded as the first step in determining whether the flow may be turbulent or not. Lastly, the first wavenumber on which the exponential filter acts, is shown as the black-dashed line; higher wavenumbers are being damped.

The value of $G_{v'v'}$ decreases with increasing wave number, but the slope of the curve does not follow the m = -5/3 value. Hence, the flow, associated with the ISW at the surface mooring, is most likely not turbulent. In addition, no peak $G_{v'v'}$ value can be discerned at k_{int}, from the either the individual PSD profiles or

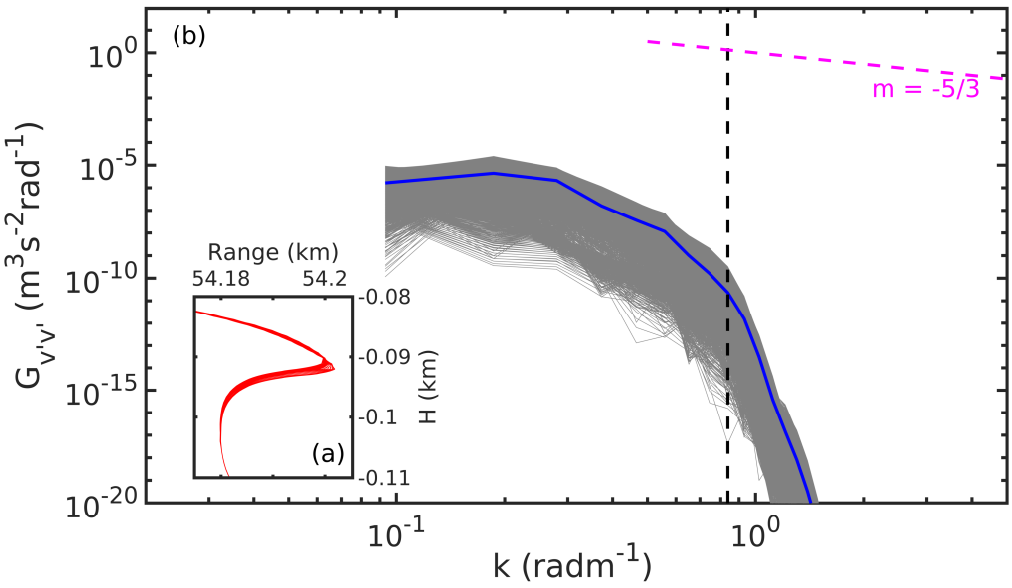

Figure 4.20: Power Spectra Density (PSD) function of the lateral velocity, v', computed across a volume that encompasses the core of the ISW, at the sub-surface mooring location. In (a), the x-z plane of the volume is shown, with the isopycnal of $\rho = 1022.26$ kgm^{-3} in red; the isopycnal profile for every gridpoint in the lateral direction is also included. The PSD is computed for every x-z lateral velocity value, inside the volume, in the lateral direction. In (b), the resulting PSD is included as a gray-solid line. The blue-solid line is the averaged PSD, obtained by averaging the PSD in the x-z plane. The magenta-dashed line is a reference line with a slope of $m = -5/3$, characteristic of homogenous free-shear turbulence. The first wavenumber on which the exponential filter acts, is shown as the black-dashed line.

the averaged PSD. It may be possible that, because not spectral profiles, in the x-z plane, lie within the unstable ρ_c isopycnal, the peak was filtered during the process to obtain the averaged $G_{v'v'}$, and is hidden within all the lateral profiles denoted by the grey lines.

Figure 4.21 shows the horizontal vorticity, ω_x, the lateral velocity, v', and the outweighed density, $\sigma = \rho - 1000$, at the surface mooring location. In 4.21(a) and (b), ω_x and v are shown along with the ρ_c isopycnal as the red-solid line and the pycnocline as the grey-solid line. In 4.21(c), the outweighed density ranges

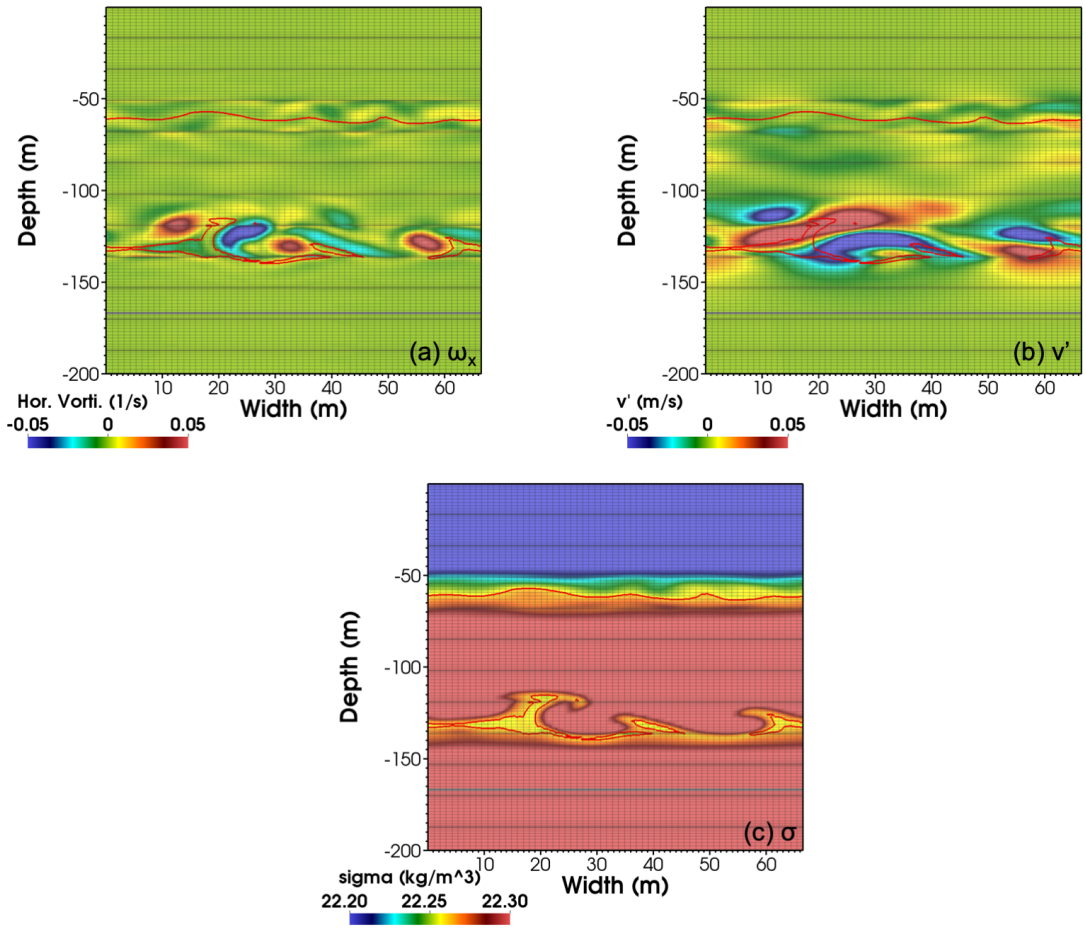

Figure 4.21: Visualization of the lateral instability with the horizontal vorticity, ω_x in (a), the lateral velocity, v', in (b), and outweighed density, $\sigma = \rho - 1000$, in (c) at the surface mooring location, in the y-z plane. The horizontal vorticity is computed from Equation (4.17). In (a) and (b), the isopycnal corresponding to ρ_c is included as the red-solid line and the pycnocline as the solid-grey line. In (c), σ ranges from 22.20 kgm^{-3} to 22.30kgm^{-3}.

from 22.20 kgm^{-3} to 22.30kgm^{-3}; there are a total of 11 isopycnals.

The ISW at the surface mooring location exhibits clear lateral structure, as opposed to the subsurface mooring location. The lateral structure may be associated with the sinking heavy fluid, that was pulled into the ISW during the onset of convective breaking, near the subsurface mooring location. As the heavy

fluid sinks, it displaces lighter fluid located below, closer to the pycnoline. The displaced light fluid rises, causing the formation of lateral convective instabilities, as shown in Figure 4.21(c), which corresponds to the density field. This lateral convective instability enhances the lateral structure of the flow; finer scale vortical motion can be clearly discerned from Figure 4.21(a). This mechanism of generation of horizontal vorticity has been studied in the context of breaking interfacial waves [55, 12], breaking internal waves [188], and the breaking of internal gravity waves beneath critical layers [49].

The PSD for the lateral velocity, $G_{v'v}$, is computed at the surface mooring location. Figure 4.22 shows the obtained spectra, from a volume that encompasses the convectively unstable region within the ISW. The x-z plane of the volume is shown in 4.22(a), along with the isopycnal that corresponds to ρ_c as the solid-red line, for every lateral gridpoint. In (b), the resulting PSD, $G_{v'v'}$, for every location in the x-z plane along y, is shown as a grey-solid line. The averaged $G_{v'v'}$, computed by averaging the grey-solid lines, is included as the solid-blue line. In addition, a reference line with a slope of $m = -5/3$ is plotted. Similarly to the subsurface mooring location, it is not known *a priori* if the flow associated with the ISW is turbulent at the surface mooring location. The first wavenumber on which the exponential filter acts, is shown as the black-dashed line; higher wavenumbers are being damped

The slope of the computed PSD, shown in Figure 4.22(b), does not follow the m = -5/3 value. Therefore, the flow at the core of the wave is not regarded as turbulent, although it may be in the process of becoming turbulent because of the changes in the average profile of $G_{v'v'}$. The slope of the averaged-profile is closer to the $m = -5/3$ value at the surface mooring location than at the subsur-

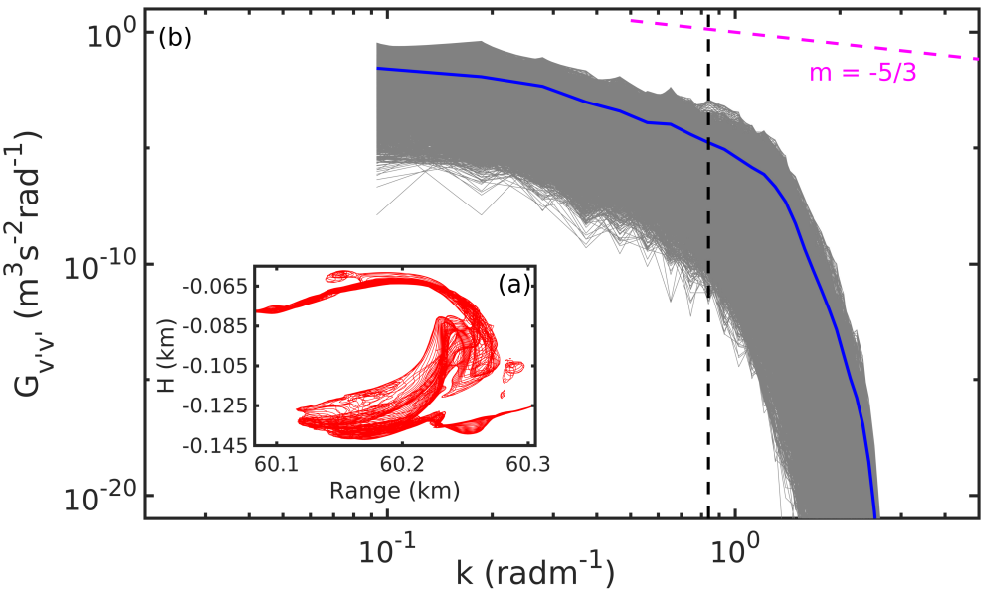

Figure 4.22: Power Spectra Density (PSD) function of the lateral velocity, v', computed across a volume that encompasses the core of the ISW, at the surface mooring location. In (a), the x-z plane of the volume is shown, with the isopycnal of ρ_c in red; the isopycnal profile for every gridpoint in the lateral direction is also included. The PSD is computed for every x-z lateral velocity value, inside the volume, in the lateral direction. In (b), the resulting PSD is included as a gray-solid line. The blue-solid line is the averaged PSD, obtained by averaging the PSD in the x-z plane. The magenta-dashed line is a reference line with a slope of $m = -5/3$, characteristic of slope of the inertial subrange in homogenous and isoptropic turbulence. The first wavenumber on which the exponential filter acts, is shown as the black-dashed line.

face mooring location.

Figure 4.22(b) also indicates that the smallest wavenumbers seem to be more energetic at the surface mooring than at the subsurface mooring location, given their higher $G_{v'v'}$ value. Large-scale lateral motion oculars due to the convective overturn. Thus, the present study highlights the three-dimensional onset of convective breaking and subsequent convective overturn, which leads to the formation of the recirculating subsurface core, as the ISW shoals over gentle slopes.

4.5 Discussion

4.5.1 Examining the evolution of Kinetic Energy

Worthy of note is the significance of the KE and APE in the context of shoaling and breaking waves. The KE may be regarded as the energy to be dissipated by the breaking wave, while the APE may be regarded as the energy available for mixing [82, 103]. When an ISW shoals, the sudden increase in APE is typically associated with a decrease in KE through the buoyancy flux [98]; as the buoyancy flux increases, the APE increases while the KE decreases. The decrease in KE and increase in APE is shown in Figure 4.10, for an ISW shoaling without without a background current. In the presence of a background current, the wave KE seems to be relatively constant while the APE increases, as shown in Figure 4.18.

The evolution of the KE, originally discussed in Section 4.4.4, may be explored by examining the two terms contributing to the production of KE [92, 175]: the buoyancy flux and shear production. The buoyancy flux is given as [82, 175],

$$B = \frac{-g\rho' w'}{\rho_o} = -bw'. \tag{4.18}$$

The shear production term is given as,

$$S = -u'w'U_z. \tag{4.19}$$

In Equation (4.18) and (4.19), ρ', u', and w' correspond to the ISW-induced density perturbation, horizontal, and vertical velocity; the quantity U_z is the background shear, or the vertical derivative of the background current profile, U. In the context of turbulent flows, Equation (4.18) and (4.19) may form part of the Turbulent Kinetic Energy Equation [92], but ρ', u', and w' would be associated with the turbulent fluctuation of the ISW-induced field.

The buoyancy flux, B, and shear production, S, is shown in Figure 4.23(a) and 4.23(b), respectively. Similar to the computation of the wave properties described in Section 4.4.4, Equation (4.18) and (4.19) are computed in the x-z plane, and averaged in the lateral; uncertainty bounds of this average may be obtained by computing the standard deviation in the lateral. The SCS bathymetric transect is included for reference in Figure 4.23(c).

As the ISW reaches the location of the subsurface and surface mooring, the magnitude of S and B increases; an increase in B corresponds to an increase in APE [82]. The error bounds indicates that closer to the surface mooring location, the simulation data is very uncertain. Here, the interior isopycnals are breaking, as noted in Figure 4.16. Prior to this breaking, it may be conjectured that the background shear provided most of the APE gained by the ISW, as it shoaled, thus the KE remaining relatively constant. The background shear would contribute to the energy dissipated and the energy used to mix the ambient fluid.

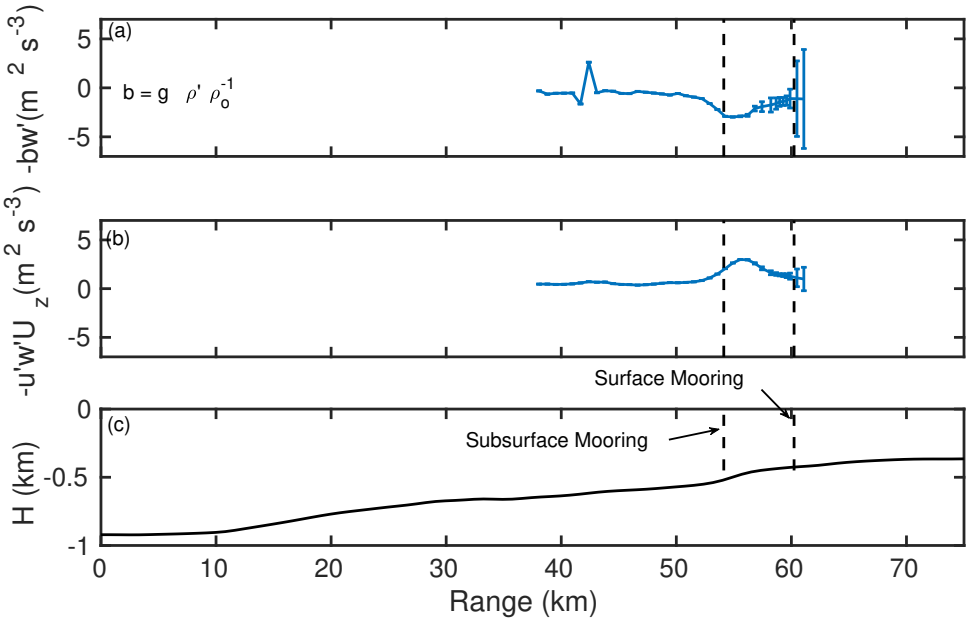

Figure 4.23: Evolution of the sources of KE for the shoaling ISW in the presence of a background current; these are: buoyancy flux (a) and shear production (b). Both sources are computed in the x-z plane and averaged in the lateral. Errorbounds are obtained from the standard deviation in the lateral direction. The SCS bathymetric transect is included for reference in (c). The location of the subsurface and surface mooring is also included as the black-dashed lines in (a) through (c).

4.5.2 Examining the Length Scales of Interest in the Shoaling ISW

The size of the convective overturn may be obtained by considering the Thorpe Scale, L_T [175]. The Thorpe Scale is a measure how far a parcel of fluid has been displaced from its stable reference location. For a given location in the along-wave direction, L_T is obtained by first, sorting the density profile into a stable, and monotonically increasing, configuration, then computing the difference between the stable and unstable configuration fluid parcel depth; L_T is the root-mean-square of the difference in depth [164]. More formally, the Thorpe Scale may be expressed as,

$$L_T = \langle \delta_T^2 \rangle^{1/2} \tag{4.20}$$

where δ_T is the vertical, z, displacement of each parcel and is defined as $\delta_T = z - z_{sorted}$. In the present study, the Thorpe Scale is computed from the 3D simulation data, using the approach described in Section 4.4.4, for the rest of the wave properties. The length scale is first obtained in the x-z plane, then averaged along the lateral direction; an uncertainty bound is obtained by computing the standard deviation in the lateral direction.

Figure 4.24 shows the laterally-averaged Thorpe Scale, for the ISW at the surface mooring location. In 4.24(a), the density profile for the unstable fluid configuration is shown as the blue-solid line; the sorted profile is shown as the red-solid line. Sorting is accomplished via a parallel sorting algorithm based on a probability density function of the density profile [189, 178, 154]. The corresponding parcel displacement, δ_T, is shown in 4.24(b). Using Equation (4.20), the Thorpe Scale at the surface mooring is L_T = 17m, with an uncertainty of ± 1.1087m. For reference, field observations of shoaling ISWs over the SCS bathymetric transect suggest Thorpe Scale values ranging between 6m and 52m [102, 103].

In addition to computing L_T at the surface mooring, the evolution of the Thorpe Scale is computed along the SCS transect and shown in Figure 4.25. The laterally-averaged L_T is obtained at the location of the ISW; the result is shown in 4.25(a). The SCS bathymetric transect is included in 4.25(b) for reference. The location of the subsurface and surface mooring is shown as the black-dashed lines in both (a) and (b).

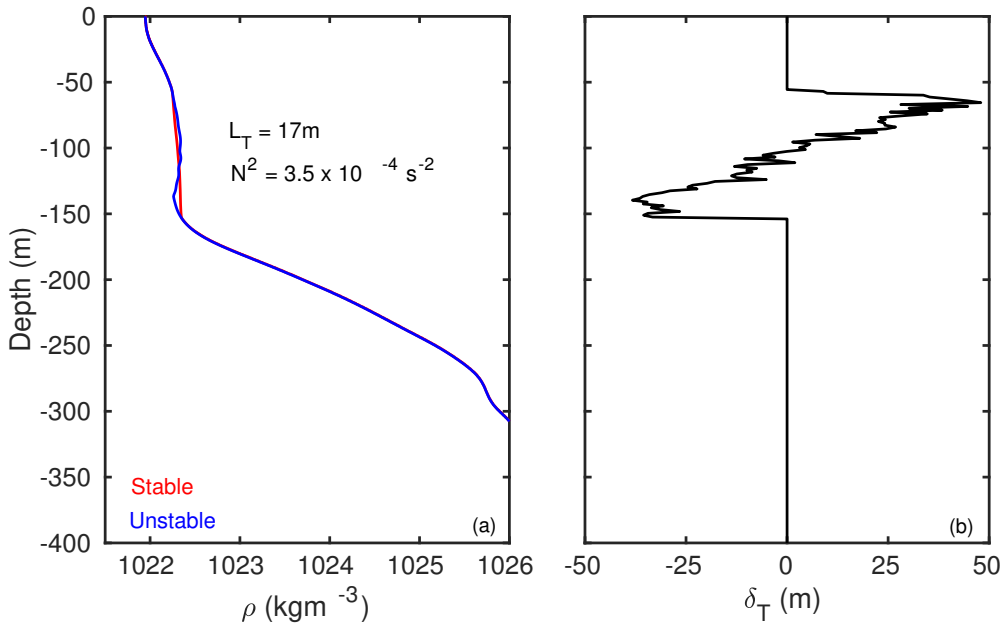

Figure 4.24: (a) Laterally-averaged profile of the stable (sorted) and unstable (unsorted) density associated with the shoaling ISW at the surface mooring location. (b) Laterally-averaged displacement of the fluid parcels, δ_T, from their stable configuration. In (a), the unstable (unsorted) density is denoted by the blue-solid line while the stable (sorted) density corresponds to the red-solid line. The stable profile is obtained by sorting the unstable profile using a parallel sorting algorigthm [154]. The Thorpe scale, L_T, is computed using Equation (4.20) with δ_t. The uncertainty in the computed length scale is ± 1.1087m. The BV Frequency, N^2, is obtained from the laterally-averaged sorted density profile.

The peak L_T between mooring locations has a value of approximately 18.24m ± 0.643m. The location of this value may be a proxy for the onset of turbulent motion [163], not the presence of turbulence itself. The maximum L_T is akin to the maximum overturn; afterwards convective motion, associated with the falling heavy fluid and rising light fluid, drive turbulent motion. However, after the mooring location, the L_T curve increases, indicating the presence of a larger overturn, though the uncertainty increases as well. Such phenomenon may be linked to a possible increment of heavy fluid, that enters the ISW from behind, as the wave shoals. Nevertheless, the large uncertainty indicates that fluid parcel displacement varies in the lateral, most likely due to the lateral overturns, first

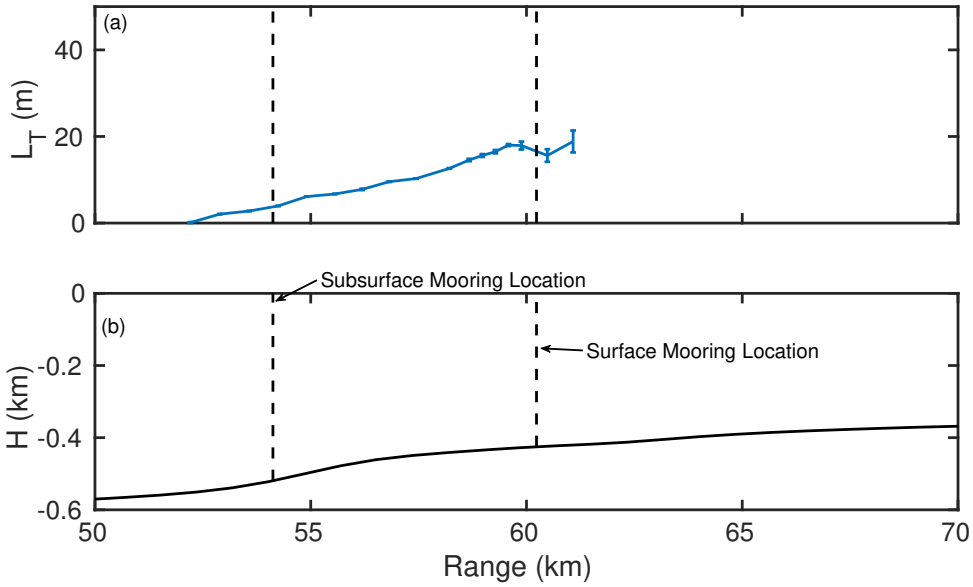

Figure 4.25: Evolution of the Thorpe Scale, L_T, along the SCS bathymetric transect. In (a), the laterally-averaged L_T is shown along with the errorbound obtained from the standard deviation, along the lateral direction. The SCS bathymetric transect is shown in (b) for reference. The Thorpe Scale is computed at the location of the ISW. The location of the subsurface and surface mooring is shown as the black-dashed lines in both (a) and (b).

shown in Figure 4.21, generated by the primary convective overturn.

Oceanographers commonly use the Thorpe Scale to estimate the dissipation of turbulent kinetic energy. Such process involves relating L_T to the Ozmidov Scale, L_O; the latter is a measure of the vertical size of the largest eddy that experiences buoyancy and is defined as $L_O = \epsilon^{1/2} N^{-3/2}$, where ϵ is the dissipation and N^2 is the BV Frequency. Field observations of mixing layers indicate that $L_T/L_O \approx 0.80$ [47], and with this value one can then solve for ϵ. Such process is known as the Indirect Method of computing the dissipation [175]. Thus, Thorpe Scale, along with the Ozmidov Scale, represent some of the most important length scales of stratified flows.

CHAPTER 5

CONCLUSIONS AND FUTURE WORK

The propagation of an internal solitary wave of depression over a flat surface and across a gently varying bathymetry has been explored, separately, in two and three-dimensions, using highly accurate numerical simulations. The objective of the dissertation was to examine the role of the wave-induced pressure at the bed and, also, how the water column properties impact the shoaling process over gentle slopes, namely in the context of convective breaking of high amplitude ISWs. Three separate studies were conducted, addressing key problems associated with aforementioned objectives. In this Chapter, the conclusion of each study is included as a separate section. Future work is also addressed at the end of each section.

5.1 On the ISW-induced pressure at the bed

In Chapter 2, the bed response due to the induced pressure of an internal solitary wave of depression was explored. The total pressure was taken as the sum of both the hydrostatic and non-hydrostatic components. Neglecting the effects of the free-surface displacement induced pressure, ISWs were capable of inducing bed failure, due to their inherently negative pressure, which acts to draw fluid from the bed. A failure criterion that compares the vertical pressure gradient to the submerged specific weight of the porous medium was employed.

A small amount of trapped gas in the porous bed was assumed in the analysis, to account for the possible presence of organic material decomposition. The compressibility of the gas hinders fluid seepage through the porous medium

during ISW propagation, substantially contributing to the pressure attenuation near the top. This, in turn, gives rise to higher vertical pore-pressure gradient, capable of failing the bed. The simulation indicated that failure occurs for weakly conductive materials.

The thickness of the failed layer was comparable to the documented thickness of failed sediment deposits in the presence of surface waves. Furthermore, the vertical pore-pressure gradient acted to reduce the buoyant weight of the particles, within the bed, impacting the criterion of incipient motion and, possibly, contributing to resuspension processes observed during the propagation of ISWs. When the pressure induced by the free-surface displacement was considered, the possibility of failure was reduced across all bed types and saturation values. At depths typical of the continental shelf (i.e. $H < 100$m), only silts with a significant amount of trapped gas met the failure criteria. Deep-water ISWs (i.e. $H \geq 100$m) were still capable of inducing failure for silt beds, regardless of the degree of saturation. These results were based on a density jump at the pycnocline, that may not characterize that at deeper waters, where ISWs have been observed. Nonetheless, the density jump highlighted the importance of the wave propagation speed as another parameter responsible for the change in pore-pressure during ISW propagation, and possible failure, in addition to the wavelength, whose role has been identified in previous studies.

Chapter 2 largely focused on the induced pore-pressure of ISWs of depression and was limited to analyzing the vertical changes inside the bed. However, highly nonlinear ISWs are also capable of inducing horizontal pressure gradients which might impact the bed dynamics. Studies of surface wave-induced liquefaction have highlighted the influence of the associated streamwise pres-

sure gradient and suggest that a failure criterion based on the horizontal pressure gradient is attainable. Future work will be devoted to addressing failure due to the horizontal pressure gradient, for both ISWS of depression and elevation, by reevaluating the assumptions of the bed properties and dimensions. Specifically, the assumption of unidirectional bed consolidation can be relaxed by considering bed motion in the streamwise direction as well. In this case, the horizontal and vertical scales will both enter the problem. Failure can also be enhanced by the presence of a train of waves, due to the prolonged exposure to pressure changes [158]. Consequently, the study of a train of nonlinear internal waves could similarly enhance potential for bed failure.

5.2 On the formation of subsurface recirculating cores in 2D

In Chapter 3, the shoaling of an internal solitary wave of depression, over realistic bathymetry and background field conditions, was simulated by solving the incompressible Navier-Stokes Equations under the Boussinesq Approximation in two-dimensions, using a high-order spectral multidomain penalty method (SMPM). The bathymetry, density, and background current fields in the water column were measured by *RCL2014* in the South China Sea (SCS) [103]. Particular emphasis was placed on the formation and evolution of recirculating subsurface cores during the shoaling process, within the constraints of 2D dynamics where there is no viscous dissipation and fluid mixing; the aforementioned processes are inherently three-dimensional. The objective of the study was to explore variations in the wave properties that support the existence of these cores, as observed in the South China Sea [102, 103]. The formation of a subsurface recirculating core in an ISW of depression shoaling over gentle slopes had never

before been simulated using actual field data as forcing.

The initial conditions representing the ISW were obtained from the solution of the Dubreil-Jacotin-Long (DJL) Equation, as forced by the observed density and background velocity field. The computed wavefield was then interpolated onto the deeper region of the SMPM grid. The shoaling simulation indicated the presence of subsurface recirculating cores, as observed in the field. The cores form because of the sign of the relative vorticity associated with the background current, which is opposite to that of the propagating ISW. The background fields of the simulation were kept steady in time, homogeneous in the along-wave direction, and only varied with depth.

The location of the subsurface and surface mooring, deployed by *RCL2014* along the SCS transect, was used to guide the subsequent analysis throughout the Chapter. The simulations explored the sensitivity of core formation to the initial wave amplitude, near-surface background shear, and maximum slope within the SCS bathymetric transect. Rotational effects were not included, although for shoaling ISWs over gentle slopes, the effect of the changing water depth is more dominant [99].

For a given initial ISW with an amplitude of 143m, results indicated that the height of the convectively unstable region was slightly below the observed value. The size of the convectively unstable region was defined by demarcating where the maximum ISW-induced horizontal velocity, U_{max}, equals the wave propagation speed, c. This region was also used as a proxy for determining the overturn length scale. The simulation suggested an convectively unstable region of 45m in height. Other definitions used to visualize the convectively unstable region included the streamlines in a reference frame moving with the

wave, which showed the presence of two regions of closed streamlines, characteristic of recirculating fluid. This streamline configuration was observed in the field and is distinct to subsurface recirculating cores [102].

In addition, the impact of the maximum slope at the SCS bathymetric transect was explored by performing a simulation with an attenuated slope value, near the location of the subsurface and surface moorings. Results showed that the maximum slope expedited the formation of the subsurface recirculating core. Regardless of slope value, the ISW became convectively unstable. No changes in the length scale of the wave were noted. Thus, it may be possible that subsurface cores occur elsewhere in the ocean, yet are easily noticeable near the Dongsha Slope given its unique bathymetry.

Variations in the initial conditions were also explored by changing the initial amplitude and inserting larger waves. None of the simulated ISWs matched the amplitude, half-width, maximum horizontal velocity, and wave propagation speed observed by *RCL2014* at the surface and subsurface mooring location along with the shipboard measurements. This inconsistency was attributed to the choice of initial condition, which does not correspond to the upstream conditions that may have resulted in the observed wave by *RCL2014*.

Finally, the effect of the shear, associated with the profile of background current, was studied by modifying its near-surface magnitude, but preserving its direction. The simulation indicated that, while the wave length and velocity scales did not vary from the original profile, the size of the convectively unstable region near the surface mooring did; the larger the magnitude, the larger the size of the region and possibly that of the recirculating subsurface core.

Given that the size of the actual subsurface recirculating core may be different than that of the convectively unstable region, future studies will incorporate a particle tracking technique, that provides an accurate method of determining core boundary. While visualizing the density field or the streamfunction indicates the presence of trapped fluid, it is not indicative of the amount of mass being transported by the wave. The transport is large for recirculating subsurface cores than surface recirculating cores, and it may be unique to the SCS region, where resuspended sediment and bottom particulates have been observed to reach the continental shelf.

5.3 On the initial instability, in 2D and 3D, preceding the formation of subsurface recirculating cores

In Chapter 4, the initial instability in a shoaling of an internal solitary wave (ISW) of depression, over realistic bathymetry and background field conditions, was simulated by solving the incompressible Navier-Stokes Equations under the Boussinesq Approximation in two and three-dimensions, with a high-order spectral multidomain penalty method (SMPM). The bathymetry, density, and background current fields, used to generate the initial conditions, were obtained from the work of *RCL2014*, and correspond to the water column properties in the South China Sea (SCS) [103].

The field observations of *RCL2014*, and results discussed in Chapter 3, indicated the presence of a convective instability prior to the formation of a recirculating subsurface core. However, it may be possible that, given the resolution of the field instruments, and the computational resolution of the simulations, shear

instabilities could also be occurring as well. If these are not resolved during the simulations, then they manifest as small perturbations of the isopycnals. Therefore, one of the objectives of the Chapter was to examine the possible presence, in 2D, of these instabilities during the shoaling process.

The initial conditions representing the ISW, were obtained from the solution of the Dubreil-Jacotin-Long (DJL)Equation [106, 179, 52], with the observed density and background current field [103]. These chosen solution was the same as that from Chapter 3. The computed wavefield was then interpolated onto the deeper region of the SMPM grid. The grid was generated from the SCS bathymetric transect water depth, where the ISW propagates in the normal-to-isobath direction, with a horizontal resolution doubled from that corresponding to the study addressed in Chapter 3.

The location of the subsurface and surface mooring deployed by *RCL2014* was used to guide the analysis of the simulation data. With regards to the presence of shear instabilities, at the subsurface mooring location, the Richardson number (Ri) was lower than 0.10, but only at where convective breaking occurs. This critical Ri value occurred because of the preceding convective instability, since the wave propagation speed decreased below the horizontal velocity field, prior to the ISW reaching the mooring location. Therefore, the primary instability was determined to be convective, for the prescribed background density and current profile, along with the SCS bathymetric transect.

When the simulation was restarted in three-dimensions, the computed wave properties were very close to those from the two-dimensional simulation. However, lateral motion was detected at the subsurface mooring location and overturning, with a clear lateral structure, was obtained at the surface mooring lo-

cation. Thus, the mentioned wave properties were not impacted by the core dynamics, yet the ISW was not 2D.

The simulated ISW available potential energy (APE) and kinetic energy (KE) indicated that, as the the APE increased, the KE remained relatively constant. For shoaling ISWs, as the amplitude increases, the propagation speed decreases, which is analogous to an APE increase and a KE decrease. An auxiliary simulation, in 2D, without a background current was performed, to ensure that the aforementioned process occurs; the evolution of the KE and APE agreed with the stipulated description. Therefore, the constant KE was linked to the presence and structure of the background current.

The production of KE was associated with the background shear and buoyancy flux. As the ISW shoaled, KE was being produced by the background shear and transferred to the APE through the buoyancy flux. Thus, the KE remained relatively constant throughout the simulation. The work of *RCL2014* indicated that, the KE increased above the APE near the mooring location, and then decreased below the APE, although there is a difference between their KE definition and that used in Chapter 4. The particular definition would play a significant role in the interpretation of the energetics of the wave.

Lastly, the size of the convective overturn, denoted as the Thorpe Scale, was computed along the SCS bathymetric transect. The obtained value was 17m; the value observed by *RCL2014* was 52m, but for an ISW corresponding to a different day than that used in the simulations. Field observations of convectively unstable ISWs shoaling over gentle slopes have suggested overturn scales between 6m and 52m [102, 103].

Future studies will focus on the turbulent flow at the subsurface recirculating core. Particular emphasis will be placed on the vorticity cascade in the lateral direction, which was simulated in the present study. An analysis of the turbulence flow will indicate the amount of dissipation and mixing associated with the propagating ISW. Finally, with the three-dimensional simulation, the definition of the recirculating subsurface core can also be addressed, via the incorporation of a highly accurate particle tracking technique. Such method can also provide a quantification of the recirculating core mass transport, as the ISW shoals over gentle slopes.

APPENDIX A

SUPPLEMENTAL MATERIAL

A.1 The Dubreil-Jacotin-Long (DJL) Equation with a baroclinic background current

For a reference frame defined in ξ-ζ coordinates, moving with the propagation speed of the ISW under consideration, the steady, incompressible, and inviscid flow, the Dubreil-Jacotin-Long (DJL) Equation [106] can be derived from the incompressible Euler Equations under the Boussinesq Approximation [179]. The result is the isopycnal displacement, η. If the effect of a steady background velocity profile $U(\zeta)$ is included, the DJL Equation can be expressed as,

$$\nabla^2\eta + \frac{U'(\zeta-\eta)}{c-U(\zeta-\eta)}\left(\eta_\xi^2 + (1-\eta_\zeta)^2 - 1\right) + \frac{N^2(\zeta-\eta)}{(c-U(\zeta-\eta))^2}\eta = 0, \tag{A.1}$$

$$\eta = 0 \text{ at } \zeta = 0, H, \tag{A.2}$$

$$\eta = 0 \text{ at } \xi \to \pm\infty, \tag{A.3}$$

where $\eta(\xi,\zeta)$ is the isopycnal displacement, c is the wave propagation speed, $N^2(\zeta)$ is the Brunt-Väisälä (BV) Frequency, and $U(\zeta)$ is the background current profile; both $N^2(\zeta)$ and $U(\zeta)$ are preexising water column properties, without the wave-driven perturbation; the subscript denotes differentiation along the specified variable. With the isopycnal displacement, the density $\rho(\xi,\eta)$, horizontal,

$u(\xi, \zeta)$, and vertical, $w(\xi, \zeta)$, velocity fields induced by the ISW can be obtained from,

$$\rho = \rho(x, \zeta - \eta), \tag{A.4}$$

$$u = U(\zeta - \eta)(1 - \eta_\zeta) + c\eta_\zeta, \tag{A.5}$$

and,

$$w = U(\zeta - \eta)\eta_\xi - c\eta_\xi, \tag{A.6}$$

respectively. Note that, if there is no background current, a solution for η can still be obtained.

Equation A.1 is solved iteratively, by first specifying a BV Frequency and background current profile, then defining a target available potential energy (APE) [52] for the desired wave-driven disturbance. The APE is regarded as the minimum energy required to adiabatically bring a parcel of fluid from its displaced location back to its reference location [189, 96]. The APE may be obtained by first defining the APE density, E_a as,

$$E_a(\xi, \zeta) = g \int_{\zeta - \eta}^{\zeta} (\rho(\xi, \zeta) - \overline{\rho}(s'))\, ds', \tag{A.7}$$

where g is the gravitational acceleration, ρ is the density field including the wave-driven disturbance, and $\overline{\rho}$ is the background density profile, invariant in

the along-wave propagation direction. The APE is the volume integral of E_a (e.g. in 2D, APE = $\int \int E_a \, d\zeta d\xi$).

The iterative solver is initialized with $\eta(\xi, \zeta)$ first estimated from weakly nonlinear theory [52]. With the η field, the associated APE is then calculated using Equation (A.7) and compared against the target APE. If the difference is not below a certain threshold, then the iterative procedure resumes. At each successive iteration, an improved isopycnal displacement estimate is obtained by solving the nonlinear eigenvalue problem, with the previous solution of η as the initial guess; the APE is recomputed and compared with the target value until convergence is achieved. Throughout this iterative process, the wave-driven disturbance progressively increases until the target APE value is reached.

A.2 Expression for Soil Compressibility Parameters

The compressibility of the bed can be expressed in terms of Lamé's parameters as,

$$\alpha = \frac{1}{(2\mu + \lambda)}, \tag{A.8}$$

where μ is the shear modulus and λ is Lamé's first parameter. Effective Lamé's parameters, denoted by $\bar{\lambda}$ and $\bar{\mu}$, can be expressed in terms of the vertical effective stress, σ_η, of the grains by assuming that the particles are spherical and noncohesive. The shear modulus and Lamé's first parameter in Equation A.8 depend on the shear modulus of the grains (i.e. taken to be quartz, $\mu = 10^9 GPa$), the number of contacts per particle, K, Poisson's ratio ν, the radius of contact per

sphere a and the particle radius R [46]. The effective vertical stress is expressed as $\sigma_\eta = (\rho_s - \rho_o)g\eta$, where ρ_s is the particle density, ρ_o is the fluid density and η is the vertical coordinate, within the bed. Assuming that deformations in the bed are much larger than deformations in the grains, during contact, the effective Lamé's parameters can be expressed as,

$$\bar{\lambda} = \frac{\mu K(1-n)}{5\pi(1-\nu)}\left(\frac{a}{R}\right), \tag{A.9}$$

and

$$\bar{\mu} = \frac{2\mu K(1-n)}{5\pi(1-\nu)}\left(\frac{a}{R}\right). \tag{A.10}$$

The contact radius the adhesion region between grains may be related to the vertical effective stress [46]. In the absence of adhesion, the normalized contact radius a/R can be expressed as,

$$\left(\frac{x}{R}\right)^3 = \frac{3\pi}{2K}\frac{(1-\nu)}{(1-n)}\frac{\sigma}{\mu}. \tag{A.11}$$

Replacing Equation A.11 in Equation A.9 and Equation A.10 yields,

$$\bar{\lambda} = \frac{\mu K(1-n)}{5\pi(1-\nu)}\left[\frac{3\pi}{2K}\frac{1-\nu}{1-n}\frac{\sigma}{\mu}\right]^3 \tag{A.12}$$

$$\bar{\mu} = \frac{\mu K(1-n)}{5\pi(1-\nu)}\left[\frac{3\pi}{2K}\frac{(1-\nu)}{(1-n)}\frac{\sigma}{\mu}\right]^3 \tag{A.13}$$

Equation A.12 and Equation A.13 requires the assumption that a small portion of the top of the bed is unattached.

BIBLIOGRAPHY

[1] A.M. Abdilghanie. *A numerical investigation of turbulence-driven and forced generation of internal gravity waves in stratified mid-water*. PhD thesis, Cornell University, 2011.

[2] A.M. Abdilghanie and P.J. Diamessis. On the generation and evolution of numerically simulated large-amplitude internal gravity wave packets. *Theor. Comput. Fluid Dyn.*, 26:205–224, 2012.

[3] P. Aghsaee and L. Boegman. Experimental investigation of sediment resuspension beneath internal solitary waves of depression. *J. Geophys. Res.*, 120:3301–3314, 2015.

[4] P. Aghsaee, L. Boegman, P.J. Diamessis, and Lamb K.G. Boundary-layer-separation-driven vortex shedding beneath internal solitary waves of depression. *J. Fluid Mech.*, 690:321–344, 2012.

[5] P. Aghsaee, L. Boegman, and K.G. Lamb. Breaking of shoaling internal solitary waves. *J. Fluid Mech.*, 659:289–317, 2010.

[6] A. Aigner, D. Broutman, and R. Grimshaw. Numerical simulations of internal solitary waves with vortex cores. *Fluid Dyn. Res.*, 25:315–333, 1999.

[7] P. Alfaro, J. Delgado, A. Estévez, J. Molina, M. Moretti, and J. Soria. Liquefaction and fluidization structures in messinian storm deposits (bajo segura basin, betic cordillera, southern spain). *Int. J. Earth Sc.*, 91(3):505–513, 2002.

[8] M.H. Alford, R.-C. Lien, H. Simmons, J. Klymak, S. Ramp, Y.-J. Yang, D. Tang, and M.-H. Chang. Speed and evolution of nonlinear inter-

nal waves transiting the south china sea. *J. Phys. Oceanogr.*, 40(6):1338–1345,1347–1355, 2010.

[9] M.H. Alford, T. Peacock, J.A. MacKinnon, J.D. Nash, M.C. Buijsman, L.R. Centurioni, S.-Y. Chao, M.-H. Chang, D.M. Farmer, O.B. Fringer, K.-H. Fu, P.C. Gallacher, H.C. Graber, K.R. Helfrich, S.M. Jachec, C.R. Jackson, J.M. Klymak, D.S. Ko, S. Jan, T.M. Shaun Johnston, S. Legg, I.-H. Lee, R.-C. Lien, M.J. Mercier, J.N. Moum, R. Musgrave, J.-H. Park, A.I. Pickering, R. Pinkel, L. Rainville, S.R. Ramp, D.L. Rudnick, S. Sarkar, A. Scotti, H.L. Simmons, L.C. St Laurent, S.K. Venayagamoorty, Y.-H. Wang, J. Wang, Y.-J. Yang, T. Paluszkiewicz, and T.-Y. Tang. The formation and fate of internal waves in the south china sea. *Nature*, 521:65–69, 2015.

[10] O. Andreassen and C.E. Easber. Gravity wave breaking in two and three dimensions 1. model description and comparison of two-dimensional evolutions. *J. Geophys. Res.*, 99(D4):8095–8108, 1994.

[11] J.R. Apel and J.R. Holbrook. Internal solitary waves in the sulu sea. *J. Hopkins Apl. Tech. D.*, 4(6):267–275, 1983.

[12] R.S. Arthur and O.B. Fringer. The dynamics of breaking internal solitary waves on slopes. *J. Fluid Mech.*, 761:360–398, 2014.

[13] T.E. Baldock and P. Holmes. Seepage effects on sediment transport by waves and currents. In *Procedings of 26th Conference on Coastal Engineering, Copenhagen, Denmark*, number 26, pages 3601–3614, 1998.

[14] M. Barad and O.B. Fringer. Simulations of shear instabilities in interfacial gravity waves. *J. Fluid Mech.*, 644:61–95, 2010.

[15] J. Bear. *Dynamics of Fluids in Porous Media*. Elsevier, 1972.

[16] R.H. Bennett and J.R. Faris. Ambien and dynamic pore pressure in fine-grained submarine sediments: Mississippi delta. *Appl. Ocean Res.*, 1:115–123, 007 1979.

[17] L. Bjerrum. Geotechnical problems involved in foundations of structures in the north sea. *Géotechnique*, 23(3):319–358, 1973.

[18] D. Bogucki and C. Garrett. A simple model for the shear-induced decay of an internal solitary wave. *J. Phys. Oceanogr.*, 23:1767–1776, 1993.

[19] D.J. Bogucki, L. G. Redekopp, and J. Barth. Internal solitary waves in the coastal mixing and optics 1996 experiment: Multimodal structure and resuspension. *J. Geophys. Res.*, 110(C2), 2005. C02024.

[20] D.J. Bogucki and L.G. Redekopp. A mechanism for sediment resuspension by internal solitary waves. *Geophys. Res. Lett.*, 26(9):1317–1320, 1999.

[21] D. Bourgault, D.C. Janes, and P.S. Galbraith. Observations of a large-amplitude internal wave train and its reflection off a steep slope. *J. Phys. Oceanogr.*, 41(3):586–600, 2011.

[22] J.P. Boyd. *Chebyshev and Fourier Spectral Methods*. Dover, second edition edition, 2001.

[23] A. Brandt and K.R. Shipley. Laboratory experiments on mass transport by large amplitude mode-2 internal solitary waves. *Phys. Fluids*, 26(046601), 2014.

[24] W. Brutsaert and A.I. El-Kadi. The relative importance of compressibility and partial saturation in unconfined groundwater flow. *Water Resour. Res.*, 20(3):400–408, 1984.

[25] B. Butman, P.S. Alexander, A. Scotti, R.C. Beardsley, and S.P. Anderson. Large internal waves in massachussetts bay tranposrt sediments offshore. *Cont. Shelf Res.*, 26:2029–2049, 2006.

[26] M. Carr and P.A. Davies. The motion of an internal solitary wave of depression over a fixed bottom boundary in a shallow, two-layer fluid. *Physics of Fluid*, 18, 2006.

[27] M. Carr, P.A. Davies, and R.P. Hoebers. Experiments on the structure and stability of mode-2 internal solitary-like waves propagating on an offset pycnocline. *Phys. Fluids*, 27, 2015.

[28] M. Carr, P.A. Davies, and P. Shivaram. Experimental evidence of internal solitary wave-induced global instability in shallow water bething boundary layers. *Phys. Fluids*, 20, 2008.

[29] M. Carr, S.E. King, and D.G. Dritschel. Numerical simulations of shear-induced instabilities in internal solitary waves. *J. Fluid Mech.*, 683:263–288, 2011.

[30] M. Carr, S.E. King, and D.G. Dritschel. Instability in internal solitary waves with trapped cores. *Phys. Fluids*, 24, 2012.

[31] G.S. Carter, M.C. Gregg, and R.C. Lien. Internal waves, solitary-like waves, and mixing on the monterey bay shelf. *Cont. Shelf Res.*, 25:1499–1520, 2005.

[32] M.-H. Chang, R.-C. Lien, Y.-J. Yang, T.-Y. Tang, and J. Wang. A composite view of surface signatures and interior properties of nonlinear internal waves: Observations and applications. *J. Atmos. Oceanic Technol.*, 25:1218–1227, 2008.

[33] M.-H. Chang, R.-C. Lien, Y.-J. Yang, T.-Y. Tang, and J. Wang. Nonlinear internal wave properties estimated with moored adcp measurements. *J. Atmos. Oceanic Technol.*, 28:802–815, 2011.

[34] C.Y. Chen and J.R.C. Hsu. Interaction between internal waves and a permeable seabed. *Ocean Eng.*, 32:587–621, 2005.

[35] S.R. Clarke and R.H.J. Grimshaw. Resonantly generated internal waves in a contraction. *J. Fluid Mech.*, 274:139–161, 1994.

[36] R.H. Cross, V.A. Baker, D.D. Treadwell, and S.R. Huntsman. Attenuation of wave-induced pore pressures in sand. In *Civil Engineering in the Oceans IV*, pages 745–757, 1979.

[37] R.E. Davis and A.Acrivos. Solitary internal waves in deep water. *J. Fluid Mech.*, 29:593–607, 1967.

[38] D. Deepwell and M. Stastna. Mass transport by mode-2 internal solitary-like waves. *Phys. Fluids*, 28(056606), 2016.

[39] O.G. Derzho and R. Grimshaw. Solitary waves with a vortex core in a shallow layer of stratified fluid. *Phys. Fluids*, 9(11), 1997.

[40] M.O. Deville, P.F. Fischer, and E.H. Mund. *High Order Methods for Incompressible Fluid Flow*. Cambridge University Press, 2002.

[41] P.J. Diamessis, J.A. Domaradzki, and J.S. Hesthaven. A spectral multidomain penalty method model for the simulation of high reynolds number localized incompressible stratified turbulence. *J. Comput. Phys.*, 202:198–322, 2005.

[42] P.J. Diamessis, Y.C. Lin, and J.A. Domaradzki. Effective numerical viscosity in spectral multidomain penalty method-based simulations of localized turbulence. *J. Comput. Phys.*, 227:8145–8164, 2008.

[43] P.J. Diamessis and L.G. Redekopp. Numerical investigation of solitary internal wave-induced global instability in a shallo water benthig boundary layers. *J. Phys. Oceanogr.*, 36:784–812, 2006.

[44] P.J. Diamessis, G.R. Spedding, and J.A. Domaradzki. Scaling and structure of high reynolds number stratified turbulent wakes. *J. Fluid Mech.*, 671:52–95, 2011.

[45] P.J. Diamessis, S. Wunsch, I. Delwiche, and P.M. Richter. Nonlinear generation of harmonics through the interaction of an internal wave beam with a model oceanic pycnocline. *Dyn. Atmos. Oceans*, 66:110–137, 2014.

[46] P.J. Digby. The effective elastic moduli of porous granular rock. *J. Appl. Mech.*, 48:803–808, 1981.

[47] T.M. Dillon. Vertical overturns: A comparison of thorpe and ozmidov length scales. *J. Geophys. Res.*, 87(C12):9601–9613, 1982.

[48] V.D. Djordjevic and L.G. Redekopp. The fission and disintegration of internal solitary waves moving over two-dimensional topography. *J. Phys. Oceanogr.*, 8:1016–1024, 1978.

[49] A. Dörnbrack. Turbulent mixing by breaking gravity waves. *J. Fluid Mech.*, 375:113–141, 1998.

[50] R. Droghei, F. Falcini, D. Casalbore, E. Martorelli, R. Mosetti, G. Sannino, R. Santoleri, and F.L. Chiocci. The role of internal solitary waves on deep-

water sedimentary processes: the case of up-slope migrating sediment waves off the messina strait. *Sci. Rep.-UK*, 6:36376:1–8, 2016.

[51] T.F. Duda, J.F. Lynch, J.D. Irish, R.C. Beardsley, S.R. Ramp, C.-S. Chiu, T.-Y. Tang, and Y.-J. Yang. Internal tide and nonlinear internal wave behavior at the continental slope in the norhtern south china sea. *IEEE J. Oceanic Eng.*, 29(4), 2004.

[52] M. Dunphy, C. Subich, and M. Stastna. Spectral methods for internal waves: indistinguishable density profiles and double-humped solitary waves. *Nonlinear Proc. Geoph.*, 18:351–358, 2011.

[53] W.D. Liam Finn, R. Siddharthan, and G.R. Martin. Response of seafloor to ocean waves. *J. Geotech. Eng.-ASCE*, 109(4):556–572, 1983.

[54] O.B. Fringer, M. Gerritsen, and R.L. Street. An unstructured-grid, finite-volume, nonhydrostatic, parallel coastal ocean simulator. *Ocean Model*, 14:139–173, 2006.

[55] O.B. Fringer and R.L. Street. The dynamics of breaking progressive interfacial waves. *J. Fluid Mech.*, 494:319–353, 2003.

[56] D. Fructus, M. Carr, J. Grue, A. Jensen, and P.A. Davies. Shear-induced breaking of large internal solitary waves. *Nonlinear Proc. Geoph.*, 18:351–358, 2011.

[57] D. Fructus and J. Grue. Fully nonlinear solitary waves in a layered stratified fluid. *J. Fluid Mech.*, 505:323–347, 2004.

[58] D. Funaro and D. Gottlieb. A new method of imposing boundary conditions in pseudospectral approximations of hyperbolic equations. *Math. Comput.*, 51(184):599–613, 1988.

[59] D. Funaro and D. Gottlieb. Convergence results for pseudospectral approximations of hyperbolic systems by a penalty-type boundary treatment. *Math. Comput.*, 57(196):585–596, 1991.

[60] T. Gerkema and J.T.F. Zimmerman. An introduction to internal waves, 2008.

[61] N. Gratiot and M. Mory. Wave-induced sea bed liquefaction with application to mine burial. In *Proceedings of the Tenth (2002) International Offshore and Polar Engineering Conference*. The International Society of Offshore and Polar Engineers, 2000.

[62] R. Grimshaw, E. Pelinovsky, T. Talipova, and A. Kurkin. Simulation of the transformation of internal solitary waves on oceanic shelves. *J. Phys. Oceanogr.*, 34:2774–2790, 2004.

[63] J. Grue, A. Jense, P.O. Rusas, and J.K. Sveen. Properties of large-amplitude internal waves. *J. Fluid Mech.*, 380:257–278, 1999.

[64] J. Grue, A. Jensen, P.-O. Rusas, and J. Kristian Sveen. Breaking and broadening of internal solitary waves. *J. Fluid Mech.*, 413:181–217, 2000.

[65] G. Haller. An objective definition of a vortex. *J. Fluid Mech.*, 525:1–26, 2005.

[66] L.R. Haury, M. Briscoe, and M.H. Orr. Tidally generated internal wave packets in massachusetts bay. *Nature*, 278:312–317, 1979.

[67] Y. He and K.G. Lamb. Internal solitary waves with subsurface cores. In preparation for Journal of Fluid Mechanics, 2018.

[68] Karl R. Helfrich and W. Kendall Melville. Long nonlinear internal waves. *Annu. Rev. Fluid Mech.*, 38:395–425, 2006.

[69] K.R. Helfrich. Internal solitary wave breaking and run-up on a uniform slope. *J. Fluid Mech.*, 243:133–154, 1992.

[70] K.R. Helfrich and R.H. Grimshaw. Nonlinear disintegration of the internal tide. *J. Phys. Oceanogr.*, 38:686–701, 2008.

[71] K.R. Helfrich and W.K. Melville. On long nonlinear internal waves over slope-shelf topography. *J. Fluid Mech.*, 167:285–308, 1986.

[72] K.R. Helfrich and B.L. White. A model for large-amplitude internal solitary waves with trapped cores. *Nonlinear Proc. Geoph.*, 17:303–318, 2010.

[73] J.S. Hesthaven, S. Gottlieb, and D. Gottlieb. *Spectral Methods for Time-Dependent Problems*. Cambridge University Press, 2007.

[74] P.E. Holloway. Internal hydraulic jumps and solitons at a shelf break region on the australian north west shelf. *J. Geophys. Res.*, 92(C2):5405–5416, 1987.

[75] J.Y. Holyer. Large amplitude progessive interfacial waves. *J. Fluid Mech.*, 93:433–448, 1979.

[76] P. Hosegood and H. van Haren. Near-bed solibores over the continental slope in the faeroe-shetland channel. *Deep-Sea Res. Pt. II*, 51:2943–2971, 2004.

[77] M.K. Hsu and A.K. Liu. Nonlinear internal waves in the south china sea. *Can. J. Remote Sens.*, 26(2):72–81, 2000.

[78] C.R. Jackson, J.C.B. da Silva, and G. Jeans. The generation of nonlinear internal waves. *Oceanography*, 25, June 2012.

[79] M. Jalali and S. Sarkar. Large eddy simulation of flow and turbulence at the steep topography of luzon strait. *Geophys. Res. Lett.*, 44:9440–9448, 2017.

[80] S.M. Joshi. *Development of fast high-order numerical methods for high-reynolds number environmental flows*. PhD thesis, Cornell University, 2016.

[81] S.M. Joshi, P.J. Diamessis, D.T. Steinmoller, M.S. Stastna, and G. Thomsen. A post-processing technique for stabilizing the discontinuous pressure projection operator in marginally-resolved incompressible inviscid flow. *Computers and Fluids*, (1-10), 2016b.

[82] D. Kang and O. Fringer. On the calculation of available potential energy in internal wave fields. *J. Phys. Oceanogr.*, 40:2539–2545, 2010.

[83] T.W. Kao, F.-S. Pan, and D. Renouard. Internal solitons on the pycnocline: generation, propagation, and shoaling and breaking over a slope. *J. Fluid Mech.*, 159:19–53, 1985.

[84] G.E. Karniadakis, M. Israeli, and S.A. Orszag. High-order splitting methods for the incompressible navier-stokes equations. *J. Comput. Phys.*, 97:411–443, 1991.

[85] G.H. Keulegan. Characteristics of internal solitary waves. *J. Res. Nat. Bur. Stand.*, 51(3), 1953.

[86] L.F. Kilcher and J.D. Nash. Structure and dynamics of the columbia river tidal plume front. *J. Geophys. Res.*, 115(C05S90), 2010.

[87] S.E. King, M. Carr, and D.G. Dritschel. The steady-state form of large-amplitude internal solitary waves. *J. Fluid Mech.*, 666:477–505, 2011.

[88] J.M. Klymak and J.N. Moum. Internal solitary waves of elevation advancing on a shoaling shelf. *Geophys. Res. Lett.*, 30(20), 2003. 2045.

[89] C.G. Koop and F.K. Browand. Instability and turbulence in a stratified fluid with shear. *J. Fluid Mech.*, 93:135–139, 1979.

[90] G.C. Koop and G. Butler. An investigation of internal solitary waves in a two-fluid system. *J. Fluid Mech.*, 112:225–251, 1981.

[91] D.A. Kopriva. *Implementing Spectral Methods for Partial Differential Equations*. Springer, 2009.

[92] P.K. Kundu, I.M. Cohen, and D.R. Dowling. *Fluid Mechanics*. Elsevier, 2012.

[93] K.G. Lamb. Numerical experiments of internal wave generation by strong tidal flow across a finite amplitude bank edge. *J. Geophys. Res.*, 99(C1):843–864, 1994.

[94] K.G. Lamb. A numerical investigation of solitary internal waves with trapped cores formed via shoaling. *J. Fluid Mech.*, 451:109–144, 2002.

[95] K.G. Lamb. Shoaling solitary internal waves: on a criterion for the formation of waves with trapped cores. *J. Fluid Mech.*, 478:81–100, 2003.

[96] K.G. Lamb. On the calculation of the available potential energy of an isolated perturbation in a density-stratified fluid. *J. Fluid Mech.*, 597:415–427, 2008.

[97] K.G. Lamb and D. Farmer. Instabilities in an internal solitary-like wave on the oregon shelf. *J. Phys. Oceanogr.*, 41:67–87, 2011.

[98] K.G. Lamb and V.T. Nguyen. Calculating energy flux in internal solitary waves with an application to reflectance. *J. Phys. Oceanogr.*, 39:559–580, 2009.

[99] K.G. Lamb and A. Warn-Varnas. Two-dimensional numerical simulations of shoaling internal solitary waves at the asiaex site in the south china sea. *Nonlinear Proc. Geoph.*, 22:289–312, 2015.

[100] K.G. Lamb and K.P. Wilkie. Conjugate flows for waves with trapped cores. *Phys. Fluids*, 16(12), 2004.

[101] T.W. Lambe and R.V. Whitman. *Soil Mechanics*. John Wiley and Sons, Inc., 1969.

[102] R.-C. Lien, E.A. D'Asaro, F. Henyey, M.-H. Chang, T.-Y. Tang, and Y.-J. Yang. Trapped core formation within a shoaling nonlinear internal wave. *J. Phys. Oceanogr.*, 42:511–525, 2012.

[103] R.-C. Lien, F. Henyey, B. Ma, and Y.-J Yang. Large-amplitude internal solitary waves observed in the northern south china sea: Properties and energetics. *J. Phys. Oceanogr.*, 44(4):1095–1115, 2014.

[104] R.-C. Lien, T.Y. Yang, M.H. Chang, and E.A. D'Asaro. Energy of nonlinear internal waves in the south china sea. *Geophys. Res. Lett.*, 32(L05615), 2005.

[105] P.L. Liu, Y.S. Park, and J.L. Lara. Long-wave-induced flows in an unsaturated permeable bed. *J. Fluid Mech.*, 586:323–345, 2007.

[106] R.R. Long. Some aspects of the flow of stratified fluids i. a theoretical investigation. *Tellus*, 8:460–471, 1953.

[107] P. Luzzatto-Fegiz and K.R. Helfrich. Laboratory experiments and simulations for solitary internal waves with trapped cores. *J. Fluid Mech.*, 757:354–380, 2014.

[108] V. Maderich, K. T. Jung, K. Terletska, I. Brovchenko, and T. Talipova. Incomplete similarity of internal solitaru waves with trapped cores. *Fluid Dyn. Res.*, 47(3), 2015.

[109] V. Maderich, K.-T. Jung, K. Terletska, and K.-O. Kim. Head-on collision of internal waves with trapped cores. *Nonlinear Proc. Geoph.*, 24:751–762, 2017.

[110] O.S. Madsen. Stability of a sand bed under breaking waves. In *Procedings of 14th Conference on Coastal Engineering, Copenhagen, Denmark*, number 14, pages 776–794, 1974.

[111] O.S. Madsen. Wave-induced pore pressures and effective stresses in a porous bed. *Géotechnique*, 28(4):377–393, 1978.

[112] C. S. Martin. Effect of a porous sand bed on incipient sediment motion. *Water Resour. Res.*, 6(4):1162–1174, 1970.

[113] T. Maxworthy. A note on the internal solitary waves produced by tidal flow over a three-dimensional ridge. *J. Geophys. Res.*, 84(C1):338–346, 1979.

[114] T. Maxworthy. On the formation of nonlinear internal waves from the gravitational collapse of mixed regions in two and three dimensions. *J. Fluid Mech.*, 96:47–64, 1980.

[115] E.E. McPhee-Shaw and E. Kunze. Boundary layer intrusions from a sloping botom: a mechanism for generating intermediate nepheloid layers. *J. Geophys. Res.*, 107(3050), 2002.

[116] A.P. Mehta, B.R. Sutherland, and P.J. Kyba. Interfacial gravity currents. ii. wave excitation. *Phys. Fluids*, 14(3558), 2002.

[117] H. Michallet and G.N. Ivey. Experiments on mixing due to internal solitary waves breaking on uniform slopes. *J. Geophys. Res.*, 104(C06):13467–13477, 1999.

[118] H. Michallet, M. Mory, and I. Piedra-Cueva. Wave-induced pore pressure measurements near a coastal structure. *J. Geophys. Res.*, 114(C06019):1–18, 2009.

[119] J.W. Miles. On the stability of heterogeneous shear flows. *J. Fluid Mech.*, 10(4):496–508, 1961.

[120] J.M. Molina, P. Alfaro, M. Moretti, and J.M. Soria. Soft-sediment deformation structures induced by cyclic stress of storm waves in tempestites (miocene, guadalquivir basin, spain). *Terra Nova*, 10(3), 1998.

[121] S.E. Moore and R.-C. Lien. Pilot whales follow internal solitary waves in the south china sea. *Mar. Mammal Sci.*, 21(1):193–196, 2007.

[122] H. Moshagen and A. Tørum. Wave-induced pressures in permeable seabeds. *J. Waterway Div.-ASCE*, 101(WW1):49–71, 1975.

[123] J. N. Moum, D. M. Farmer, E. L. Shroyer, W. D. Smyth, and L. Armi. Dissipative losses in nonlinear internal waves propagating across the continental shelf. *J. Phys. Oceanogr.*, 37(7):1989–1995, 2007.

[124] J. N. Moum, J. M. Klymak, J. D. Nash, A. Perlin, and W. D. Smyth. Energy transport by nonlinear internal waves. *J. Phys. Oceanogr.*, 37(7):1968–1988, 2007.

[125] J.N. Moum, D.M. Farmer, W.D. Smyth, L. Armi, and S. Vagle. Structure and generation of turbulence at interfaces strained by internal solitary waves propagating shoreward over the continental shelf. *J. Phys. Oceanogr.*, 33:2093–2112, 2003.

[126] J.N. Moum and J.D. Nash. Seafloor pressure measurements of nonlinear internal waves. *J. Phys. Oceanogr.*, 38:481–491, 2008.

[127] J.N. Moum and W.D. Smyth. The pressure disturbance of a nonlinear internal wave train. *J. Fluid Mech.*, 558:153–177, 2006.

[128] T. Nakamura, Y. Kawasaki, T. Kono, and T. Awaji. Large-amplitude internal waves observed in the kruzenshtern strait of the kuril island chain and possible water transport and mixing. *Cont. Shelf Res.*, 30:598–607, 2010.

[129] J.D. Nash and J.N. Moum. River plumes as a source of large-amplitude internal waves in the coastal ocean. *Nature*, 437:400–403, 2005.

[130] M.S. Nataraja and H.S. Gill. Ocean wave-induced liquefaction analysis. *J. Geotech. Eng.-ASCE*, 109(4):573–590, 1983.

[131] D.A. Nelson and G.B. Jacobs. Dg-ftle: Lagrangian coherent structures with high-order discontinuous-galerkin methods. *J. Comput. Phys.*, 295:65–86, 2015.

[132] A.L. New and R.D. Pingree. Large-amplitude internal soliton packets in the central bay of biscay. *Deep-Sea Res.*, 37(3):513–524, 1990.

[133] S. Okusa. Wave-induced stresses in unsaturated submarine sediments. *Géotechnique*, 35:517–532, 1985.

[134] J. Olsthoorn, M. Stastna, and N. Soontiens. Fluid circulation and seepage in lake sediment due to propagating and trapped internal waves. *Water Resour. Res.*, 48, 2012.

[135] I. Orlansky and K. Bryan. Formation of the thermocline step stucture by large-amplitude internal gravity waves. *J. Geophys. Res.*, 74(28), 1969.

[136] A.R. Osborne and T.L. Burch. Internal solitons in the andaman sea. *Science*, 208(4443), 1980.

[137] R.B. Perry and G.R. Schmike. Large-amplitude internal waves observed off the northwest coast of sumatra. *J. Geophys. Res.*, 70(10), 1965.

[138] R. Peyret. *Handbook of Computational Fluid Mechanics*. Academic Press, 1996.

[139] O.M. Phillips. *The dynamics of the upper ocean*. Cambridge, second edition edition, 1977.

[140] S.B. Pope. *Turbulent Flows*. Cambridge University Press, 2000.

[141] M. Preusse, M. Stastna, H. Freistuehler, and F. Peeters. Intrinsic breaking of internal solitary waves in a deep lake. *PLOS ONE*, 7(e41674), 2012.

[142] L.S. Quaresma, J. Vitorino, A. Oliveira, and J. da Silva. Evidence of sediment resuspension by nonlinear internal waves on the western portuguese mid-shelf. *Mar. Geo.*, 246:123–143, 2007.

[143] S.R. Ramp, T.Y. Tang, T.F. Duda, J.F. Lynch, A.K. Liu, C.S. Chiu, F.L. Bahr, H.R. Kim, and Y.J. Yang. Internal solitons in the northeastern south china

sea part i: Sources and deep water propagation. *IEEE J. Oceanic Eng.*, 29(29):1157–1181, 2004.

[144] D.B. Reeder, B.B. Ma, and J. Yang, Y. Very large subaqueous sand dunes on the upper continental slope in the south china sea generated by episodic, shoaling deep-water internal solitary waves. *Mar. Geo.*, 279:12–18, 2011.

[145] G.A. Rivera-Rosario, P.J. Diamessis, and J.T. Jenkins. Bed failure induced by internal solitary waves. *J. Geophys. Res.*, 122:5468–5485, 2017.

[146] I.S. Robinson. *Discovering the Ocean from Space: The unique applications of satellite oceanography*. Springer, 2010.

[147] J.W. Rottman and R. Grimshaw. *Environmental Stratified Flows*, chapter Atmospheric Internal Solitary Waves. Kluwer Academic Publishers, 2002.

[148] Jr. R.R. Hodges. Generation of turbulence in the upper atmosphere by internal gravity waves. *J. Geophys. Res.*, 72(13), 1967.

[149] J.S. Russell. Report on waves. Technical report, Murray, 1844.

[150] M.K. Sadek, L. Parras, and P.J. Diamessis. By-pass transition to turbulence under a surface solitary wave. in preparation for Journal of Fluid Mechanics, 2016.

[151] M.K. Sadek, L. Parras, P.J. Diamessis, and P.L.F. Liu. Two-dimensional instability of the bottom boundary layer under a surface solitary wave. *Phys. Fluids*, 27(044104), 2015.

[152] K. Saffarinia and T.W. Kao. A numerical study of the breaking of an internal soliton and its interaction with a slope. *Dyn. Atmos. Oceans*, 23:379–391, 1996.

[153] T. Sakai, K. Hatanaka, and H. Mase. Wave-induced effective stress in seabed and its momentary liquefaction. *J. Waterw. Port. C. Div.*, 118(2):202–206, 1992.

[154] H. Salehipour, W.R. Peltier, and A. Mashayek. Turbulent diapycnal mixing in stratified shear flows: the influence of prandtl number on mixing efficiency and transition at high reynolds number. *J. Fluid Mech.*, 773:178–223, 2015.

[155] M. Salloum, O.M. Knio, and A. Brandt. Numerical simulation of mass transport in internal solitary waves. *Phys. Fluids*, 24(016602), 2012.

[156] H. Sandstrom and J.A. Elliott. Internal tide and solitons on the scotian shelf: A nutrient pump at work. *J. Geophys. Res.*, 89(C4):6415–6426, 1984.

[157] E. Santilli and A. Scotti. The stratified ocean model with adaptive refinement (somar). *J. Comput. Phys.*, 291:60–81, 2015.

[158] L. Scholtès, B. Chareyre, H. Michallet, E. Catalano, and M. Marzougui. Modeling wave-induced pore pressure and effective stress in a granular seabed. *Continuum Mech. Therm.*, 27(1):305–323, 2014.

[159] A. Scotti and J. Pineda. Observation of very large and steep internal waves of elevation near the massachusetts coast. *Geophys. Res. Lett.*, 31(22), 2004. L22307.

[160] E.L. Shroyer. *Small-Scale Processes in the Coastal Ocean*, chapter Varicose Waves. Oceanography, 2008.

[161] E.L. Shroyer, J.N. Moum, and J.D. Nash. Nonlinear internal waves over new jersey's continental shelf. *J. Geophys. Res.*, 116(C03022), 2011.

[162] J. Small. A nonlinear model of the shoaling and refraction of interfacial solitary waves in the ocean. part i: Development of the model and investigations of the shoaling effect. *J. Phys. Oceanogr.*, 31:3163–3183, 2001.

[163] W.B. Smyth and J.N. Moum. Length scales of turbulence in stably stratified mixing layers. *Phys. Fluids*, 12(6):1327–1342, 2000.

[164] W.B. Smyth, J.N. Moum, and D.R. Caldwell. The efficiency of mixing in turbulent patches: Inferences from direct simulations and microstructure observations. *J. Phys. Oceanogr.*, 31:1969–1992, 2001.

[165] N. Soontiens, C. Subich, and M. Stastna. Numerical simulation of supercritical trapped internal waves over topography. *Phys. Fluids*, 22(116605), 2010.

[166] A.P. Stamp and M. Jacka. Deep-water internal solitary waves. *J. Fluid Mech.*, 305:347–371, 1995.

[167] T.P. Stanton and L.A. Ostrovsky. Observations of highly nonlinear internal solitons over the continental shelf. *Geophys. Res. Lett.*, 25(14):2695–2698, 1998.

[168] M. Stastna and K.G. Lamb. Large fully nonlinear internal solitary waves: The effect of background current. *Phys. Fluids*, 14(9):2987–2999, 2002.

[169] M. Stastna and K.G. Lamb. Sediment resuspension mechanicsm associated with internal waves in coastal waters. *J. Geophys. Res.*, 113, 2008.

[170] B.M. Sumer, F. Hatipoglu, J. Fredsøe, and N.-E. Ottesen Hansen. Critical flotation density of pipelines in soils liquefied by waves and density of liquefied soils. *J. Waterw. Port. C. Div.*, 132(4):252–265, 2006.

[171] M.B. Sumer. *Liquefaction Around Marine Structures*. World Scientific, 2014.

[172] M.B. Sumer, M.B. Sen, I. Karagali, B. Ceren, J. Fredsøe, M. Sottile, L. Zilioli, and D.R. Fuhrman. Flow and sediment transport induced by a plunging solitary wave. *J. Geophys. Res.*, 116, 2011.

[173] D.E. Terez and O.M. Knio. Numerical simulations of large-amplitude internal solitary waves. *J. Fluid Mech.*, 362:53–82, 1998.

[174] J. A. Thomas, J. A. Lerczak, and J. N. Moum. Horizontal variability of high-frequency nonlinear internal waves in massachusetts bay detected by an array of seafloor pressure sensors. *J. Geophys. Res.*, 121(8):5587–5607, 2016.

[175] S.A. Thorpe. *The Turbulent Ocean*. Cambridge University Press, 2005.

[176] A. Tørum. Wave-induced pore pressure- air/gas content. *J. Waterw. Port. C. Div.*, 133(1):83–86, 2007.

[177] C.D. Troy and J.R. Koseff. The instability and breaking of long internal waves. *J. Fluid Mech.*, 543:107–136, 2005.

[178] Y.-H. Tseng and J.H. Ferziger. Mixing and available potential energy in stratified flows. *Phys. Fluids*, 13(5), 2001.

[179] B. Turkington, A. Eydeland, and S. Wang. A computational method for solitary internal waves in a continously stratified fluid. *Stud. Appl. Math.*, 85:93–127, 1991.

[180] H. van Haren. Bottom-pressure observations of deep-sea internal hydrostatic and non-hydrostatic motions. *J. Fluid Mech.*, 714:591–611, 2013.

[181] A. Verruijt. *Flow Through Porous Media*, chapter Elastic Storage of Aquifers. Academic Press, 1969.

[182] A. Verruijt. *Theory and Problems of Poroelasticity*, chapter Theory of Poroelasticity. Delft, 2016.

[183] V. Vlasenko and K. Hutter. Numerical experiments on the breaking of solitary internal waves over a slope-shelf topography. *J. Phys. Oceanogr.*, 32:1779–1793, 2002.

[184] V. Vlasenko, L. Ostrovsky, and K. Hutter. Adiabatic behavior of strongly nonlinear internal solitary waves in slope-shelf areas. *J. Geophys. Res.*, 110(C04006), 2005.

[185] B.C. Wallace and D.L. Wilkinson. Run-up of internal waves on a gentle slope in a two-layered system. *J. Fluid Mech.*, 191:419–442, 1988.

[186] R.K. Walter, M. Stastna, C.B. Woodson, and S.G. Monismith. Observations of nonlinear internal waves at a persistent coastal upwelling front. *Cont. Shelf Res.*, 117:100 – 117, 2016.

[187] S.J. Williams and D.-S. Jeng. The effects of a porous-elastic seabed on the interfacial wave propagation. *Ocean Eng.*, 34:1818–1831, 2007.

[188] K.B. Winters and E.A. D'Asaro. Three-dimensional wave instability near a critical layer. *J. Fluid Mech.*, 272:255–284, 1994.

[189] K.B. Winters, P.N. Lombard, J.J. Riley, and E.A. D'Asaro. Available potential energy and mixing in density-stratified fluids. *J. Fluid Mech.*, 289:115–128, 1995.

[190] T. Yamamoto, H.L. Koning, H. Sellmeijer, and E. Van Hijum. On the response of a poro-elastic bed to water waves. *J. Fluid Mech.*, 87:193–206, 1978.

[191] S. Zhang and M.H. Alford. Instabilities in nonlinear internal waves on the washington continental shelf. *J. Geophys. Res.*, 120:5272–5283, 2015.

[192] Z. Zhao and V. Klemas. Remote sensing evidence for baroclinic tide origin of internal solitary waves in the northeastern south china sea. *Geophys. Res. Lett.*, 31(L06302), 2004.

[193] Q. Zhou and P.J. Diamessis. Reflection of an internal gravity wave beam off a horizontal free-slip surface. *Phys. Fluids*, 25(3), 2013.

[194] Q. Zhou and P.J. Diamessis. Lagrangian flows within reflecting internal waves at a horizontal free-slip surface. *Phys. Fluids*, 27(12), 2015.

[195] Q. Zhou and P.J. Diamessis. Surface manifestation of internal waves emitted by submerged localized stratified turbulence. *J. Fluid Mech.*, 798:505–539, 2016.